

EDITORIAL BOARD

Editor-in-Chief

Igor Krivtsun
E.O. Paton Electric Welding Institute of the NASU, Kyiv, Ukraine

Deputy Editor-in-Chief

Michael Gasik
Aalto University, Espoo, Finland

Deputy Editor-in-Chief

Jacob Kleiman
Integrity Testing Laboratory, Markham, Canada

Editorial Board Members

Serhii Akhonin
E.O. Paton Electric Welding Institute of the NASU, Kyiv, Ukraine

Chunlin Dong
Guangzhou Jiao Tong University, China

Shiyi Gao
China-Ukraine Institute of Welding,
Guangdong Academy of Sciences, Guangzhou, China

Len Gelman
The University of Huddersfield, UK

Andrey Gumenyuk
Bundesanstalt für Materialforschung und –prüfung (BAM),
Berlin, Germany
Vitalii Knysh
E.O. Paton Electric Welding Institute of the NASU, Kyiv, Ukraine

Volodymyr Korzhyk
E.O. Paton Electric Welding Institute of the NASU, Kyiv, Ukraine
Victor Kvasnytskyi
NTUU «Igor Sikorsky Kyiv Polytechnic Institute», Ukraine

Yuliia Kvasnytska
Physico-Technological Institute of Metals and Alloys
of the NASU, Kyiv, Ukraine

Leonid Lobanov
E.O. Paton Electric Welding Institute of the NASU, Kyiv, Ukraine

Eric Macdonald
The University of Texas at El Paso, USA

Anatoliy Maistrenko
V. Bakul Institute for Superhard Materials
of the NASU, Kyiv, Ukraine

Serhiy Maksymov
E.O. Paton Electric Welding Institute of the NASU, Kyiv, Ukraine

Dhanesh G. Mohan
School of Engineering University of Sunderland England,
United Kingdom

João Pedro Oliveira
Universidade NOVA de Lisboa, Portugal

Valerii Peremitko
Dniprovsky State Technical University, Kamianske, Ukraine

Valeriy Pozniakov
E.O. Paton Electric Welding Institute of the NASU, Kyiv, Ukraine

Uwe Reisgen
Welding and Joining Institute, Aachen, Germany

Massimo Rogante
Rogante Engineering, Civitanova Marche, Italy

Cezary Senderowski
Mechanics and Printing Institute, Warsaw University
of Technology, Poland

Magdalena Speicher
Kempten University of Applied Sciences, Germany

Mattias Thuvander
Chalmers University of Technology, Goteborg, Sweden

Valentyn Uchanin
Karpenko Physico-Mechanical Institute of the NASU, Lviv, Ukraine

Gerald Wilhelm
University of Applied Sciences of Munich, Germany

Yongqiang Yang
South China University of Technology, Guangzhou, China

Executive Editor

Oleksandr Zelnichenko
International Association "Welding", Kyiv, Ukraine

Address of Editorial Office:

E.O. Paton Electric Welding Institute, 11 Kazymyr Malevych Str., 03150, Kyiv, Ukraine
E-mail: office@paton.kiev.ua; <https://paton.org.ua/en/>

Address of Publisher:

International Association "Welding", 11 Kazymyr Malevych Str., 03150, Kyiv, Ukraine
Tel.: (38044) 205 23 90, E-mail: patonpublishinghouse@gmail.com; journal@paton.kiev.ua
<https://patonpublishinghouse.com/eng/journals/tpwj>

The Journal was registered by the National Council of Ukraine on Television and Radio Broadcasting on 09.05.2024, carrier identifier R30-04569
ISSN 0957-798X (Print), ISSN 3041-2293 (Online)
DOI: <https://doi.org/10.37434/tpwj>, from #01, 2020 to now; DOI: <https://doi.org/10.15407/tpwj> from #01, 2014 to #12, 2019.

Subscriptions, 12 issues per year:

348 Euro — annual subscription for the printed (hard copy) version, air postage and packaging included;
288 Euro — annual subscription for the electronic version (sending issues in pdf format or providing access to IP addresses).

Representative Offices of "The Paton Welding Journal":

BRAZIL, Arc Dynamics

Address: Nova Iguacu, Rio de Janeiro, Brazil
Daniel Adolpho, Tel.: +55 21 9 6419 5703,
E-mail: dadolpho@arcdynamics.com.br

CHINA, China-Ukraine Institute of Welding, Guangdong Academy of Sciences

Address: Room 210, No. 363 Changxing Road, Tianhe, Guangzhou, 510650, China
Zhang Yupeng, Tel.: +86-20-61086791,
E-mail: patonjournal@gwi.gd.cn

BULGARIA, Bulgarian Welding Society

Address: Blvd. Asen Yordanov No.10, Sofia 1592, Bulgaria
Pavel Popgeorgiev, Tel.: +359 899 96 22 20,
E-mail: office@bws-bg.org

POLAND, PATON EUROPE Sp. z o. o.

Address: ul. Kapitałowa 4, 35-213, Rzeszów, Poland
Anton Stepakhno, Tel.: +38067 509 95 67,
E-mail: Anton.Stepakhno@paton.ua

The content of the Journal includes articles received from authors from around the world in the field of welding, cutting, cladding, soldering, brazing, coating, 3D additive technologies, electrometallurgy, material science, NDT and selectively includes translations into English of articles from the following journals, published in Ukrainian:

- «Автоматичне Зварювання» (Automatic Welding), [https://patonpublishinghouse.com/eng/journals/as](https://patonpublishinghouse.com/eng/journals/as;);
- «Suchasna Elektrometalurhiya» (Electrometallurgy Today), [https://patonpublishinghouse.com/eng/journals/sem](https://patonpublishinghouse.com/eng/journals/sem;);
- «Tekhnichna Diahnostyka ta Neruinivnyi Kontrol» (Technical Diagnostics & Nondestructive Testing), <https://patonpublishinghouse.com/eng/journals/tdnk>.

CONTENTS

ORIGINAL ARTICLES

S.L. Zhdanov, O.A. Haivoronsky, V.D. Poznyakov, A.V. Zavdoveev, A.M. Gerasymenko, R.V. Bogodist IMPACT OF ARC WELDING AND HIGH-FREQUENCY MECHANICAL FORGING ON THE MECHANICAL PROPERTIES AND RESISTANCE TO BRITTLE FRACTURE OF WELDED JOINTS OF S420NL STEEL *	3
V.V. Holovko, V.A. Kostin, V.V. Zhukov DISPERSED OXIDES INFLUENCE ON THE KINETICS OF THE WELD METAL STRUCTURAL TRANSFORMATIONS*	9
V.V. Skryabinskyi, V.M. Nesterenkov, M.O. Rusynyk, V.I. Zagornikov, O.I. Goncharenko, I.M. Klochkov INFLUENCE OF ELECTRON BEAM WELDING TECHNOLOGY ON THE WIDTH OF THE SOFTENING ZONE OF ALUMINIUM 2219 ALLOY*	19
N.V. Vigilianska, C. Senderowski, T.V. Tsymbalista, K.V. Iantsevitch, A.I. Kildiy, O.Yo. Gudymenko DETONATION SPRAYING OF COATINGS CONTAINING Cr ₂ AlC MAX PHASE*	25
S.V. Akhonin, V.O. Berezos, A.Yu. Severyn, O.H. Yerokhin, V.V. Pashynskyi FEATURES OF SMELTING OF HEAT-RESISTANT TITANIUM ALLOY OF THE Ti-Nb-Al-Mo-Zr ALLOYING SYSTEM BY ELECTRON BEAM MELTING WITH A COLD HEARTH**	31
S.V. Akhonin, V.Yu. Bilous, V.V. Pashynskyi, R.V. Selin, A.Iu. Severin, E.L. Vrzhyzhevskyi THE EFFECT OF ANNEALING ON THE STRUCTURE AND PROPERTIES OF WELDED JOINTS OF HEAT-RESISTANT PSEUDO-α-TITANIUM ALLOY Ti-Al-Zr-Sn-Mo-Nb-Si ALLOYING SYSTEM**	36
V.D. Poznyakov, O.V. Korieniev INFLUENCE OF WELDING THERMAL CYCLES ON THE STRUCTURE AND HARDNESS OF THE METAL IN THE HAZ OVERHEATING AREA IN WELDED JOINTS OF MEDIUM-CARBON ALLOY STEELS OF HIGH HARDNESS**	46

*Translated Article(s) from “Avtomatychne Zvaryuvannya” (Automatic Welding), No. 3, 2025.
**Translated Article(s) from “Suchasna Elektrometalurhiya” (Electrometallurgy Today), No. 2, 2024.



Indexing: The electronic edition of the Journal is stored in the V.I. Vernadsky National Library of Ukraine (eVerLib), included in the OPEN UKRAINIAN CITATION INDEX database and international databases: CROSSREF, EBSCO, Google Scholar, INDEX COPERNICUS, ULRICHSWEB.

IMPACT OF ARC WELDING AND HIGH-FREQUENCY MECHANICAL FORGING ON THE MECHANICAL PROPERTIES AND RESISTANCE TO BRITTLE FRACTURE OF WELDED JOINTS OF S420NL STEEL

**S.L. Zhdanov, O.A. Haivoronsky, V.D. Poznyakov, A.V. Zavdoveev,
A.M. Gerasymenko, R.V. Bogodist**

E.O. Paton Electric Welding Institute of the NASU
11 Kazymyr Malevych Str., 03150, Kyiv, Ukraine

ABSTRACT

The paper considers the regularities of phase-structural transformations in welded joints of low-alloy S420NL steel in the initial state, after high-frequency mechanical forging and accumulation of fatigue damage. Welded joints were produced by mechanized gas metal arc welding in a carbon dioxide environment using Filarc PZ 6114 S flux-cored wire. The grain, subgrain and dislocation structures of welded joints were studied by light and transmission electron microscopy (TEM). The experimental data on the impact of the structure on the change in the values of the impact toughness (KCV) and brittle fracture resistance (K_q) of welded joints without treatment with high-frequency mechanical forging, after accumulation of fatigue damage were obtained. The efficiency of increasing their fatigue resistance due to the use of high-frequency mechanical forging is shown.

KEYWORDS: low-alloy steel, arc welding, welded joints, structure, high-frequency mechanical forging, fatigue damage, brittle fracture

INTRODUCTION

One of the main service characteristics of welded joints is the ability to provide high durability under cyclic loads. However, their fatigue resistance limit may differ significantly from that of the base metal. The probability of failure due to metal fatigue is one of the factors that must be taken into account when designing structures [1, 2]. Fatigue failure starts with one or more cracks on the surface and propagates inwards under repeated force until a complete rupture occurs. The fraction of fatigue damage in welded structures is approximately 40 % of the total number of fractures and failures. The cause is that under cyclic loads, adverse residual stresses play a significant role, the concentration of which is determined by the shape of the weld and technological defects, the gradient of structures and mechanical characteristics at the interface between the weld metal and the HAZ. Additionally, the fatigue resistance is affected by the chemical composition and structure of the base metal, parameters of the welding thermal cycle, loading pattern, environment, etc. [3, 4]. The negative impact of the mentioned factors cannot always be minimized before or during welding. Therefore, in many cases, postweld treatment of welded joints is required [5–8]. The relevance of fatigue resistance technology has been a priority for engineers for many decades, and

information about their achievements does not leave the pages of technical publications [1–3, 6, 7].

The world practice shows a general trend to search for high-tech methods in order to extend the safe operation of existing metal structures. Systematic studies [7–11] conducted at the E.O. Paton Electric Welding Institute of the NAS of Ukraine and other organisations have shown that advanced methods of welding, high-frequency mechanical forging (HMF) and automation of this process provide high physical and mechanical indices of the strengthened metal layer and at the present stage of development of resource-saving technologies, they are the most effective way to strengthen welded structures operating under cyclic loads.

In view of this, the aim of the study was to obtain comparative test results in determining the impact of arc welding and high-frequency mechanical forging, as well as the accumulation of fatigue damage on the physical and mechanical properties of welded joints and their resistance to brittle fracture.

RESEARCH PROCEDURE

The object of research was welded joints of low-alloy structural S420NL steel of the following chemical composition, %: 0.18 C; 0.58 Si; 1.01 Mn; 0.6 Ni; 0.11 Mo; 0.22 Cr; 0.17 V; 0.05 Nb; 0.48 Cu; 0.011 S; 0.018 P. During their welding in CO_2 , Filarc PZ 6114 S flux-cored welding wire of 1.2 mm diameter was used, which ensures equal strength of the weld

metal with the base metal in terms of static strength indices. The welding mode of butt joints of the specified steel of 14 mm thick with a V-shaped edge preparation was the following: $I_w = 190\text{--}210$ A; $U_a = 26\text{--}28$ V; $V_w = 14\text{--}16$ m/h.

Postweld HMF was performed according to the practiced technology with the parameters of static loading (tool clamping) $C = 150\text{--}200$ N with the frequency and amplitude of transducer oscillations of 27 kHz and $\alpha = 15$ μm and the longitudinal feed rate of the deforming tool $V = 25$ mm/s. A narrow area of the metal of the fusion line of the joint with the formation of a smooth groove of 2.0–2.5 mm wide and up to 1.0 mm deep after forging was subject to treatment.

An integrated approach of modern methods of light (Versamet-2, Neophot-32) and transmission electron microscopy (JEM-200SX, JEOL, Japan) was used to conduct experimental studies. Microhardness was measured using a LECO M-400 microhardness tester with a load of 100 g. The specimens for metallographic examinations were prepared according to standard procedures using diamond pastes of different dispersion. The microstructure was revealed by chemical etching in a 4 % alcohol solution of nitric acid.

To test the impact toughness of the heat-affected zone (HAZ) of welded joints, the specimens were made in accordance with DSTU EN ISO 9017:2015. The test results were used to assess the effect of HMF on the change in KCV indices at test temperatures down to -40 $^{\circ}\text{C}$.

The ability of the metal to resist brittle fracture was determined using the approaches of fracture mechanics, according to which the specimens were used, preliminarily cut out from welded joints with a thickness of 10 mm with an induced fatigue crack at an apex of the notch in the initial state and after HMF. Then, under static bending loading, the critical stress intensity factor K_q was determined. Fracture mechanics formulas were used to determine the values of the critical stress intensity factor. The previously established dependence was taken into account, stating that with an increase in the values of K_q , the sensitivity to stress concentration decreases and the resistance of the metal to brittle fracture grows, or vice versa, with a decrease in the factor, the resistance drops.

Fatigue tests were carried out on 14 mm thick welded joints in the initial state and after HMF under cyclic bending loading. The welded joints were loaded at a frequency of 14 Hz at a symmetrical cycle stress of 100 MPa. The UMP-1 machine was used for the tests. During the tests, a number of cycles was recorded, at which a fatigue crack of critical length (3 mm) was initiated and the stress was formed at which the specimens remained undamaged after $2.1 \cdot 10^6$ load cycles.

RESULTS AND DISCUSSION

As a result of the impact toughness tests, it was found that the KCV indices for the HAZ near-weld metal in the case of high-frequency mechanical forging and without it are almost similar, but after HMF they are somewhat higher. Thus, at a test temperature of $+20$ $^{\circ}\text{C}$, they are in the range of 319–327 J/cm², at -20 $^{\circ}\text{C}$ — 281–290 J/cm², at -40 $^{\circ}\text{C}$ — 238–250 J/cm² (see Table 1).

Light microscopy showed that the structure of the base metal of S420NL steel is ferrite-pearlite with a grain size of $D_{gr} \sim 10\text{--}30$ μm and a microhardness of $HV_{0.1} \sim 1600\text{--}1700$ MPa. In a multi-pass welded joint without HMF treatment, the weld metal has a ferrite-pearlite (F + P) structure. In the upper pass, the microhardness is $HV \sim 1650$ MPa with a globular grain size $D_{gr} \sim 10\text{--}50$ μm and dendrites $hx1 = 50\text{--}200 \times 150\text{--}550$ μm . In the lower pass, $HV_{0.1} \sim 1600\text{--}1700$ MPa, the grain is also globular of the size $D_{gr} \sim 10\text{--}50$ μm and dendrites $hx1 = 50\text{--}100 \times 150\text{--}450$ μm .

In HAZ, a bainite structure (B) is observed, and when approaching the base metal, the F + P structure is observed. The size of the packages decreases from $D_{gr} \sim 40\text{--}200$ μm (HAZ overheating area) to $D_{gr} \sim 5\text{--}39$ μm (HAZ recrystallisation area). At the same time, $HV_{0.1}$ decreases, respectively, from 2210–2740 MPa to 1990–2280 MPa.

Compared to the initial state after HMF, at a depth of 125 μm from the surface of the specimen, the structure in the above HAZ regions of the welded joint is refined to $D_{gr} \sim 15\text{--}100$ μm (HAZ overheating area) and $D_{gr} \sim 5\text{--}30$ μm (HAZ recrystallisation area), while the $HV_{0.1}$ values grow by an average of 1.2 times — up to 3090 MPa and 2360, respectively (Figure 1).

Table 1. Impact toughness of the HAZ metal in welded joints of S420NL steel produced using Filarc PZ 6114 S flux-cored wire in CO₂

No.	Postweld treatment	KCV, J/cm ² , at temperatures, $^{\circ}\text{C}$		
		+20	−20	−40
1	Initial state	315–322	275–287	227–252
		319	282	238
2	High-frequency mechanical forging	325–330	281–298	235–262
		327	290	250

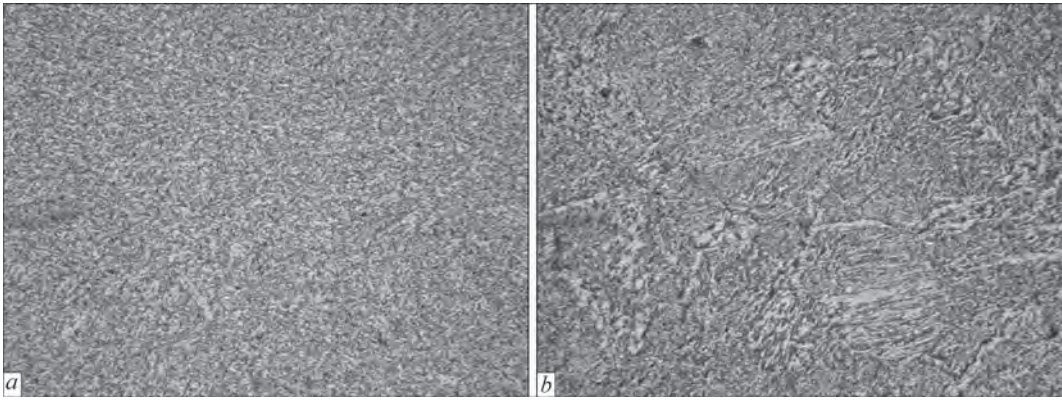


Figure 1. Microstructure ($\times 500$) of the weld metal (a) and HAZ (b) of the welded joint of S420NL steel produced using Filarc PZ 6114 S wire in CO_2 after HMF

The TEM method has found that a substructure ($0.3\text{--}1.5\text{ }\mu\text{m}$) is formed in the weld metal. The density of dislocations (ρ) in the weld metal structure is in average $\rho = 3\text{--}6 \cdot 10^9\text{ cm}^{-2}$. A lath bainite structure is formed in the heat-affected zone. The upper bainite has a lath thickness of $h_1 = 0.3\text{--}1.1\text{ }\mu\text{m}$ with a substructure of the size $d_s = 0.16\text{--}0.3 \times 0.35\text{--}1\text{ }\mu\text{m}$ at

a dislocation density of $\rho = 4\text{--}6 \cdot 10^{10}\text{ cm}^{-2}$. The lower bainite has the size of $h_1 = 0.5\text{--}1.3\text{ }\mu\text{m}$ with $d_s = 0.15\text{--}0.4 \times 0.25\text{--}0.9\text{ }\mu\text{m}$ at a dislocation density of $\rho = 2\text{--}5 \cdot 10^{10}\text{ cm}^{-2}$.

Thus, it was found that in the metal of the welded joint of S420NL steel using Filarc PZ 6114 S wire, relatively small gradients in the weld metal and HAZ

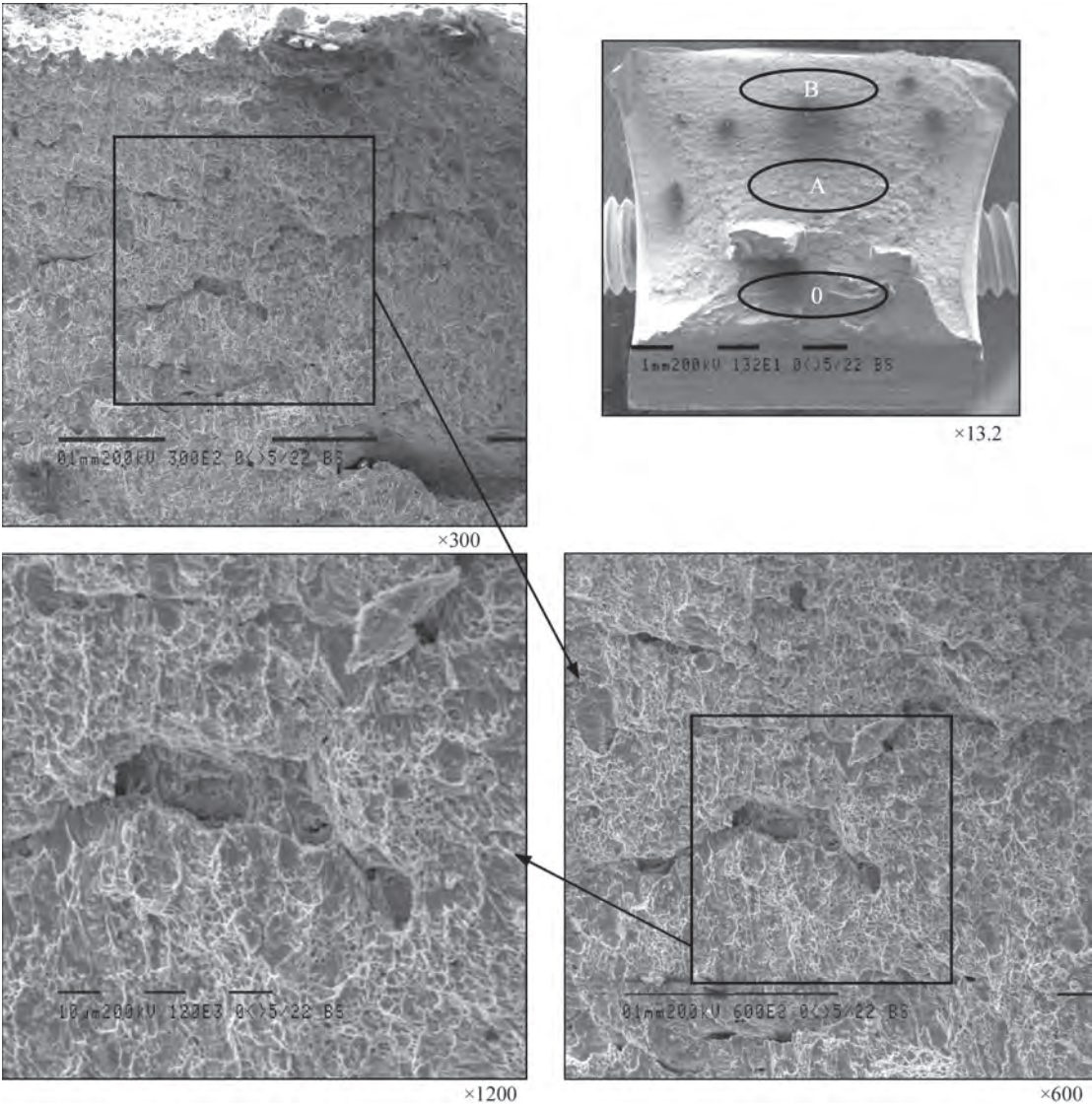


Figure 2. Photo with a fracture of welded joint specimens after impact bending test at $+20\text{ }^\circ\text{C}$ (zone of slow crack propagation)

in terms of dislocation density and formation of sub-structural components are observed, which will probably provide the crack resistance, as well as strengthening of the weld and HAZ areas.

Fractographic examinations of the welded joints after the impact toughness tests at temperatures of +20, -20, and -40 °C were performed using the scanning electron microscopy method for characteristic

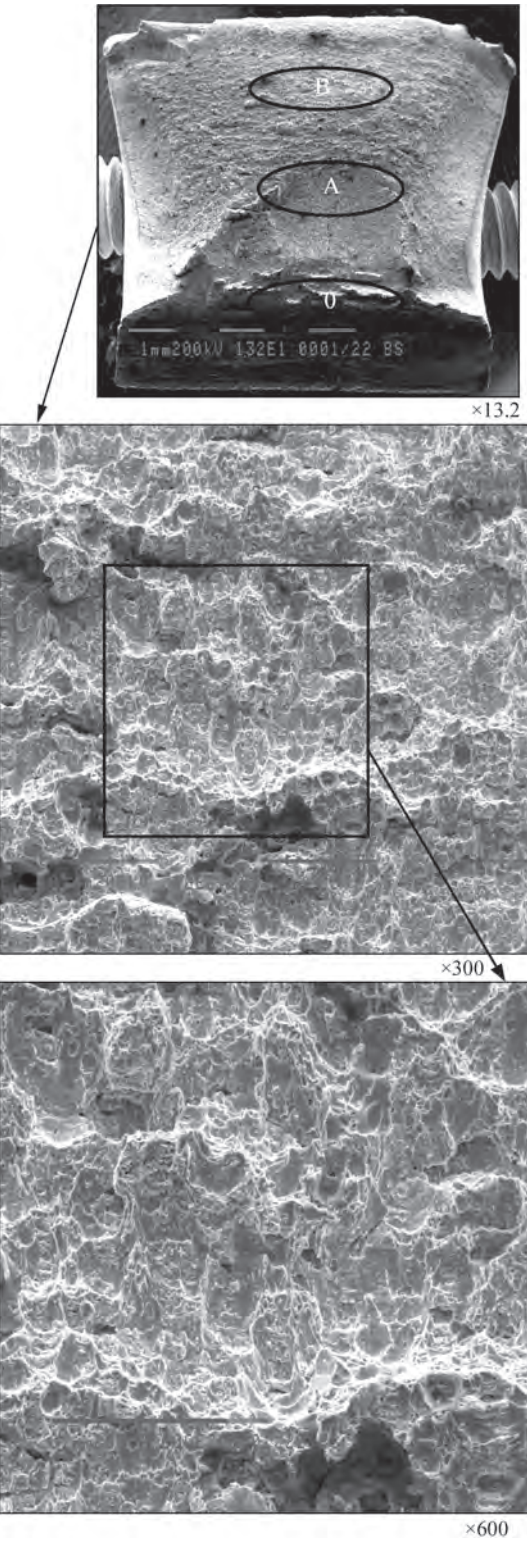


Figure 3. Photo with a fracture of welded joint specimens after impact bending test at -40 °C (zone of slow crack propagation)

fractures (near the notch — slow crack propagation; main crack propagation, ultimate fracture and side bevels). For all the studied fractures, the following was shown: fracture occurred over the HAZ metal, the fracture pattern is ductile with a pitted microrelief. In the zones of slow crack propagation, delamination and isolated secondary microcracks are observed (Figures 2, 3). No defects, ultimate fracture and side bevels were found in the zones of main crack propagation at all test temperatures. This indicates high crack resistance of the metal and is confirmed by high impact strength indices (see Table 1). Based on the results of the research on resistance to brittle fracture, the following was established. In the initial state, welded joints of S420NL steel without HMF treatment during the tests of the HAZ metal, have K_q indices at a level of 95.8 MPa√m at a test temperature of +20 °C, 92.4 MPa√m at -20 °C and 86.7 MPa√m at -40 °C (Figure 4). The values of the stress intensity factor for the HAZ metal after HMF of the welded joints are somewhat higher. Depending on the test temperature, they are 97.1, 93.5, and 89.1 MPa√m, respectively. An increase in the resistance to brittle fracture of the HAZ metal of welded joints of S420NL steel as a result of HMF is within 2.5 %.

The results of the carried out studies on fatigue resistance indicate that the welded joint specimen of S420NL steel in the initial state was affected by a fatigue crack with a critical length of 3 mm after 14,200,000 loading cycles. In contrast, the specimens subjected to HMF remained undamaged after $N = 2.1 \cdot 10^6$ load cycles. It can be assumed that an increase in the fatigue resistance of welded joints of S420NL steel occurred as a result of changes in the structure in the near-surface layer on the fusion line and in the HAZ metal.

From the literature [11–13] and from the practice of operation of welded structures of different purposes, it has been found that fatigue damage can accumulate in the most loaded assemblies. It causes pre-

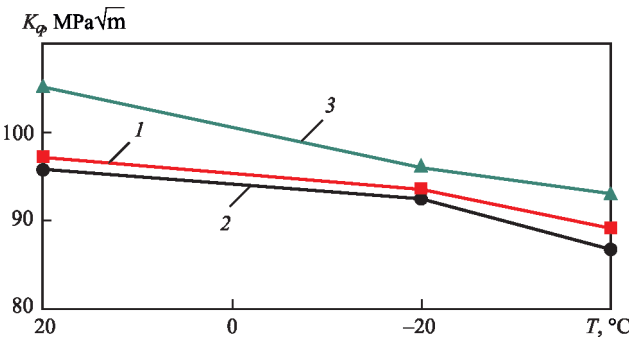


Figure 4. Dependence of the critical stress intensity factor K_q on the test temperature of the HAZ metal of welded joints of S420NL steel: 1 — with HMF; 2 — without HMF; 3 — base metal for comparison

ture cracking, which in turn significantly reduces the cyclic durability of damaged elements in the structure as a whole. Therefore, the paper also studied the effect of the level of accumulated fatigue damage on the resistance to brittle fracture in the HAZ metal of the butt welded joints made with the above welding consumables. The difference from the tests discussed earlier was that the specimens were first subjected to cyclic loading with a different number of cycles. In our case, it was $N = 800,000$ and $N = 1,200,000$, which is 60 and 80 % of the total number of load cycles, at which (see above) fatigue cracks are formed (1,420,000 cycles). Based on the research results, it was found that with an increase in the level of accumulated damage, the value of the stress intensity factor K_q decreases slightly but remains at a high level (Figure 5). Thus, at a test temperature of $+20\text{ }^{\circ}\text{C}$, with an increase in the level of accumulated damage from 60 to 80 %, the values of the factor drop from 96 to 94.5 $\text{MPa}\sqrt{\text{m}}$, and at a temperature of $-40\text{ }^{\circ}\text{C}$ — from 83.5 to 81.9 $\text{MPa}\sqrt{\text{m}}$, respectively.

It is obvious that a decrease in the resistance of HAZ metal of welded joints to brittle fracture occurs as a result of changes in the metal structure under long-term loads.

The conducted structural examinations show that as a result of long-term cyclic loading, certain changes occurred in the HAZ metal structure of the welded joint of S420NL steel associated with the formation of local band structures. This indicates the propagation of dislocation redistribution processes in this zone. At the same time, no changes occur in the phase composition, grain size and microhardness. Thus, as noted above, in the overheating area of HAZ joints, there is a bainite structure with a microhardness of 1870–2450 MPa, the size of the packages is 40–200 μm .

The pattern of fracturing metal of welded joints after accumulation of fatigue damage at a number of 1,200,000 load cycles at temperatures from $+20\text{ }^{\circ}\text{C}$ to $-40\text{ }^{\circ}\text{C}$ was studied by the scanning electron microscopy.

At a temperature of $+20\text{ }^{\circ}\text{C}$ in the zone of main crack propagation, the fracture pattern is mainly ductile ($V_{\text{fr}} = 85\text{--}90\text{ } \%$). There are no small pits on the surface with a size of $d_p = 0.5\text{--}5\text{ } \mu\text{m}$ and large ones with a size of $d_p = 8\text{--}30\text{ } \mu\text{m}$. There are also areas of quasi-brittle fracture ($V_{\text{fr}} = 10\text{--}15\text{ } \%$) with the size of quasi-spall facets $d_f \sim 5\text{--}25\text{ } \mu\text{m}$.

When the test temperature is lowered to $-20\text{ }^{\circ}\text{C}$, the volume fraction of brittle fracture grows to $V_{\text{fr}} = 30\text{--}35\text{ } \%$, the size of the quasi-spall facets does not change.

At a test temperature of $-40\text{ }^{\circ}\text{C}$, the volume fraction of brittle fracture grows to $V_{\text{fr}} = 60\text{--}65\text{ } \%$, the size of the quasi-spall facets does not change ($d_f \approx 5\text{--}25\text{ } \mu\text{m}$).

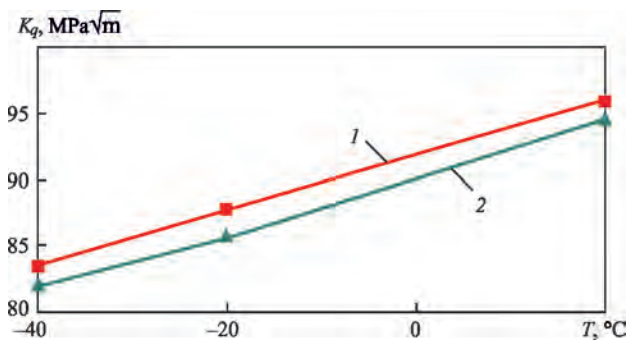


Figure 5. Influence of fatigue damage accumulation on the resistance to brittle fracture in the HAZ metal of welded joints of S420NL steel: 1 — 60 % of accumulated damage $N = 800,000$ cycles); 2 — 80 % of accumulated damage $N = 1,200,000$ cycles)

Also, the metal contains long secondary cracks of $L_{\text{cr}} = 20\text{--}110\text{ } \mu\text{m}$.

Thus, when the test temperature is lowered to $-40\text{ }^{\circ}\text{C}$, a predominantly brittle type of fracture (60–65 %) is observed in the region of the main crack propagation. This is confirmed by a slight decrease (by 12 %) in the fracture toughness from $K_q = 94.5\text{ } \text{MPa}\sqrt{\text{m}}$ ($T_{\text{test}} = 20\text{ }^{\circ}\text{C}$) to $K_q = 82\text{--}85\text{ } \text{MPa}\sqrt{\text{m}}$ (at subzero temperatures), which indicates sufficient crack resistance of welded joints of S420NL steel under operating cyclic loads.

CONCLUSIONS

1. Metallographic examinations found that under the action of HMF at a depth of 125 μm from the surface of the specimen, the bainite structure of the HAZ metal of the welded joint is refined, small gradients in the density of dislocations and the formation of substructural components are observed, while the hardness values grow compared to the initial state. Also, after HMF, the impact toughness of the HAZ metal values of welded joints of S420NL steel is somewhat higher than in the state without forging.

2. It was established that the use of HMF for welded joints of S420NL steel leads to an increase in the resistance of HAZ metal to brittle fracture, as evidenced by a slight increase in the stress intensity factor K_q within the range of up to 0.5 %.

3. The influence of the level of accumulated damage on the resistance of welded joints of S420NL steel to brittle fracture was evaluated. The obtained data indicate that with an increase in the level of damage from 60 to 80 % of the total number of loads, under which fatigue cracks are formed, the value of the factor K_q decreases by 1.5–2.0 %. This can be explained by certain changes in the structure of the HAZ metal of welded joints (without changing the phase composition) associated with the formation of local band structures and the propagation of processes of dislocation redistribution in this zone.

4. It was established that it is possible to increase the fatigue resistance of welded joints of S420NL steel by using HMF after their welding. At the same time, after HMF, the welded joint remains undamaged after $N = 2.1 \cdot 10^6$ load cycles, while without HMF, a fatigue crack of critical length is formed after 1,420,000 cycles.

REFERENCES

1. Kudryavtsev, V.I., Naumchenkov, N.E. (1976) *Fatigue of welded structures*. Moscow, Mashinostroenie [in Russian].
2. Trufiyakov, V.I. (1998) Increasing the fatigue resistance of welded joints and structure. *Avtomaticheskaya Svarka*, **11**, 11–19 [in Russian].
3. Pokhmursky, V.I., Khoma, M.S. (2008) *Corrosion resistance of metals and alloys*. Lviv, SPOLOM [in Ukrainian].
4. Knysh, V.V., Solovej, S.A., Kyrian, V.I. et al. (2017) Application of high-frequency peening to improve the performance of butt welded joints in the atmosphere of temperate climate. *The Paton Welding J.*, **4**, 14–18. DOI: <https://doi.org/10.15407/tpwj2017.04.03>
5. Degtyarev, V.A. (2011) Assessment of the high-frequency mechanical forging mode effect on fatigue strength of welded joints. *Strength Mater.*, **43**, 154–160. DOI: <https://doi.org/10.1007/s11223-011-9281-1>
6. Nekhoroshkov, O.N., Pershin V.P., Semukhin B.S. (2006) Application of the method of ultrasonic impact treatment for welded joints of structural steels. *Bulletin of TSUACE*, **2**, 120–125 [in Russian].
7. Knysh, V.V., Kuzmenko A.Z., Vojtenko O.V. (2006) Increasing fatigue resistance of welded joints by high-frequency mechanical peening. *The Paton Welding J.*, **1**, 30–33.
8. Zhang, H., Wang, D., Xia, L. et al. (2015) Effects of ultrasonic impact treatment on pre-fatigue loaded high-strength steel welded joints. *Inter. J. of Fatigue*, **80**, 278–287. DOI: <https://doi.org/10.1016/j.ijfatigue.2015.06.017>
9. Panin, V.E., Kablov, E.N., Pleshanov, V.S. (2006) Effect of ultrasonic impact treatment on the structure and fatigue resistance of welded joints of high-strength steel VKS-12. *Fizicheskaya Mezomechanika*, **3**, 85–96 [in Russian].
10. Lobanov, L.M., Kirian, V.I., Knysh, V.V., Prokopenko, G.I. (2006) Improvement of fatigue resistance of welded joints in metal structures by high-frequency mechanical peening (Review). *The Paton Welding J.*, **9**, 2–8.
11. Knysh, V.V., Solovej, S.A., Kuzmenko, A.Z. (2011) Influence of preliminary cyclic loading on effectiveness of welded joint strengthening by high-frequency peening. *The Paton Welding J.*, **10**, 36–39.
12. Knysh, V.V., Solovej, S.A., Kuzmenko, A.Z. (2012) Improvement of fatigue resistance of welded joints with accumulated damage under multistage and block loading. *The Paton Welding J.*, **7**, 19–23.
13. Knysh, V.V., Kuzmenko, A.Z., Solovej, S.A. (2009) Accumulation of fatigue damage in tee welded joints in as-welded and after high-frequency peening under block loading. *Machynoznavstvo*, **9**, 27–31.

ORCID

S.L. Zhdanov: 0003-3570-895X,
O.A. Haivoronsky: 0000-0002-5922-5541,
V.D. Poznyakov: 0000-0001-8581-3526,
A.V. Zavdoveev: 0003-2811-0765

CONFLICT OF INTEREST

The Authors declare no conflict of interest

CORRESPONDING AUTHOR

S.L. Zhdanov
E.O. Paton Electric Welding Institute of the NASU
11 Kazymyr Malevych Str., 03150, Kyiv, Ukraine.
E-mail: patonlab48@ukr.net

SUGGESTED CITATION

S.L. Zhdanov, O.A. Haivoronsky, V.D. Poznyakov, A.V. Zavdoveev, A.M. Gerasymenko, R.V. Bogodist (2025) Impact of arc welding and high-frequency mechanical forging on the mechanical properties and resistance to brittle fracture of welded joints of S420NL steel. *The Paton Welding J.*, **6**, 3–8.
DOI: <https://doi.org/10.37434/tpwj2025.06.01>


JOURNAL HOME PAGE

<https://patonpublishinghouse.com/eng/journals/tpwj>

Received: 29.01.2025

Received in revised form: 22.04.2025

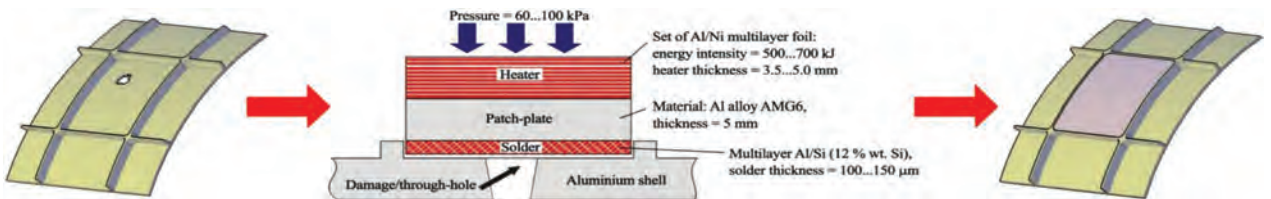
Accepted: 25.06.2025



Developed at PWI

**TECHNOLOGY FOR REPAIRING ALUMINIUM SHELLS
IN SPACE USING SHS ASSISTANCE REACTION SOLDERING**

Large aluminium shells used in space can be damaged. Proposes a scheme for repairing shells by attaching flat linings to them by reaction soldering. In the example of AMg6 alloy plates, the fundamental possibility of joining aluminium alloys by local heating of the connection zone with heat generated in reaction multilayer foils when initiating a self-propagating high-temperature synthesis (SHS) reaction in them is shown.



Pressure = 60...100 kPa

Heater

Patch-plate

Solder

Damage/through-hole

Aluminium shell

Set of Al/Ni multilayer foil:
energy intensity = 500...700 kJ
heater thickness = 3.5...5.0 mm

Material: Al alloy AMG6,
thickness = 5 mm

Multilayer Al/Si (12 % wt. Si),
solder thickness = 100...150 μm

For more information, please follow the links: <http://dx.doi.org/10.15407/tpwj2019.04.03>; <https://doi.org/10.37434/tpwj2023.10.03>

DISPERSED OXIDES INFLUENCE ON THE KINETICS OF THE WELD METAL STRUCTURAL TRANSFORMATIONS

V.V. Holovko, V.A. Kostin, V.V. Zhukov

E.O. Paton Electric Welding Institute of the NASU

11 Kazymyr Malevych Str., 03150, Kyiv, Ukraine

ABSTRACT

Research was conducted to study the influence of inoculation of the aluminium, titanium, magnesium, and zirconium dispersed refractory oxides into the weld pool on the modification of the metal structure in low-alloy steel welds. It is shown that the inoculation of refractory oxides into the weld pool increases the temperature at which the bainitic transformation ends and significantly reduces its temperature range. This trend coincides with the size of the wetting angle between the oxide and liquid iron. Increasing the content of inoculants in the weld pool liquid metal from 0.1 to 0.2 % affects the temperatures of the start and finish of the bainitic transformation. Both the start and finish temperatures are increased, that is, the formation of bainite occurs in the higher temperatures region, and the temperature range of this region narrows (the kinetics of transformation increases). An increase in the temperature of the finish of the bainitic transformation and a reduction in its temperature range cause an increase in the acicular ferrite content in the weld metal structure, which corresponds to an increased impact energy level of the weld metal.

KEYWORDS: welding, microstructure, dispersed oxides, weld pool inoculation, bainitic transformation

INTRODUCTION

Improvement of the mechanical properties of welded joints of low-alloy high-strength steels is a relevant problem in the field of welded metal structures. Modern materials science examines the metal modification processes as a leading tool for further development of the scope of low-alloy steel application in manufacture of components, structures and apparatuses designed for operation in extreme conditions. Both the research performed by prominent scientific centers and industrial implementation experience indicate that refractory compound inoculation into the metal melt allows effectively influencing the processes of metal structure formation at the crystallization and recrystallization stages. Application of the currently defined approaches to modification in manufacturing welded metal structures from high-strength low-alloy steels requires expansion of the base of scientific knowledge and concepts as to the influence of dispersed refractory inoculants on development of peritectic processes during formation and development of dendrites in the weld pool, decomposition of the austenite phase with substructure formation and bainitic transformation parameters.

The processes of weld metal modification begin with producing finer austenite grains (γ), which is a necessary condition, as a large number of ferrite grains (α) are formed and grow on γ -grain boundary. In this connection, formation and growth of γ -grains in the matrix, and, hence, also the δ/γ free energy are of particular interest. During crystallization of low-carbon

steel weld pool the phase transition of delta-ferrite into austenite occurs in a thin hard shell in the immediate vicinity of the meniscus. It is well known that many casting defects form in this region, but still very little is known about the morphological development of this important phase transition.

Modification processes are widely used for improvement of the mechanical properties of both the steels proper, and the metal of welds on these steels. By the nature of metallurgical interaction with the metal it is possible to single out two main types of modifiers: refractory and surface-active. A lot of attention was paid to description of the influence of refractory modifiers, forming refractory insoluble particles with the chemical elements of the metal melt, and promoting heterogeneous formation of nuclei of metal crystallization centers. Results of the performed research are summarized in a number of fundamental studies [1–3].

Much less attention was paid to the influence of surface-active modifiers on the processes of formation of the structure in iron-carbon alloys. They are known to deposit in the form of a thin layer on the surface of metal crystal nuclei in the melt, which causes a reduction in surface energy of the interphases in the melt-solid phase system [4]. It results in an increase in the rate of formation of the crystallization centers, which is associated with reduction of the nucleus critical radius, but the metal crystal growth rate decreases [5]. Such a double effect of surface-active modifiers causes a refinement of the dimensions of the crystallized metal structure [6].

The work gives the results of investigations, which were aimed at expansion of the base of scientific knowledge on the peculiarities of the influence of surface-active modifiers on formation of the weld metal structure. In particular, the influence of wetting of the growing dendrite surface by nonmetallic inclusions on metal structure formation was considered. The data presented in the work will be used in development of new welding consumables, and improvement of the currently available technological processes of low-alloy steel welding.

STATE OF THE PROBLEM

In the presence of inhomogeneous particles in the melt or unevenness on the dendrite surface the energy required for formation of new phase nuclei, decreases due to interphase tension between the melt, foreign particles and forming nuclei. Crystalline nuclei form on hard particles, which were in the overcooled melt until they reached the critical size. Heterogeneous nucleation usually occurs at crystallization of the steel melt in the weld pool. This is associated with presence of a large number of foreign particles (endogenous and exogenous inclusions). Refractory nonmetallic inclusions can be the center of heterogeneous nucleation of the dendrites and can influence their development, but here we should take into account the widely known negative influence of nonmetallic inclusions on the mechanical properties of the weld metal. The oxides, such as Al_2O_3 , MgO and TiO_2 , are primary nonmetallic forms, which can be present in the weld pool melt.

Investigations of liquid iron wetting in contact with Al_2O_3 , MgO and TiO_2 , showed that in the case of pure iron the wetting angle and the surface tension are within $105.1\text{--}103^\circ$ and $1500\text{--}1410\text{ m}\cdot\text{N}/\text{m}$ for Al_2O_3 substrate, and $99.2\text{--}90^\circ$ and $1490\text{--}1270\text{ m}\cdot\text{N}/\text{m}$ for MgO substrate, respectively. For Ti_2O_3 substrate the contact angle is somewhat reduced from 128.2 to 122° , and the surface tension has an average value of $1610\text{ m}\cdot\text{N}/\text{m}$. For cases of Al_2O_3 /pure Fe and MgO /pure Fe, formation of a reaction layer on the interface of FeAl_2O_4 and $\text{MgO}\text{--}\text{FeO}$ (solid solution), respectively, leads to reduction of the contact angle and the surface tension. In the case of Ti_2O_3 /pure Fe the interphase reaction cannot take place. As regards the case of Ti_2O_3 /steel, an abrupt reduction in the contact angle and surface tension values are caused by formation of Al_2TiO_5 reaction layer [7–9].

Wetting tests, which were conducted between molten alloy Fe–Cr–Ni and Al_2O_3 , MgO and $\text{MgO}\cdot\text{Al}_2\text{O}_3$ oxide substrates in Ar atmosphere at 1873 K , allowed determination of the contact angles and interphase energies for each substrate composition. It was determined that molten iron has contact angles of 114 , 111

and 117° with Al_2O_3 , MgO and $\text{MgO}\cdot\text{Al}_2\text{O}_3$ substrates, and molten Fe–Cr–Ni alloy has the angles of 105 , 103 and 103° with the same substrates, respectively. The difference in the contact angles points to the fact that the wettability between the molten Fe–Cr–Ni alloy and all the three substrates was higher than that between the molten iron and the substrates. The level of interfacial energy of molten iron is equal to 1862 , 2388 and $2781\text{ m}\cdot\text{N}/\text{m}$ on Al_2O_3 , MgO and $\text{MgO}\cdot\text{Al}_2\text{O}_3$, and for molten Fe–Cr–Ni alloy it is 1513 , 2075 and $228\text{ m}\cdot\text{N}/\text{m}$, respectively [7–9]. The differences in the contact angle are attributable to the influence of interfacial energy. The interfacial energy values calculated by the Young's equation were smaller to a greater extent for molten Fe–Cr–Ni alloy with all the substrate types, than those for molten iron. The differences in the interfacial energy level are attributable to higher reactivity of Fe–Cr–Ni alloy at contact with oxide substrates, than that of pure iron.

THE OBJECTIVE OF THE WORK

was to study the features of the processes of nucleation, growth and development of the precipitated phase morphology during crystallization of the weld pool metal and during phase transformations which are controlled by the free interfacial energy between the refractory oxide particles and the matrix.

MATERIALS AND RESEARCH METHODOLOGY

Investigation of the influence of refractory Al_2O_3 , MgO , TiO_2 and ZrO_2 particles on modification of the structural components of weld metal was performed on deposited metal samples, cut out of the last layer of the metal of a butt weld made with experimental flux-cored wire OERLIKON Fluxcord 35.22 of “metal core” type $4.0\pm 0.1\text{ mm}$ in diameter under a layer of ST65 flux to ISO 14171 standard [10]. Physical-chemical parameters of the joints selected for the experiments are given in Table 1.

Samples of the deposited metal were produced by the method of automatic welding using KA-001 welding tractor and KIU-1200 power source. Welding was performed with reverse polarity direct current of $500\text{--}520\text{ A}$, at arc voltage of $34\text{--}36\text{ V}$ and welding speed of $43\pm 1\text{ m}/\text{h}$. After each pass the butt joint was cooled in air to the temperature of not more than 120°C . Energy input of welding was equal to $13\text{--}15\text{ kJ}/\text{cm}$.

Refractory compound particles of $200\text{--}500\text{ }\mu\text{m}$ size were added (inoculated) to the molten metal through the core of 1.6 mm flux-cored wire fed to the weld pool in the form of “cold” filler. Filler flux-cored wire was made from a strip of 08Yu grade steel of $0.8\times 12\text{ mm}$ size. The charge for the core filling was produced

Table 1. Physical and chemical characteristics of the compounds used in the experiments

Compound	$T_{\text{melting}}, ^\circ\text{C}$	Crystalline lattice type	Lattice parameter, nm	δ -Fe size mismatch, %	Interfacial energy, mJ/m ²
ZrO ₂	2715	Tetragonal	α — 3.640, c — 5.152	1	2863
MgO	2825	FCC	α — 4.213	14	2226
TiC	3160		α — 4.336	18	884
TiO ₂	1843	Tetragonal	α — 4.593, c — 2.959	25	2444
Al ₂ O ₃	2044	Rhombohedral	α — 5.120 (55.25°)	39	972

from a mixture of iron powder of PZhm grade with inoculants. The inoculant content was equal to 10 % for welds with Al₂O₃*, MgO*TiO₂* and ZrO₂* marking and 20 % for welds with Al₂O₃**, MgO**, TiO₂** and ZrO₂** marking. Strip filling factor was kept in the range of 18–20 %. Schemes of preparation of the butts, welded joint and locations of taking the samples for investigations are given in Figures 1, 2.

Metallographic investigations of the last pass were conducted in optical microscope Neophot 32 on transverse sections of the weld metal, polished and etched in a 2 % solution of nitric acid in alcohol (Nital). The same sections were used for investigation in a scanning electron microscope. Microstructure analysis was conducted in keeping with the requirements of EN ISO 17639 standard [11] and recommendations of IIW [12]. The primary weld structure was studied on polished samples, etched in a boiling saturated solution of sodium picrate (C₆H₂(NO₂)₃ONa) in water.

Structural parameters were determined with application of MIPAR image analysis software (USA) v.4.2.1, which uses the technology of deep learning with application of artificial intelligence (AI). It allows teaching the software to adapt to analysis of the obtained microphotographs, characterized by different contrast, brightness, dimensions of structural elements and features of the texture, as well as the technique of sample preparation for investigations.

In the latter versions of MIPAR program (higher than v.4.2) a large library of recipes is used to determine the grain size, volume fraction and distribution by phase and inclusion dimensions, as well as the

structure orientation and heterogeneity, texture features, etc. Standard recipes of the MIPAR program were used in the work to determine the size and branching of the grain boundaries in low-alloy steels.

The nature of structural transformations in the alloyed weld metal was studied by simulation of the themodeformational welding cycle (TDWC) in Gleeble 3800 complex, fitted with a high-speed dilatometer. Investigations were performed using a cylindrical samples 6 mm in diameter and 80 mm long, made from deposited metal 20 mm thick. According to the methodology developed at PWI, the samples were heated by a preset program in the vacuum chamber up to a temperature of 1170 °C, and then cooled by different thermal cycles with different cooling rates. The cooling curves corresponded to Newton–Richman dependence and cooling rates of 5; 10; 17; 30; 45 °C/s in the temperature region of 500–600 °C. The cooling parameters of the thermal welding cycles (thermal and time) in the welded joint metal were reproduced quite accurately.

INVESTIGATION RESULTS

Tables 2–4 give the results of studying the chemical composition, microstructure and results of dylatometric studies of the weld metal, where: WMWI is the weld metal without inoculants.

INVESTIGATION RESULTS

The movement of the solid/liquid interface at weld pool metal crystallization is characterized by a no-

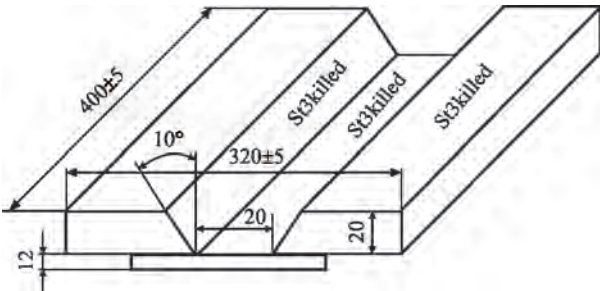


Figure 1. Scheme of butt joint preparation to cut out weld metal samples in accordance with ISO 14 [7]

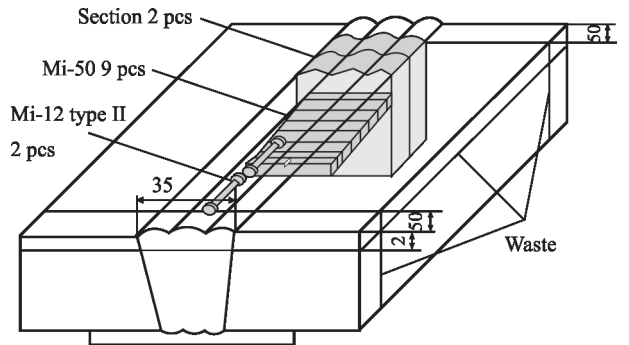


Figure 2. Scheme of taking samples for determination of the chemical composition, mechanical properties and structure of the weld metal

Table 2. Chemical composition of the weld metal

Weld	C	Si	Mn	S	P	Cr	Ti	Al	Zr
WMWI	0.053	0.37	1.60	0.008	0.016	0.37	<0.01	~0.004	N/D
Al ₂ O ₃ [*]	0.060	0.27	1.43	0.014	0.012	0.35	<0.01	0.006	
MgO [*]	0.061	0.42	1.50	0.014	0.012	0.41	<0.01	0.005	
TiO ₂ [*]	0.047	0.26	1.48	0.012	0.014	0.40	0.012	0.008	
ZrO ₂ [*]	0.061	0.42	1.53	0.017	0.014	0.40	<0.01	0.006	0.007
Al ₂ O ₃ ^{**}	0.024	0.26	1.40	0.009	0.014	0.38	0.011	0.009	0.002
MgO ^{**}	0.029	0.34	1.40	0.015	0.019	0.32	0.018	0.010	0.005
TiO ₂ ^{**}	0.020	0.28	1.40	0.010	0.014	0.30	0.012	0.008	0.001
ZrO ₂ ^{**}	0.024	0.36	1.40	0.015	0.019	0.35	0.014	0.008	0.006

Table 3. Phase fraction and primary crystallite size in weld metal samples

Weld	Phase fraction, %					Primary crystallite size, μm
	AF	PF	Ph	WF	P	
WMWI	95	2.6	2.4	–	–	120–160
Al ₂ O ₃ [*]	50.4	16.1	28.4	–	5.1	68–77
MgO [*]	84.0	9.3	6.7	–	–	100–125
TiO ₂ [*]	91.3	3.7	2.0	3.0	–	115–155
ZrO ₂ [*]	84.3	7.3	6.7	1.7	–	50–90
Al ₂ O ₃ ^{**}	67.1	13.8	7.2	8.9	3.0	140–200
MgO ^{**}	73.5	11.0	7.0	5.5	3.0	100–210
TiO ₂ ^{**}	56.5	16.2	15.0	10.7	1.5	60–100
ZrO ₂ ^{**}	55.0	18.0	12.0	12.0	3.0	150–280

Note. AF — acicular ferrite; PF — polygonal ferrite; Ph — polyhedral ferrite; WF — Widmanstaetten ferrite; P — pearlite.

Table 4. Results of dylatometric analysis of the weld metal

Weld	Ac ₃	Ac ₁	B _s	B _f	Δγ	Δα
WMWI	909	718	707	449	191	257
Al ₂ O ₃ [*]	909	718	749	542	191	206
MgO [*]	907	725	726	497	182	229
TiO ₂ [*]	908	722	722	494	187	228
ZrO ₂ [*]	905	723	714	487	181	227
Al ₂ O ₃ [*]	933	725	756	540	208	215
MgO ^{**}	933	720	766	528	213	238
TiO ₂ ^{**}	933	725	756	540	208	215
ZrO ₂ ^{**}	933	724	766	541	209	224

Note. Ac₃ and Ac₁ are the temperatures of the start and finish of primary austenite decomposition; B_s and B_f are the temperatures of the start and finish of the bainitic transformation; Δγ and Δα is the temperature range of primary austenite decomposition and bainitic transformation.

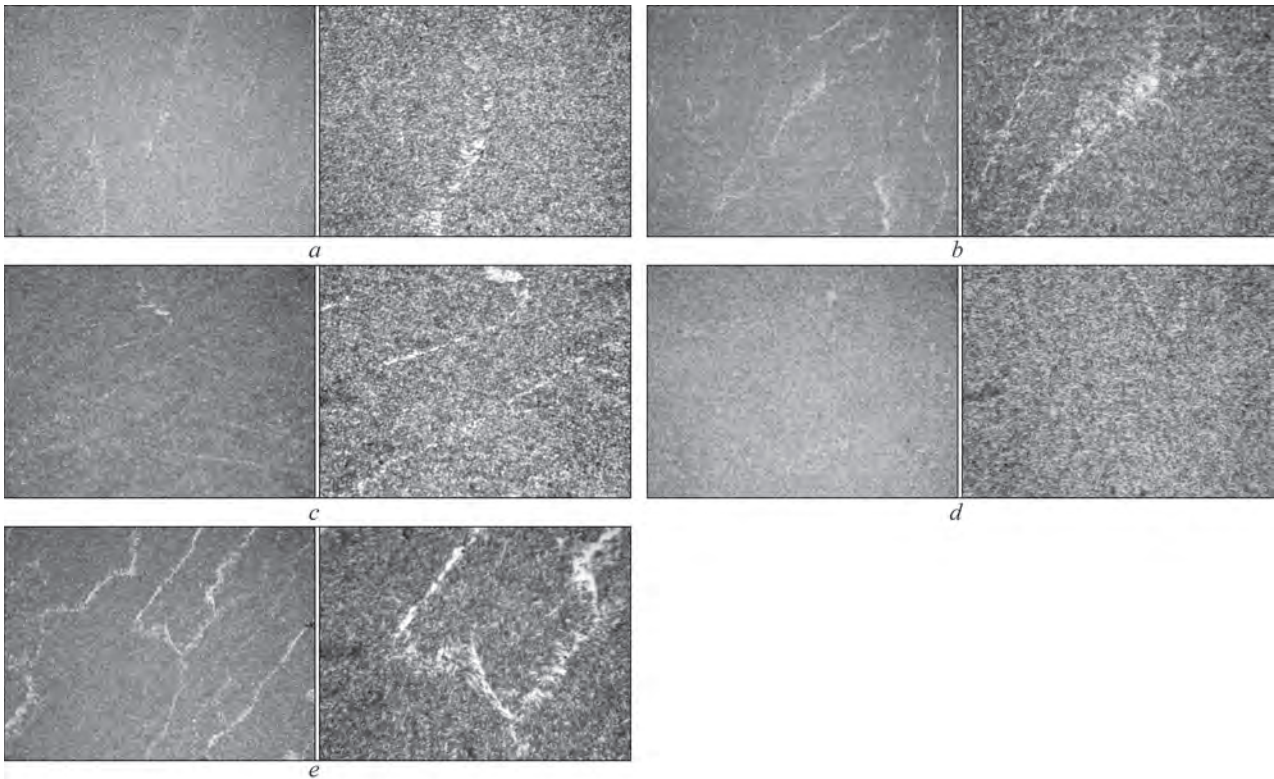


Figure 3. Weld metal microstructure with 0.1 % inoculation: *a* — weld metal without inoculations; *b* — MgO*; *c* — ZrO₂*; *d* — Al₂O₃*; *e* — TiO₂*; left (×200), right (×500)

ticeable unevenness. In places with a higher level of overcooling the growth of a dendrite in the form of a sharpened peak is initiated. The speed of movement of the dendrite tip in a metal melt and the dendrite size are determined by the surface energy on the solid/liquid interface. Refractory nonmetallic inclusions, which meet with the dendrite tip during its movement in the metal melt, are sorbed on this surface, influencing its energy level. Investigations of the influence of energy distribution anisotropy on the interface on the grain structure formation showed the existence of a reverse dependence between these parameters, namely during crystallization a lowering of the interfacial energy level in the metal promotes an increase in the grain size [7].

The processes of dendrite decomposition are associated with a decrease in the grain boundary energy. Changes in the energy of dendrite grain boundaries have an indirect influence on the distribution of γ -ferrite grain sizes in the metal. Based on comparative analysis of the anisotropy of grain size distribution and anisotropy of grain boundary energy it was shown that there exists a reversible dependence between these two values in polycrystals that envisages the ex-

istence of a relatively larger quantity of grains with low boundary energy, than in the case of high-energy grain boundaries [7, 8]. Thus, a change in the type of the intergranular interlayer in a sample, which leads to a change in the grain boundary energy, also influences the changes in the grain size during transformation. Influence of the presence of refractory oxides in the solid solution on the processes of crystallization and recrystallization of the weld metal was studied on samples prepared by the above described procedure.

Samples of metal microstructure of welds inoculated with MgO, ZrO₂, Al₂O₃ and TiO₂ compounds in the amount of 0.1 %, as well as of weld metal without inoculants, are shown in Figure 3.

As one can see from the data given in Figure 4, inoculation of refractory oxides to the weld pool promotes an increase in the temperature of the finish of bainitic transformation and essentially lowers its temperature range. This trend coincides with the influence of the size of wetting angle between the oxide and liquid iron on the transformation temperatures, as was noted above. A certain deviation from such a dependence was noted only for the welds, modified by titanium oxides TiO₂.

In work [7] such a feature is associated with the fact that for TiO₂ in contact with liquid iron, the melting region forms at the temperature below the melting temperature of pure iron, which is associated with a strong trend to formation of TiO₂–FeO compounds (solid solution). The kinetics of this process is deter-

Table 5. Contact angle of wetting the refractory oxides by the iron melt [9]

Oxide	MgO	ZrO ₂	Al ₂ O ₃	TiO ₂
Angle of wetting by Fe-armco	128	123	42	5

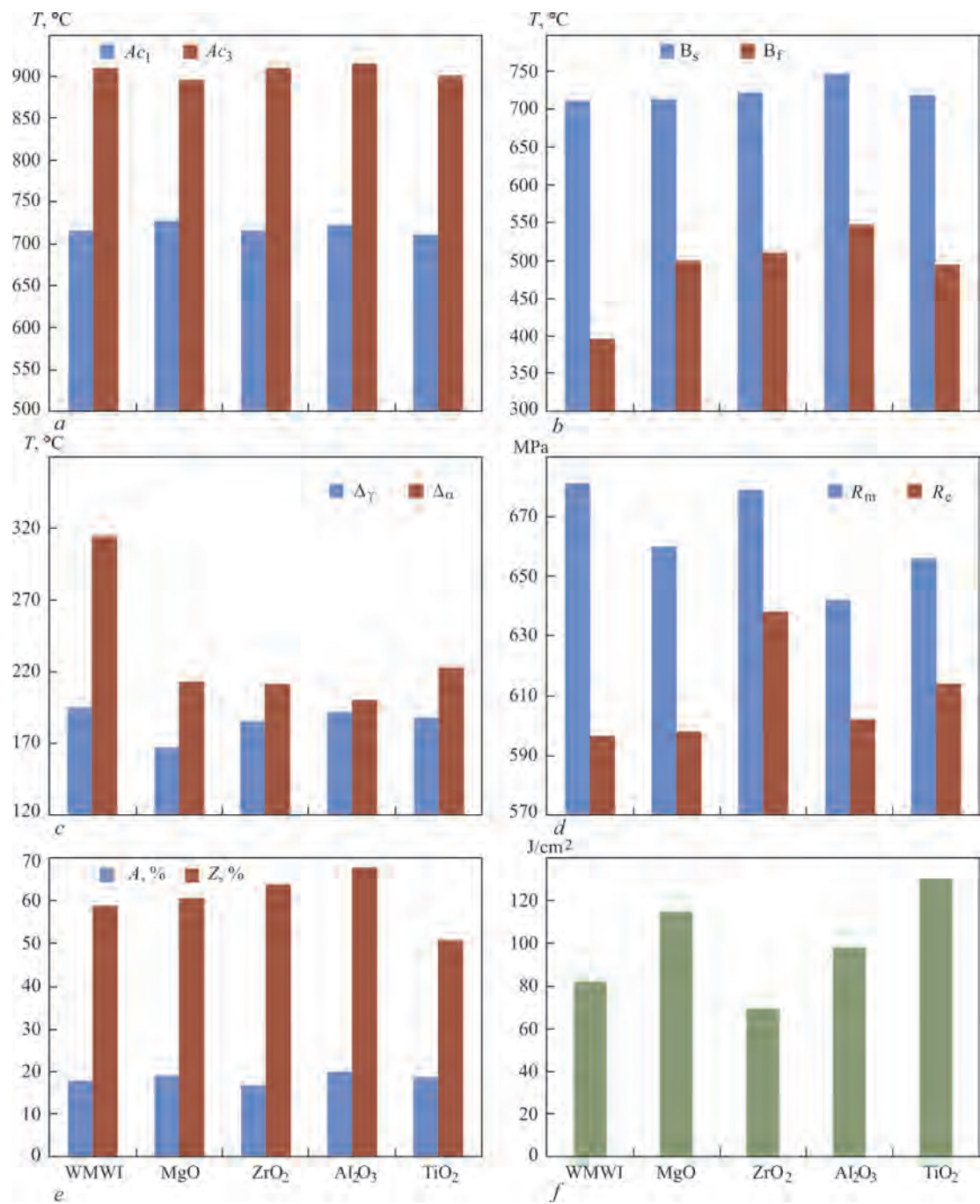


Figure 4. Influence of inoculation of 0.1% refractory oxides to the weld pool on structural transformations and mechanical properties of the weld metal: *a* — temperatures of the start (Ac_3) and finish (Ac_1) of primary austenite decomposition; *b* — temperatures of the start (B_s) and finish (B_f) of bainitic transformation; *c* — temperature ranges of austenite decomposition ($\Delta\gamma$) and bainitic transformation ($\Delta\alpha$); *d* — ultimate strength (R_m) and yield limit (R_e) of the weld metal; *e* — relative elongation (A) and reduction in area (Z) of the weld metal; *f* — impact toughness of weld metal at $-20\text{ }^\circ\text{C}$ test temperature

mined by direct reactions between pure iron, TiO_2 (s) and gaseous oxygen. The main source of oxygen for such a reaction is TiO_2 decomposition and low partial pressure of oxygen in the solution.

For Al_2O_3 and MgO which are in contact with liquid iron, formation of the reaction layer of FeAl_2O and $\text{MgO}\cdot\text{FeO}$ on the interface, accordingly, leads to reduction of the contact angle, but the kinetics of these processes is slower, so that a change in the contact angle can take place with time [8].

Refractory magnesium and zirconium oxides have rather high angles of wetting with liquid iron, unlike titanium and aluminium oxides (Table 5), which readily wet the growing dendrite surface.

Samples of metal microstructure in welds inoculated with MgO , ZrO_2 , Al_2O_3 , and TiO_2 compounds in the amount of 0.2 %, are given in Figure 5.

RESULT ANALYSIS

Differences in the process of formation of the dendrites, primary and secondary structure of metal in the

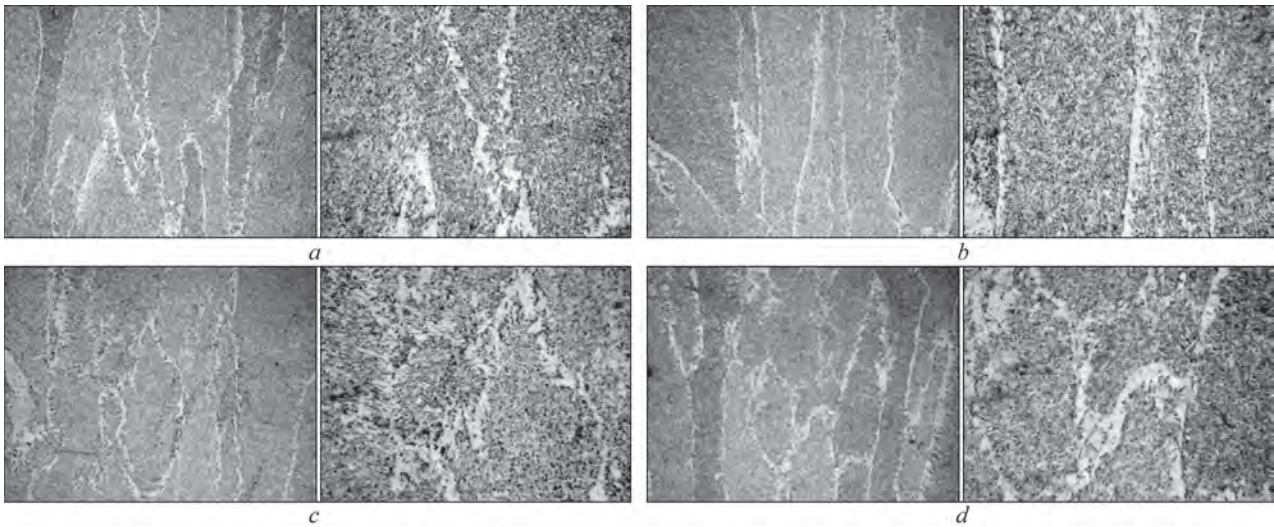


Figure 5. Weld metal microstructure with 0.2 % inoculation: *a* — MgO^{**}; *b* — ZrO₂^{**}; *c* — Al₂O₃^{**}; *d* — TiO₂^{**}; left (×200), right (×500)

welds inoculated by dispersed particles of refractory compounds, should be related to the features of interphase interaction of the dispersed refractory particles with different morphological formations of the solid phase, appearing in the weld metal at cooling. Weld pool inoculation with refractory particles of magnesium oxide, having rather high angles of wetting with liquid iron, is accompanied by an increase in the temperature of completion of primary crystallization, leading to narrowing of the temperature range of $\delta \rightarrow \gamma$ -transformation. It results in shifting of the temperatures of the start and finish of the bainitic transformation to higher temperature region, but the temperature range proper becomes narrower (Figure 6).

Weld pool inoculation with refractory particles of zirconium oxide, which also have rather high angles of wetting with liquid iron, is accompanied by an increase in the temperature of completion of primary crystallization, which leads to narrowing of the temperature range of $\delta \rightarrow \gamma$ -transformation. Similarly, as with the introduction of magnesium oxides, a shifting of the temperatures of the start and finish of bainitic transformation into the higher temperature region occurs, but the temperature range proper becomes narrower (Figure 6).

Increase of the scope of inoculation with magnesium and zirconium oxide particles promotes an increase in the temperature of the start of primary crystallization, that leads to widening of the temperature range of $\delta \rightarrow \gamma$ -transformation, which is accompanied by a certain increase in the dimensions of prima-

ry crystallites from 100–125 μm in the structure of MgO^{*} weld metal up to 100–210 μm in the structure of MgO^{**} weld and from 50–90 μm in the structure of ZrO₂^{*} weld up to 150–280 μm in the structure of ZrO₂^{**} weld (Figure 6). A shift in the temperatures of the start and finish of the bainitic transformation into the higher temperature region occurs, but the temperature range proper is expanded, resulting in a decrease in the parameter of integrated perimeter of secondary structure grains from 248737 for the structure of MgO^{*} weld to 225604 in the structure of MgO^{**} weld and from 240343 for ZrO₂^{*} weld up to 252681 for ZrO₂^{**} weld (Table 6).

Increase in the scopes of addition of MgO particles to the weld pool is accompanied by an increase in the temperature range of the bainitic transformation from 229 to 238 $^{\circ}\text{C}$, while in the case of an increase in the volume of addition of ZrO₂ particles to the weld pool the range of bainitic transformation remains unchanged (227–224 $^{\circ}\text{C}$), which influences preservation of microhardness of polyhedral ferrite on the level of 188–176 HV0.1 at inoculation with MgO particles and an increase in microhardness of polyhedral ferrite to the level of 194–210 HV0.1 at inoculation with ZrO₂ particles.

Interphase interaction on the solid/liquid interface in the presence of refractory MgO particles helps inhibit the process of dendrite growth to the dimensions of 100–125 μm , whereas in the presence of ZrO₂ particles the dendrites grow to the dimensions of

Table 6. Integrated perimeter of grain boundaries of the secondary structure of the samples (in pixels)

Inoculant volume, %	MgO	ZrO ₂	Al ₂ O ₃	TiO ₂	SiC	TiC + Ti
0.1	248737	240343	236874	262259	253642	251068
0.2	225604	252681	219168	277395	268201	263162

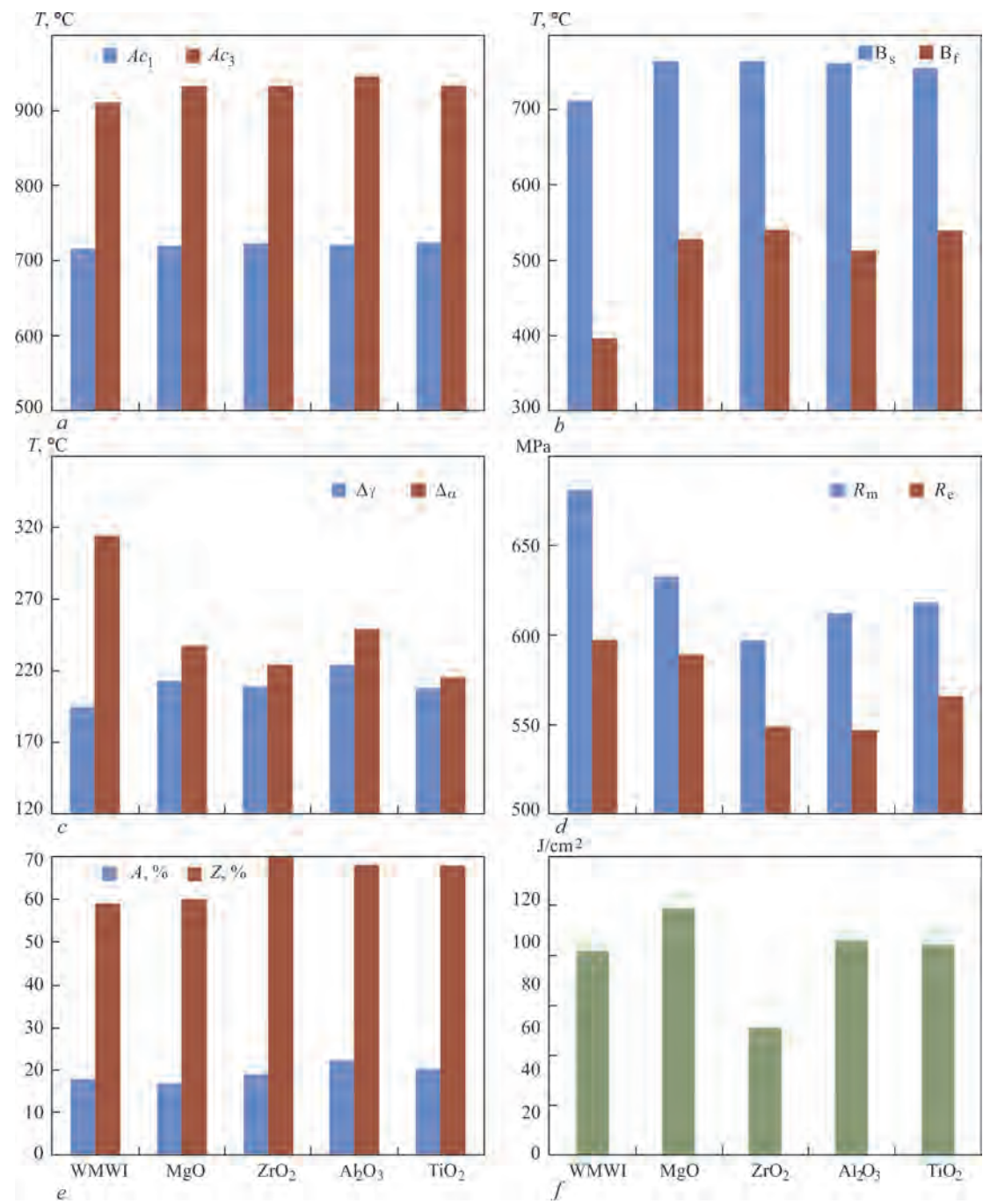


Figure 6. Influence of inoculation of 0.2 % refractory oxides to the weld pool on structural transformations and mechanical properties of the weld metal: *a* — temperatures of the start (Ac_3) and finish (Ac_1) of primary austenite decomposition; *b* — temperatures of the start (B_s) and finish (B_f) of bainitic transformation; *c* — temperature ranges of austenite decomposition ($\Delta\gamma$) and bainitic transformation ($\Delta\alpha$); *d* — ultimate strength (R_m) and yield limit (R_e) of weld metal; *e* — relative elongation (A) and reduction in area (Z) of the weld metal; *f* — impact toughness of weld metal at -20 °C test temperature

150–280 μm , which is attributable to formation of a liquid layer of $\text{MgO}\cdot\text{FeO}$ composition in the points of contact of the dendrite surface with the inoculant and reduction of the contact angle.

Increase in weld pool inoculation with MgO particles promotes both shifting of the bainitic transformation region towards higher temperatures, and increase in the temperature range of the transformation proper to 238 °C. Increase in the content of ZrO_2 particles promotes an increase in the temperatures of the start

and finish of the bainitic transformation, but does not influence the size of its temperature range (Figure 6).

Preservation of the content of acicular ferrite in the secondary structure of the weld metal at the level of 73–84 % with increase of MgO content and 2–5 μm width of the ferrite fringes of the grains, contrary to reduction in acicular ferrite content from 84 to 55 % and increase in the width of the ferrite fringes up to 10 μm with increase of ZrO_2 particle content, is associated with the changes in the kinetics of the bainitic

transformation processes during inoculation with refractory MgO and ZrO₂ particles (Figures 3, 5).

Changes in the content of acicular ferrite in the metal microstructure (Table 3), branching of the grain boundaries and width of their fringes (Table 6), influenced the lowering of both the strength values from 638 to 549 MPa and impact toughness at 40 °C test temperature from 69 to 37 J/cm².

Increase in the temperature of the finish of bainitic transformation and reduction in its temperature range lead to an increase in the content of acicular ferrite in the weld metal structure (Table 3), which may be related to reduction in carbon diffusion from primary austenite grains during $\gamma \rightarrow \delta$ -transformation. Increase in the content of ferrite of acicular morphology in the structure corresponds to an increased level of impact energy of the weld metal, and the relatively low value of this parameter for the case of inoculation with zirconium oxide emphasizes the importance of the processes of reaction layer formation on the interface magnesium and aluminium oxides with liquid iron.

At contact of aluminium and titanium oxides a liquid phase of FeAl₂O₄ and TiO₂·FeO composition forms at the dendrite growth front, respectively, which influences the process of further formation of the weld metal structure. Increase in the content of aluminium and titanium oxides in the weld pool leads to an increase in the temperature of the start and finish of the primary structure formation, as well as the start and finish of the bainitic transformation (Table 4).

In the metal of welds inoculated with aluminium and titanium oxides, the temperature of the start of the bainitic transformation exceeds that of the finish of primary structure formation, which is accompanied by an increased content of polygonal ferrite and width of the ferrite fringes of secondary structure grains in the weld metal secondary structure. Reduction of the temperature range of $\gamma \rightarrow \alpha$ -transformation, as well as increase of the temperature of the bainitic transformation end in the metal of these welds inhibits carbon diffusion during recrystallization, which influences an increase in the content of cementite precipitates in the grain body, and an increase in upper bainite content in the metal structure.

Increase in the content of aluminium oxides in the weld metal is accompanied by rising of the temperature of $\delta \rightarrow \gamma$ and $\gamma \rightarrow \alpha$ -transformations, leading to an increase in the dimensions of primary crystallites, and of the secondary structure grains (Table 3), reduction in the branching of intergranular boundaries (Table 6) and lowering of the values of weld metal toughness at low temperatures (Table 2).

Increase in the content of titanium oxides in the weld metal is accompanied by an increase in the

temperature range of $\delta \rightarrow \gamma$ -transformation, with the temperature range of $\gamma \rightarrow \alpha$ -transformation becoming narrower, which leads to smaller dimensions of primary crystallites and refinement of the ferrite grains (Table 3), and greater branching of the intergranular boundaries (Table 4), but does not result in an increase in the level of metal fracture toughness values (Table 2), which is associated with an increased content of polygonal ferrite and Widmanstaetten ferrite, in keeping with the processes described above.

The data derived as a result of the conducted studies widened the base of scientific knowledge on such phase transformations in steel as restructuring of the crystalline lattice and carbon redistribution between the phases. The features of the influence of these processes on the main types of transformations are shown, namely: ferritic, pearlitic, and bainitic, which successively replace each other at temperature lowering, and on the morphology of the products of decomposition and recrystallization. It is shown that the changes, characteristic for the processes of transformation of the weld structure as a result of pool metal inoculation with the refractory oxides during cooling influence the mechanical properties of the welds.

CONCLUSIONS

Research was performed, which was aimed at widening the base of scientific knowledge on the features of the influence of surface-active modifiers on formation of the weld metal structure. In particular, the influence of the growing dendrite surface wetting with nonmetallic inclusions on the metal structure formation was considered. Generalization and analysis of the derived data allowed us to formulate the following conclusions.

1. Weld pool inoculation with particles of refractory oxides, having rather high angles of wetting with liquid iron (MgO, ZrO₂), is accompanied by an increase in the temperature of the end of primary crystallization, leading to narrowing of the temperature range of $\delta \rightarrow \gamma$ -transformation. During addition of such oxides the temperatures of the start and finish of the bainitic transformation shift towards higher temperature region, but the temperature range proper is narrowed.

2. Interphase interaction on the solid/liquid interface in the presence of refractory MgO particles promotes a deceleration of the process of dendrite growth, which is attributable to formation of a liquid layer of MgO·FeO composition in the points of contact of the dendrite surface with the inoculant and a decrease in the contact angle.

3. Increase in the fraction of inoculated compounds of aluminium, magnesium, titanium and zirconium ox-

ides from 0.1 to 0.2 % influences the temperature of the start and finish of the bainitic transformation. Both the temperature of its start and finish is increased, i.e. bainite formation occurs in the region of higher temperatures, and the temperature range of this region becomes narrower (transformation kinetics is increased).

4. Increase in the temperature of the finish of the bainitic transformation and reduction in its temperature range result in an increase in the acicular ferrite content in the metal structure of welds inoculated with MgO, TiO₂, ZrO₂ particles, which may be associated with reduced carbon diffusion from primary austenite grains during the $\gamma \rightarrow \alpha$ -transformation.

REFERENCES

1. Gubenko, S.I., Parusov, V.V., Derevyanchenko, I.V. (2005) *Nonmetallic inclusions in steel*. Dnipro, ART-PRESS [in Russian].
2. Goldstein, Ya.E., Mizin, V.G. (1956) *Modification and microalloying of cast iron and steel*. Moscow, Metallurgiya [in Russian].
3. Shpis, H.-I. (1971) *Behavior of nonmetallic inclusions in steel during crystallization and deformation*. Moscow, Metallurgiya [in Russian].
4. Popovich, V., Kondir, A., Pleshakov, E. et al. (2009) *Technology of structural materials and materials science. Practical work*. Lviv, Svit [in Ukrainian].
5. Bokshetjn, B.S., Kopetsky, I.V., Shvindlerman, L.S. (1986) *Thermodynamics and kinetics of grain boundaries in metals*. Moscow, Metallurgiya [in Russian].
6. Gulyaev, A.P. (1977) *Metals science*. Moscow, Metallurgiya [in Russian].
7. Rohrer, G.S. (2011) Grain boundary energy anisotropy: A review. *J. Mater. Sci.*, **46**, 5881–5895. DOI: <https://doi.org/10.1007/s10853-011-5677-3>
8. Rohrer, G.S., Anthony, J.G., Rollett, E.D. (2008) A model for the origin of anisotropic grain boundary character distributions in polycrystalline materials. *Applications of Texture Analysis*, **17**, 10. DOI: <https://doi.org/10.1002/9780470444214.ch36>
9. Panasyuk, A.D., Fomenko, V.S., Glebova, H.G. (1986) *Stability of nonmetallic materials in melts*. Kyiv, Naukova Dumka [in Russian].
10. ISO 14171:2008(E): *Welding consumables — Wire electrodes and wire-flux combinations for submerged arc welding of non alloy and fine grain steels — Classification*.
11. ISO 17639:2003: *Destructive tests on welds in metallic materials — Macroscopic and microscopic examination of welds*.
12. IIW Doc. No. IX-1533-88/IXJ-123-87 Revision 2 / June 1988 *Guide to the light microscope examination of ferritic steel weld metals*.

ORCID

V.V. Holovko: 0000-0002-2117-0864,

V.A. Kostin: 0000-0002-2677-4667,

V.V. Zhukov: 0000-0002-3358-8491

CONFLICT OF INTEREST

The Authors declare no conflict of interest

CORRESPONDING AUTHOR

V.V. Holovko

E.O. Paton Electric Welding Institute of the NASU
11 Kazymyr Malevych Str., 03150, Kyiv, Ukraine.

E-mail: v_golovko@ukr.net

SUGGESTED CITATION

V.V. Holovko, V.A. Kostin, V.V. Zhukov (2025) Dispersed oxides influence on the kinetics of the weld metal structural transformations. *The Paton Welding J.*, **6**, 9–18.

DOI: <https://doi.org/10.37434/tpwj2025.06.02>

JOURNAL HOME PAGE

<https://patonpublishinghouse.com/eng/journals/tpwj>

Received: 31.10.2024

Received in revised form: 19.03.2025

Accepted: 25.06.2025



IEEE STEE-2026

2026 IEEE 8TH INTERNATIONAL CONFERENCE

ON SMART TECHNOLOGIES IN POWER ENGINEERING AND ELECTRONICS

IEEE Kyiv Polytechnic Week

Igor Sikorsky Kyiv Polytechnic Institute

April 27-30, 2026, Kyiv, Ukraine

<https://stee.ieee.org.ua/>

E-mail: stee@ieee.org.ua

IMPORTANT DATES

Paper Submission — December 1, 2025

Review — February 15, 2016

Final Paper Submission — March 1, 2026

Acceptance Notification — March 15, 2026

Registration — April 1, 2026

Conference — April 27-30, 2026

INFLUENCE OF ELECTRON BEAM WELDING TECHNOLOGY ON THE WIDTH OF THE SOFTENING ZONE OF ALUMINIUM 2219 ALLOY

**V.V. Skryabinskyi, V.M. Nesterenkov, M.O. Rusnyk, V.I. Zagornikov,
O.I. Goncharenko, I.M. Klochkov**

E.O. Paton Electric Welding Institute of the NASU
11 Kazymyr Malevych Str., 03150, Kyiv, Ukraine

ABSTRACT

During electron beam welding (EBW) of 2219 alloy, the strength characteristics of joints can decrease by up to 50 % in relation to the base metal. In order to ensure the uniform strength of the structure, the locations of the welds are chosen in thickened areas. At the same time, the width of the thickened area should be greater than the width of the softening zone of the welded joint. This zone includes the cast zone and the heat-affected zone (HAZ), in which the strength of the base metal decreased. The influence of welding speed and the use of process pads on the width of the cast zone and the HAZ, i.e. on the width of the softening zone during EBW of 2219 alloy plates were studied. It was found that an increase in the welding speed from 10 to 20 mm/s reduced the width of the softening zone approximately by a half. The use of the process pad allows reducing the width of the softening zone by approximately 20 %. In this case, the weld underfill is formed in the body of the pad and after its removal the welded butt does not require further mechanical treatment. It was established by calculation and experimental methods that the process pad cuts off the peripheral part of the electron beam, which is about 5 % of its full power. In practice, the influence of this peripheral part leads to undesirable expansion of the weld on the side of the beam entrance and to additional heating of the base metal and, as a result, to an increase in the size of the softening zone.

KEYWORDS: electron beam welding, aluminium alloy, heat affected zone, softening zone, process pad

INTRODUCTION

The high-strength aluminium 2219 alloy of the Al–6Cu alloying system is a heat-treatable alloy. The high mechanical properties of such alloys are achieved as a result of heat treatment, at which secondary strengthening phases are precipitated. During welding of such alloys, these phases dissolve in the heat-affected zone (HAZ), which causes a decrease in the strength characteristics of the metal. The beginning of the dissolution process is featured not only by the maximum heating temperature, but also by the duration of staying in the corresponding temperature range [1].

The electron beam welding (EBW) process is characterized by a very short thermal cycle period with high cooling rates and a small volume of molten metal. This leads to a significant reduction in the size of the HAZ [2, 3]. Despite this, the strength of welded joints remains quite low. For example, even at short-term heating typical for EBW, the strength factor of Al–6Cu alloy joints is 70–75 % [4] and sometimes less than 50 % [5]. In order to ensure a uniform structural strength, weld locations are chosen in thickened areas. Moreover, the width of the thickened area should be greater than the width of the softening zone of the welded joint. On the other hand, an excessive increase in the width of such areas leads to an undesirable increase in the overall

weight of the structure. The softening zone of the joint includes the cast zone and the HAZ, where the strength of the base metal decreased. In order to reduce the weight of structures, it is necessary to choose the EBW conditions, which ensure the production of welds with a minimum width of the cast zone and HAZ. Electron beam welding allows producing such joints. High energy concentration allows welding metals at high speed with a small weld pool volume.

The EBW of aluminium alloys has its own peculiarities. In many cases, the penetration has a wedge shape [5–8]. This is predetermined by the fact that the distribution of the electron beam power density along its cross-section is close to the normal distribution law [9]. The central part of the beam with the highest energy concentration melts the metal and ensures its welding. The peripheral parts of the beam hitting the edges of the metal being welded melt them, thereby increasing the width of the weld on the side of the beam entrance. In addition, the edges of this peripheral part of the beam, which no longer have enough power to melt the metal, directly heat the edges to be welded, increasing the HAZ width.

Typical cross-sections of joints of aluminium Al–6Cu system alloys welded by electron beam are shown in Figure 1. In all cases, the welds are wider at the beam entrance than at the root part. Also, a slight

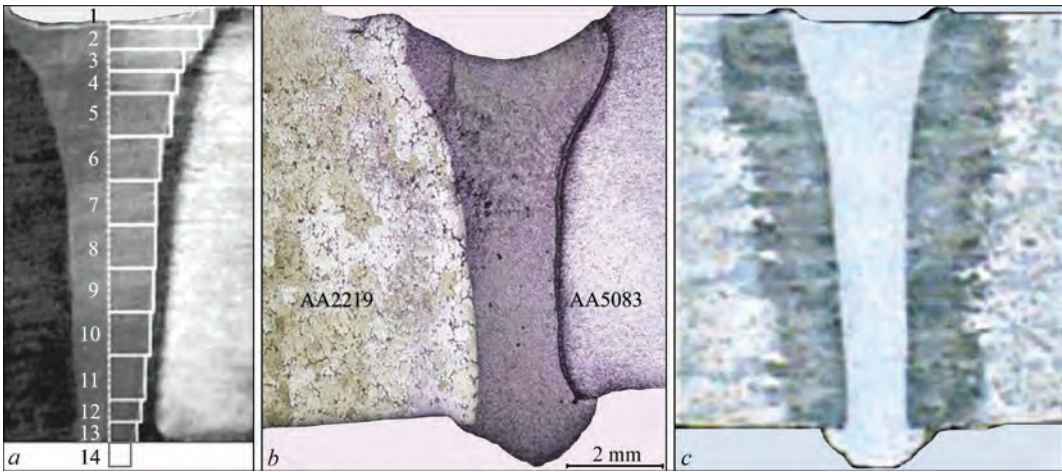


Figure 1. Typical cross-sections of welds at EBW of Al-6Cu alloy: *a* — [6]; *b* — [7]; *c* — [8]

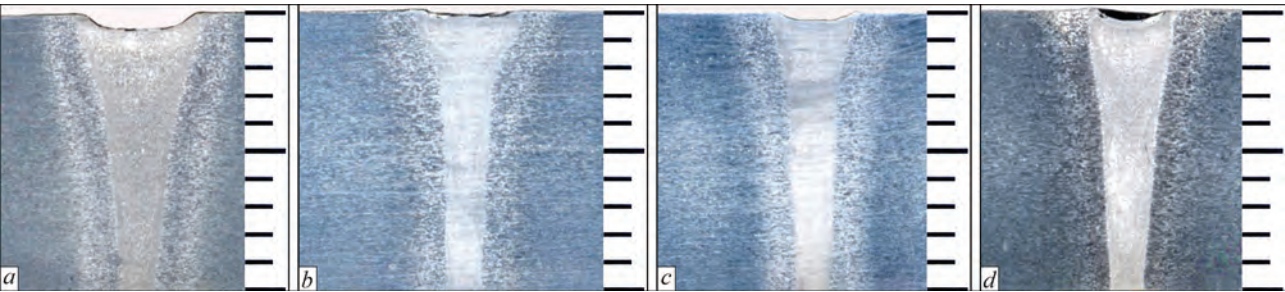


Figure 2. Cross-sections of welds at EBW of 2219 alloy at welding speed: *a* — 10; *b* — 15; *c* — 20; *d* — 25 mm/s

underfill of the weld metal is seen on the beam entrance side.

THE AIM

of this work is to determine the technology for EBW of 2219 alloy plates, which ensures the production of joints with a minimum width of the softening zone.

DESCRIPTION OF THE MAIN MATERIAL

Welding was carried out in an electron beam welding installation UL-209M with an ELA 60/60 power source. The hardness of the weld metal and HAZ were measured by the Vickers method, using the M-400 hardness tester by LECO. The load was 1N (100 g), the time of load application was 10 s. The plates of aluminium 2219 T8 alloy with a thickness of 10 mm were welded. The parameters of the welding conditions (Table 1) were selected in such a way as to provide complete penetration of the butt in one pass with the formation of reinforcement and reverse weld bead.

Table 1. EBW conditions for 2219 alloy plates

Metal thickness, mm	10	10	10	10	12.2*
Accelerating voltage, kV	60	60	60	60	60
Welding speed, mm/s	10	15	20	25	20
Beam current, mA	55	70	85	95	95
* – 10 mm + 2.2 mm thick pad.					

In all experiments, a circular beam scanning trajectory was used at an amplitude of 1 mm and a scan frequency of 580 Hz with focusing on the surface of the plates to be welded. I.e., the relative distribution of the electron beam power density was maintained constant. Cross-sections of welds at EBW of 2219 alloy at welding speeds of 10, 15, 20 and 25 mm/s are shown in Figure 2.

The widest welds (see Table 2) were produced by welding at a speed of 10 mm/s. The cast zone is wedge-shaped, its width is 5.5 mm on the beam entrance side and 1.6 mm on the beam exit side. When the speed was increased to 15 mm/s, the width of the cast zone decreased to 3.6 and 1.4 mm, respectively. The further increase in the welding speed did not significantly affect the width of the cast zone.

Table 2. Width of the weld cast zone depending on the welding speed

Welding speed, mm/s	10	15	20	25*	20 (welding with the pad)
Width of the cast zone on the beam entrance side, mm	5.5	3.6	3.6	3.6	1.6
Width of the cast zone on the beam exit side, mm	1.6	1.4	1.4	1.3	1.4
*Weld with defects.					

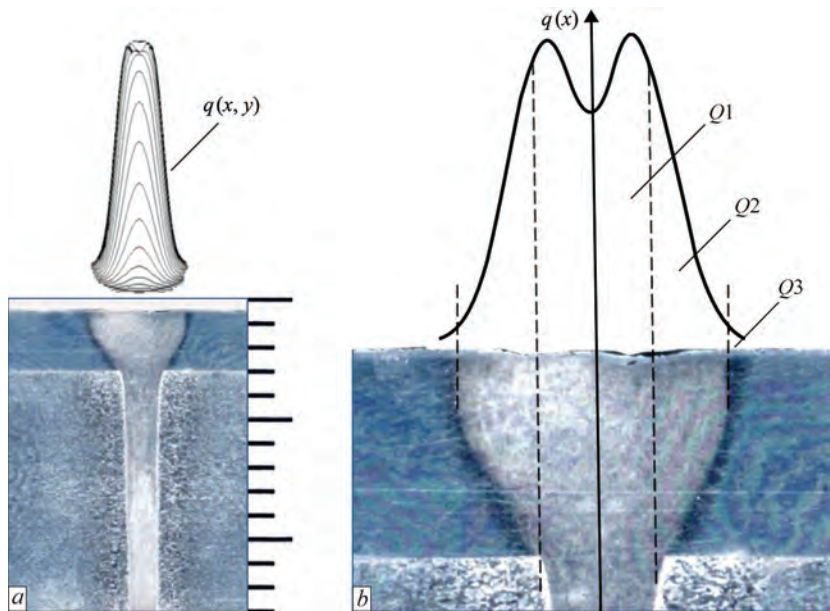


Figure 3. Distribution of beam power density (*a* — $q(x, y)$ and *b* — $q(x)$) and cross-section of 2219 alloy weld produced using a pad made of the same alloy

The expansion of the cast zone from the beam entrance is caused by the presence of a peripheral part of the beam with a relatively low power density. In order to exclude the influence of the peripheral part of the beam on the penetration shape, a welding technique with the pad of the same material was used. Such pads during welding with complete penetration not only shield the peripheral parts of the beam, but also serve as a filler material. The underfill in the weld is formed in the body of the pad. After welding, the pad is removed by mechanical treatment.

It was noted that at speeds of 10, 15 and 20 mm/s, the welding process is carried out with stable joint formation both from the face and root parts of the weld. When the welding speed is increased to 25 mm/s, the stability of the weld formation is violated. Defects such as poor penetration and slight metal leakage periodically appear in the root part of the weld. Therefore, welding with the process pad was carried out at the maximum speed that ensures a stable process, i.e. at 20 mm/s.

In Figure 3, the cross-section of the weld produced with the pad was schematically combined with the volumetric diagram of the beam power density distribution (Figure 3, *a*) and the cross-section of this diagram (Figure 3, *b*). It is seen from the Figure that the cast zone is narrow and has an almost rectangular shape. The width of the cast weld zone under the pad is 1.6 mm and 1.4 mm on the beam exit side, with a maximum pad partial melting width of 5 mm. The central part of the electron beam with the highest energy concentration and power $Q1$ ensures complete penetration of the metal to be welded and the process pad. The side peripheral parts of the beam with a low

energy concentration are shielded by the process pad. At the same time, they partially melt (power $Q2$) and heat (power $Q3$) the pad.

It is interesting to determine how much of the electron beam power is shielded by the process pad. It can be calculated or measured experimentally. The previously developed algorithm for calculating the distribution of electron beam power density [10] allows calculating the ratio of beam powers in any selected treatment areas. For the calculations, a software for designing electron beam scans was used [11]. Figure 4 shows the distribution of the power density of an electron beam with an effective diameter of 0.5 mm for a scan in the form of a circle with a diameter of

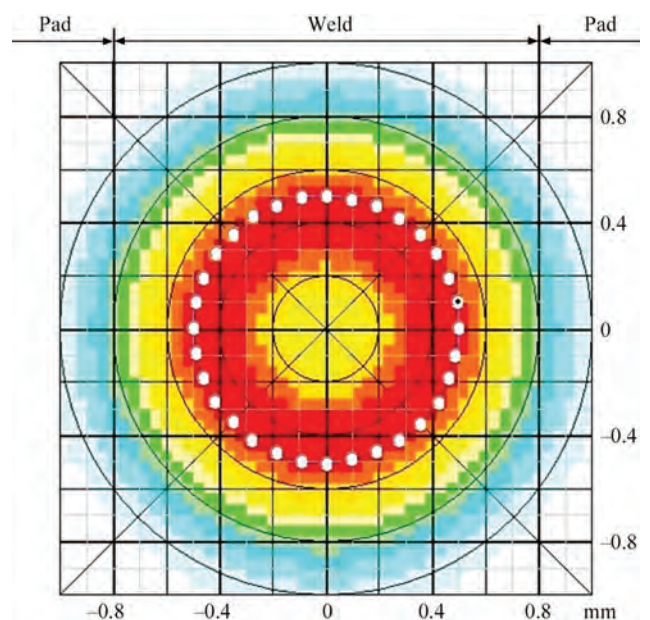


Figure 4. Color image of the beam power density distribution $q(x, y)$ displayed on the computer screen

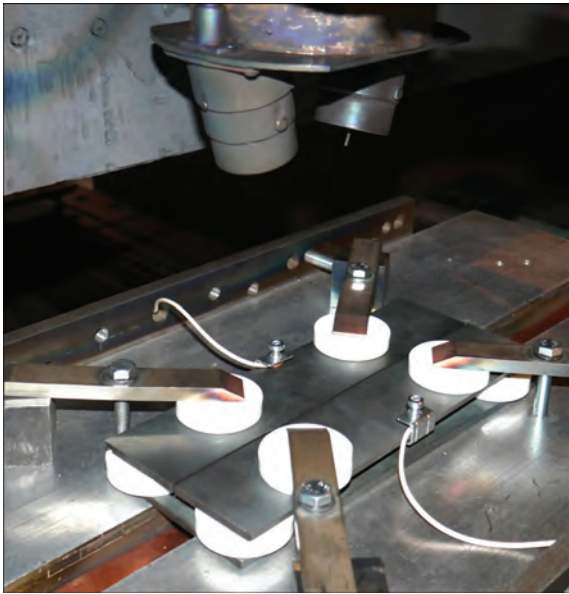


Figure 5. Experimental measurement of the beam power shielded by the process pad

1 mm. The colours represent the beam power intensity from minimum (blue) to maximum (red).

A part of the electron beam power that falls on the weld area with complete penetration ($Q1, \%$) can be calculated by the formula:

$$Q1(\%) = \frac{100 \iint_{WMe} q(x, y) dx dy}{\iint_{Me} q(x, y) dx dy},$$

where $q(x, y)$ is the distribution of beam power density; WMe is the area of beam effect that falls on the weld metal; Me is the entire area of electron beam treatment. Similarly, it is possible to calculate a part of the beam power that is consumed for partial melting ($Q2, \%$) and heating ($Q3, \%$) of the pad metal on both sides of the weld.

Calculations have shown that in our case, about 95 % of the electron beam power is directed at the weld, and about 2.5 % of the beam power on each side is directed to heating and melting the parts of the pad adjacent to the weld, respectively. The experimental measuring of the electron beam power directed at a certain area to be treated is possible by placing a refractory metal target in this area and measuring the amount of current passing through the target. The beam power shielded by the pad was determined as follows. Molybdenum plates with a thickness of 6 mm were fixed in the assembly and welding device with a gap of 1.6 mm between them. The width of the gap was equal to the width of the weld under the process pad. The plates were placed on the ceramic insulators and fixed with clamps through the ceramic insulators, as shown in Figure 5.

These insulators electrically isolated the plates from the welding chamber, i.e. from “ground”. The electric wires connected to the molybdenum plates were removed from the vacuum chamber and connected to ‘ground’ through voltage dividers. Electric currents passing through the plates were measured by voltmeters connected to voltage dividers. A basic secondary electronic video surveillance system of the RASTR6 type was used to direct the beam to the centre of the gap between the plates. After that, the welding process was simulated at the conditions used for welding the 2219 alloy plates with the pad (i.e., at a beam current of 95 mA, see Table 1). When the beam was precisely aimed at the centre of the gap, the readings of voltmeters during the experiment coincided. During the measurement, the currents of the plates fluctuated within 2.5–3.5 mA. Thus, approximately 5 to 7 % of the total beam power fell on both plates. The total width of the softening zone of the welded

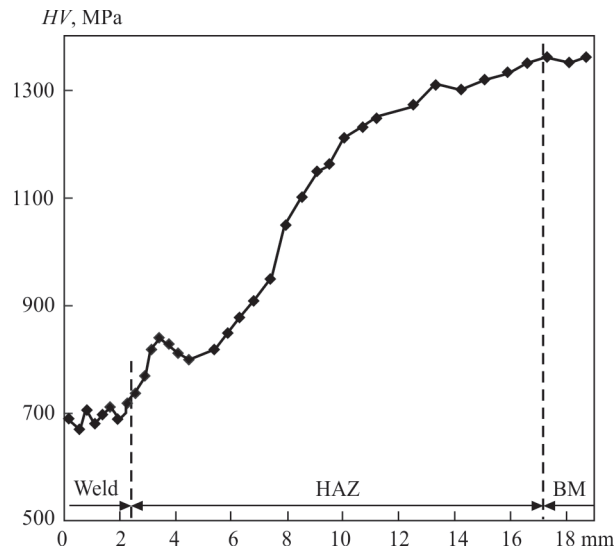


Figure 6. Distribution of hardness in the cross-section of joints in 2219 alloy plates welded at a speed of 10 mm/s

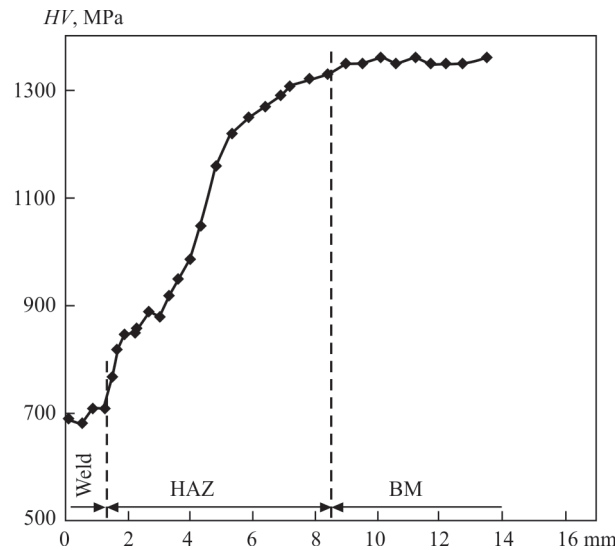


Figure 7. Distribution of hardness in the cross-section of joints in 2219 alloy plates welded at a speed of 20 mm/s

Table 3. Width of the HAZ and softening zone depending on the welding speed and during welding with the process pad

Welding speed, mm/s	10	15	20	25*	20 (welding with the pad)
Maximum width of the cast zone, mm	5.5	3.6	3.6	3.6	1.6
Width of HAZ from the fusion line to the base metal, mm	15	10	7	6	6
Width of the softening zone, mm	35.5	23.6	17.6	15.6	13.6

*Weld with forming defects.

joint is equal to the width of the cast zone plus the width of the HAZ on both sides of it. The width of the HAZ was determined by measuring the hardness of the cross-sections of the welded joints at distances of 1.5 mm from the plate surface on the beam entrance side. The measurement step was 0.3–0.5 mm. The measurements started from the centre of the weld and ended in 3–5 mm after reaching the base metal. The distribution of hardness in the cross-sections of the joints of 2219 alloy plates welded at speeds of 10 and 20 mm/s is shown in Figures 6 and 7.

The hardness of the weld metal is 670–710 MPa, while the hardness of the base metal is 1350–1360 MPa. When the welding speed was increased from 10 to 20 mm/s, the HAZ width decreased from 15 to 7 mm. It is seen that the hardness of the metal at a distance of 1 mm from the fusion line is by 30–40 MPa higher than the hardness measured at a distance of 2–3 mm. This is predetermined by the partial hardening of the metal in the immediate vicinity of the weld after it was heated to the quenching temperature and then rapidly cooled. The cross-sectional hardness distribution of the joints of 2219 alloy plates welded with the process pad is shown in Figure 8.

Table 3 shows the dependence of the HAZ width and softening zone on the welding speed.

Table shows that an increase in the welding speed from 10 to 20 mm/s reduces the width of the softening zone by almost half (from 35.5 to 17.6 mm). The further increase in the welding speed is inappropriate because it will cause violation of the joint formation stability and appearance of defects.

The use of the process pad during EBW of 10 mm thick aluminium 2219 alloy plates allows reducing the width of the softening zone from 17.6 to 13.6 mm (i.e. by about 20 %) on the beam entrance side and producing a narrow weld with practically parallel side walls.

CONCLUSIONS

It has been found that during EBW of 2219 aluminium alloy plates with a thickness of 10 mm, an increase in

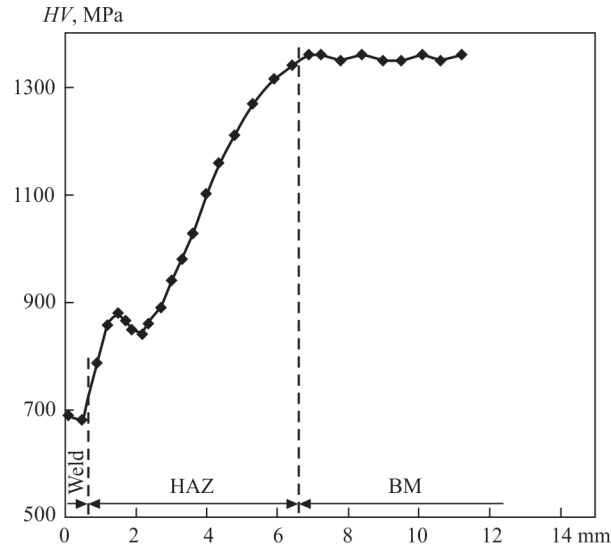


Figure 8. Distribution of hardness in the cross-section of joints in 2219 alloy plates welded with the technological pad at a speed of 20 mm/s

the welding speed from 10 to 20 mm/s reduces the width of the softening zone approximately by a half.

The use of the process pad when welding at a speed of 20 mm/s allows for an additional reduction in the width of the softening zone by approximately 20 % and produces a narrow weld with almost parallel side walls. In this case, the weld underfill is formed in the body of the pad; after its removal, the welded butt does not require further mechanical treatment.

An algorithm for calculating the ratio of beam powers in selected areas of the treated surface was proposed. It has been found by calculations and experiments that the technological pad cuts off the peripheral part of the electron beam, which is about 5–7 % of its total power. In practice, the influence of this peripheral part leads to undesirable expansion of the weld on the beam entrance side and to additional heating of the base metal and, as a result, to an increase in the sizes of the softening zone.

REFERENCES

1. Lozovskaya A.V., Chajka A.A., Bondarev A.A., Poklyatsky A.G., Bondarev Andr.A. (2001) Softening of high-strength aluminium alloys in different fusion welding processes. *The Paton Welding J.*, **3**, 13–17. <https://patonpublishinghouse.com/tpwj/pdf/2001/tpwj200103all.pdf>

2. Fatih Hayat (2022) Electron beam welding of 7075 aluminium alloy: Microstructure and fracture properties. *Engineering Sci. and Technol. an Inter. J.*, **34**, 101093. DOI: <https://doi.org/10.1016/j.jestch.2022.101093>

3. Meng, Qing-guo, Fang, Hong-yuan, Xu, Wen-li, Ji, Shu-de (2006) Microstructure and mechanical properties of 2219 Al-alloy heat-affected zone with twin wire welding. *Transact. of the China Welding Institution*, **3**, 9–12. DOI: <https://hjb.hwi.com.cn/hjxb/en/article/id/20060303>

4. Nazarenko, O.K., Kajdalov, A.A., Kovbasenko, S.N. et al. (1987) *Electron beam welding*. Ed. by B.E. Paton. Kyiv, Naukova Dumka.

5. Ghulam Hussain, Tauheed Shehbaz, Mohammed Alkahtani, Usman Abdul Khaliq, Hongyu Wei (2024) Nanomechanical, mechanical and microstructural characterization of electron beam welded Al2219-T6 tempered aerospace grade alloy: A comprehensive study. *Heliyon*, 10(1), e23835. DOI: <https://doi.org/10.1016/j.heliyon.2023.e23835>
6. Skalsky, V.R., Botvina, L.R., Lyasota, I.N. (2012) Peculiarities of structure and mechanical heterogeneity in EB-welded joints of 1201-T alloy. *The Paton Welding J.*, 7, 15–18. <https://patonpublishinghouse.com/tpwj/pdf/2012/pdfarticles/07/5.pdf>
7. Mastanaiah P., Abhay Sharma, Madhusudhan Reddy G. (2018) Process parameters-weld bead geometry interactions and their influence on mechanical properties: A case of dissimilar aluminium alloy electron beam welds. *Defence Technology*, 14, 137–150. DOI: <https://doi.org/10.1016/j.dt.2018.01.003>
8. Rusynyk, M.O., Nesterenkov, V.M., Sahul, M., Klochkov, I.M. (2023) Influence of electron beam focusing current on geometry and microstructure of welded joints of aluminium 2219 alloy. *The Paton Welding J.*, 7, 31–36. DOI: <https://doi.org/10.37434/tpwj2023.07.04>
9. Rykalin, N.N., Zuyev, I.V., Uglov, A.A. (1978) Basis of electron-beam material processing. Moscow, Mashinostroenie [in Russian].
10. Skryabinskyi, V.V. (1994) *Development of technology of electron beam welding of high-strength aluminium alloys 1570 and 1460 with control of density distribution of beam power*: Syn. of Thesis for Cand. of Techn. Sci. Degree. Kyiv, PWI [in Ukrainian].
11. Skryabinskyi, V.V., Nesterenkov V.M., Rusynyk, M.O. (2020) Electron beam welding with programming of beam power density distribution. *The Paton Welding J.*, 1, 49–53. DOI: <https://doi.org/10.37434/tpwj2020.01.07>

ORCID

V.V. Skryabinskyi: 0000-0003-4470-3421,
V.M. Nesterenkov: 0000-0002-7973-1986,
M.O. Rusynyk: 0000-0002-7591-7169,
V.I. Zagornikov: 0000-0003-0456-173X,
O.I. Goncharenko: 0009-0007-8492-7119,
I.M. Klochkov: 0000-0001-6490-8905

CONFLICT OF INTEREST

The Authors declare no conflict of interest

CORRESPONDING AUTHOR

V.V. Skryabinskyi
E.O. Paton Electric Welding Institute of the NASU
11 Kazymyr Malevych Str., 03150, Kyiv, Ukraine.
E-mail: skryabinski.vv.555@gmail.com

SUGGESTED CITATION

V.V. Skryabinskyi, V.M. Nesterenkov, M.O. Rusynyk, V.I. Zagornikov, O.I. Goncharenko, I.M. Klochkov (2025) Influence of electron beam welding technology on the width of the softening zone of aluminium 2219 alloy. *The Paton Welding J.*, 6, 19–24.
DOI: <https://doi.org/10.37434/tpwj2025.06.03>


JOURNAL HOME PAGE

<https://patonpublishinghouse.com/eng/journals/tpwj>

Received: 04.03.2025

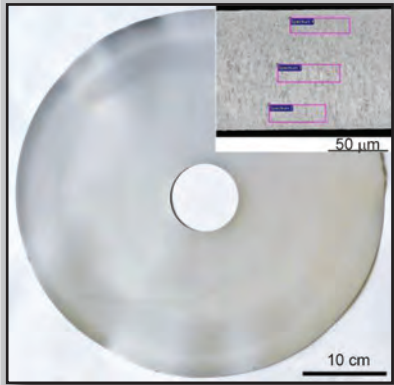
Received in revised form: 06.05.2025

Accepted: 25.06.2025

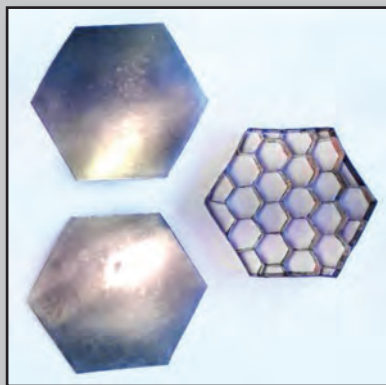


Developed at PWI

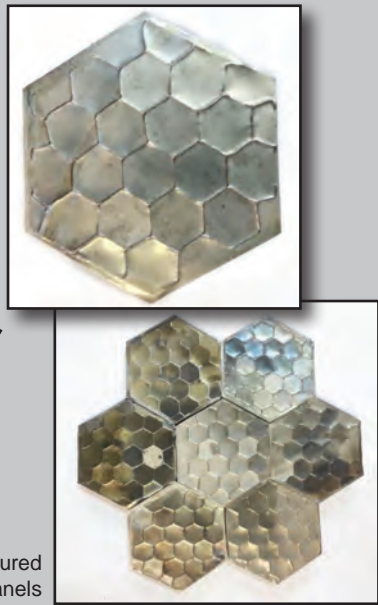
Fabricating lightweight thermal protection honeycomb sandwich panels based on thin-sheet heat-resistant alloys produced by vacuum deposition



Appearance and microstructure (inset) of the cross-section CoCrFeNiSi_{0.2} high-entropy alloys foil



General view of the the manufactured elements of the three-layer panel (lower and upper cover sheets, honeycomb core)



General view of the manufactured three-layer honeycomb panels

For more information, please follow the link <https://doi.org/10.37434/tpwj2023.08.03>

DETONATION SPRAYING OF COATINGS CONTAINING Cr_2AlC MAX PHASE

N.V. Vigilianska¹, C. Senderowski², T.V. Tsymbalista¹, K.V. Iantsevitch¹,
A.I. Kildiy¹, O.Yo. Gudymenko³

¹E.O. Paton Electric Welding Institute of the NASU
11 Kazymyr Malevych Str., 03150, Kyiv, Ukraine

²Warsaw University of Technology, Institute of Mechanics and Printing
Narbutta 85, 02-524 Warsaw, Poland

³V.E. Lashkaryov Institute of Semiconductor Physics of the NASU
41 Nauky Prosp., 03028, Kyiv, Ukraine

ABSTRACT

The paper investigates the process of forming coatings containing Cr_2AlC MAX phase by detonation spraying using powders produced by the mechanochemical synthesis. The powder mixtures of the Cr–Al–C and Cr_3C_2 –Al systems were used as starting components. It has been found that no new phases are formed in the Cr–Al–C system as a result of mechanochemical synthesis within 1.5–5 h, while the synthesis of Cr_2AlC MAX phase occurs during the detonation spraying of the MChS powder of this mixture. In the Cr_3C_2 –Al system, the formation of Cr_2AlC MAX phase is observed already at the processing stage after 1.5 h. Due to the interaction reaction of the components in the process of detonation spraying, the content of MAX phase grows in the coating relative to the MChS powder. Both types of coatings contain phases of chromium carbides and oxide components of chromium and aluminium. The produced coatings are characterized by high microhardness (about 5000 MPa), dense lamellar structure, and corrosion resistance in a 3 % NaCl solution.

KEYWORDS: MAX phase, detonation spraying, coating, microstructure, corrosion resistance

INTRODUCTION

In recent years, materials based on MAX phases have attracted increased interest for industrial use due to their unique combination of both metal and ceramic properties, which they owe to their typical nanolaminate structure [1, 2]. Among the currently known MAX phases, Cr_2AlC phase is of considerable interest due to its complex of physical and chemical properties, namely: low density, excellent mechanical properties, high rigidity, ease of processing, resistance to damage, corrosion resistance in many salt and acid solutions, electrical and thermal conductive properties [3–6]. Among the methods for producing Cr_2AlC MAX phase, the most common are sintering methods, including spark plasma sintering, hot pressing, methods of self-propagating high-temperature synthesis (SHS), and mechanochemical synthesis [7–11]. Powders of both simple elements as well as compounds of carbides, oxides, and intermetallics in various ratios are used as starting components. The produced materials have high strength, heat resistance and corrosion resistance.

Another method of using materials based on MAX phases is their depositing on the surface of parts in the form of coatings. Most of the available studies are devoted to the formation of coatings based on Cr_2AlC MAX phase in the form of thin films produced by magnetron sputtering of individual elements or segmented composite targets [12, 13]. Despite the high

purity and density of magnetron coatings, they cannot be used in extreme conditions under high loads due to their small thickness, which is several microns.

To produce coatings based on MAX phases with a thickness of several hundred micrometers, thermal spraying methods such as plasma-arc, high-velocity oxygen fuel, and cold gas-dynamic spraying are used [14]. The raw materials used for spraying are powders with a synthesized Cr_2AlC MAX phase produced by sintering [15] and powders of mechanical mixtures of the starting components, such as Cr + Al + graphite [16], Cr_3C_2 + Al + Cr [17]. When using powders containing MAX phase for spraying, due to the oxidation of powder particles and decomposition reactions associated with incongruent melting of MAX phases, the content of Cr_2AlC MAX phase in the coatings is significantly reduced relative to the starting powder, which is one of the main problems when spraying this type of coatings. In the case of spraying powders of mechanical mixtures, the synthesis of MAX phase occurs during the spraying process and the formation of the coating layer at the interaction of starting components. The content of MAX phase in such coatings can be further increased by the following heat treatment [16].

THE AIM

of this work is to study the formation of coatings containing Cr_2AlC MAX phase under the conditions of the detonation spraying method using powders produced by the mechanochemical synthesis.

Table 1. Characteristics of starting powders of mechanical mixtures

Powder	Grade	Particle size, μm	Impurity content, wt. %
Cr	PKh1M	<20	0.009 N; 0.07 C; 0.20 Fe; 0.10 Ni; 0.10 Si; 0.10 Ca; 0.30 O; P i 0.032 O
Al	PA-4	40–50	<0.4 Si, <0.35 Fe, <0.02 Cu
Graphite	GL-1	<40	Ash content <13 %
Cr ₃ C ₂	PKKh-1S	<40	–

MATERIALS AND RESEARCH PROCEDURES

Powders produced by the method of mechanochemical synthesis (MChS) of powder mixtures of 73Cr–19Al–8C and 91Cr₃C₂ + 9Al (wt. %) compositions were used as materials for spraying coatings by the detonation method. The characteristics of the starting powders used to produce the mechanical mixtures for the MChS process are given in Table 1.

The ratio of the components of the Cr–Al–C powder mixture was calculated to produce Cr₂AlC MAX phase according to the reaction 2Cr + Al + C = Cr₂AlC; the components of the Cr₃C₂–Al mixture were calculated on the basis of a thermodynamic assessment of the probability of reactions in the system with the formation of Cr₂AlC MAX phase and previous studies of the formation of Cr₂AlC MAX phase under plasma-arc spraying of Cr₃C₂–Al system powders [18].

The MChS process of powder mixtures was carried out in a high-energy planetary mill “Activator 2SL” at a drum rotation speed of 1000/1500 rpm, the processing time was 1.5 and 5 h.

For coating spraying, a detonation spraying unit “Pe-run-S” was used. A mixture of oxygen and propane-butane with the addition of air was used as a detonation mixture, the flow rate and ratio of oxygen to propane-butane was 3:1, the amount of powder per shot was ≈ 100 mg, and the number of shots was 100, the cycle frequency was 6.6 s^{–1}. The technological parameters of detonation spraying, such as propane-butane fuel gas flow rate (*Q*_{C₃H₈}), oxygen flow rate (*Q*_{O₂}), diluent gas flow rate (air) (*Q*_{air}), transport gas flow rate (air) (*Q*_{tr}), and spraying distance (*L*), are given in Table 2. The technological parameters of detonation spraying were selected based on the calculation of obtaining a coating thickness of 4–6 μm for 1 cycle and minimizing the oxidation of the powder material during the spraying process.

A Neophot-32 optical microscope with a digital photography device was used to study the particle mi-

crostructure of MChS powders and sprayed coatings. The phase composition of the powder and coating particles was studied using a PANalytical X’Pert PRO diffractometer with CuK_α radiation (λ = 0.15406 nm). The voltage at the tube anode was 45 kV and the current was 40 mA. Diffraction patterns were taken in a step of 0.025° with a point accumulation time of 1 s. The diffractometric measurements data were processed using High Score Plus software. The microhardness *HV* of the coatings was measured using a PMT-3 microhardness tester at an indenter load of 50 g.

The corrosion resistance of the coatings was studied using the potentiostatic method. The coatings with a thickness of 500 μm were deposited on the specimens of AISI 1017 steel with dimensions of 50×50×3 mm. Electrochemical studies were carried out in a P-5827M potentiostat with a scan rate of 2 mV/s at a temperature of 18–20 °C. The specimens under study were used as working electrodes, a chlorosilver electrode (Ag/AgCl) was used as a comparison electrode, and platinum was used as an auxiliary electrode. The study was carried out in a 3% NaCl solution. The current and corrosion potential were determined graphically from polarization curves.

RESEARCH RESULTS AND DISCUSSION

The analysis of the microstructure of the powders of Cr–Al–C and Cr₃C₂–Al systems (Figure 1) indicates the formation of conglomerate-type particles of irregular shape in the MChS process due to the repeated processes of refinement and “cold welding”: both after 1.5 h and after 5 h of processing. The size of the powders of MChS products after 1.5 h of processing is *d*₁₀ = 9 μm, *d*₅₀ = 21 μm, *d*₉₀ = 43 μm for Cr–Al–C system and *d*₁₀ = 8 μm, *d*₅₀ = 17 μm, *d*₉₀ = 45 μm for Cr₃C₂–Al system. When the processing time is increased to 5 hours, the size of the MChS products does not change significantly and is *d*₁₀ = 10 μm, *d*₅₀ = 21 μm, *d*₉₀ = 41 μm for Cr–Al–C system and *d*₁₀ = 8 μm, *d*₅₀ = 16 μm, *d*₉₀ = 40 μm for Cr₃C₂–Al system.

It was found by X-ray diffraction analysis (XRD) that during the MChS process for 1.5 and 5 h of Cr–Al–C system powder, no new phases were synthesized, and only the peaks of the chromium and aluminum phases were present on the XRD patterns of the produced powders (Figure 2, *a*, *b*). The graphite phase

Table 2. Technological parameters of detonation spraying of coatings containing Cr₂AlC MAX phase

Gas flow rate, m ³ /h				<i>L</i> , mm
<i>Q</i> _{C₃H₈}	<i>Q</i> _{O₂}	<i>Q</i> _{air}	<i>Q</i> _{tr}	
0.5	1.55	0.4	0.5	110

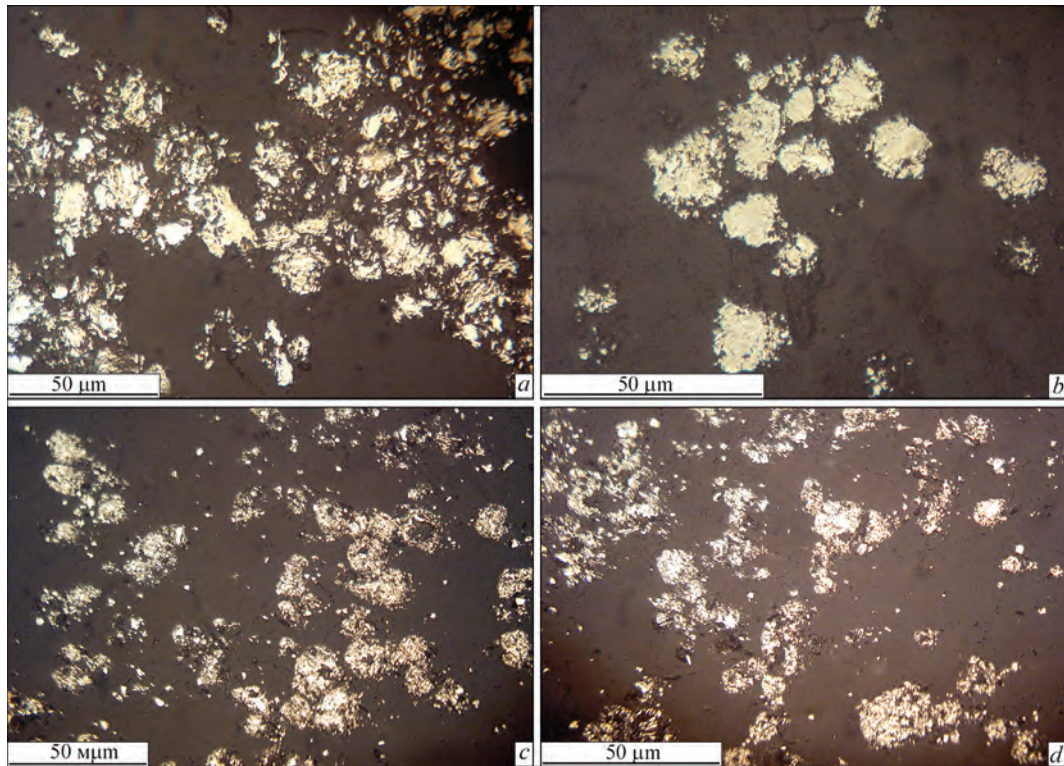


Figure 1. Microstructure of powders of Cr–Al–C (*a, b*) and Cr_3C_2 –Al (*c, d*) systems produced by the MChS method for 1.5 (*a, c*) and 5 (*b, d*) h

was not revealed in the XRD patterns, which may be the result of its transition to an amorphous state or refinement in the mill during processing to a nanosize. With an increase in the processing time to 5 h, a slight shift towards lower angles of the chromium lines is observed, which may indicate the dissolution of aluminium in chromium to form a solid solution.

In the case of Cr_3C_2 –Al system powder, during the MChS process, both at 1.5 and 5 h of processing, the starting components of the mixture of chromium and aluminium carbide interact with the formation of Cr_2AlC MAX phase and a small amount of the intermetallic Cr_5Al_8 compound in the final product of the MChS phase (Figure 2, *c, d*). In addition to the start-

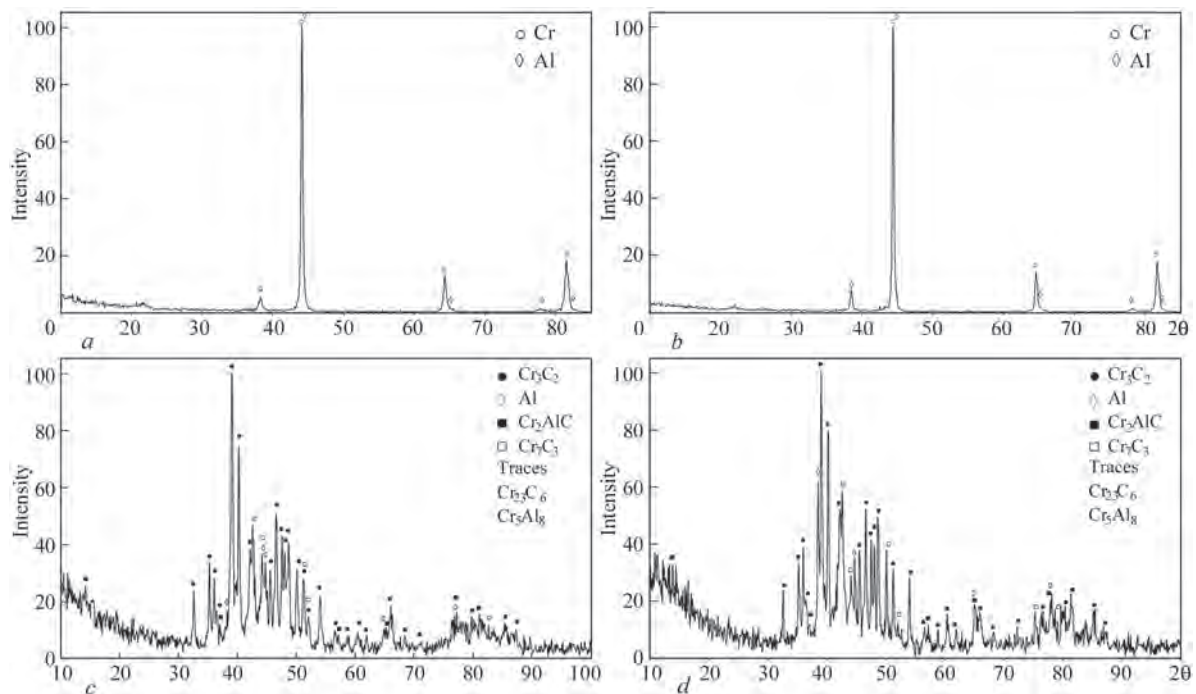


Figure 2. X-ray diffraction patterns of powders of Cr–Al–C (*a, b*) and Cr_3C_2 –Al (*c, d*) systems produced by the MChS method for 1.5 (*a, c*) and 5 (*b, d*) h

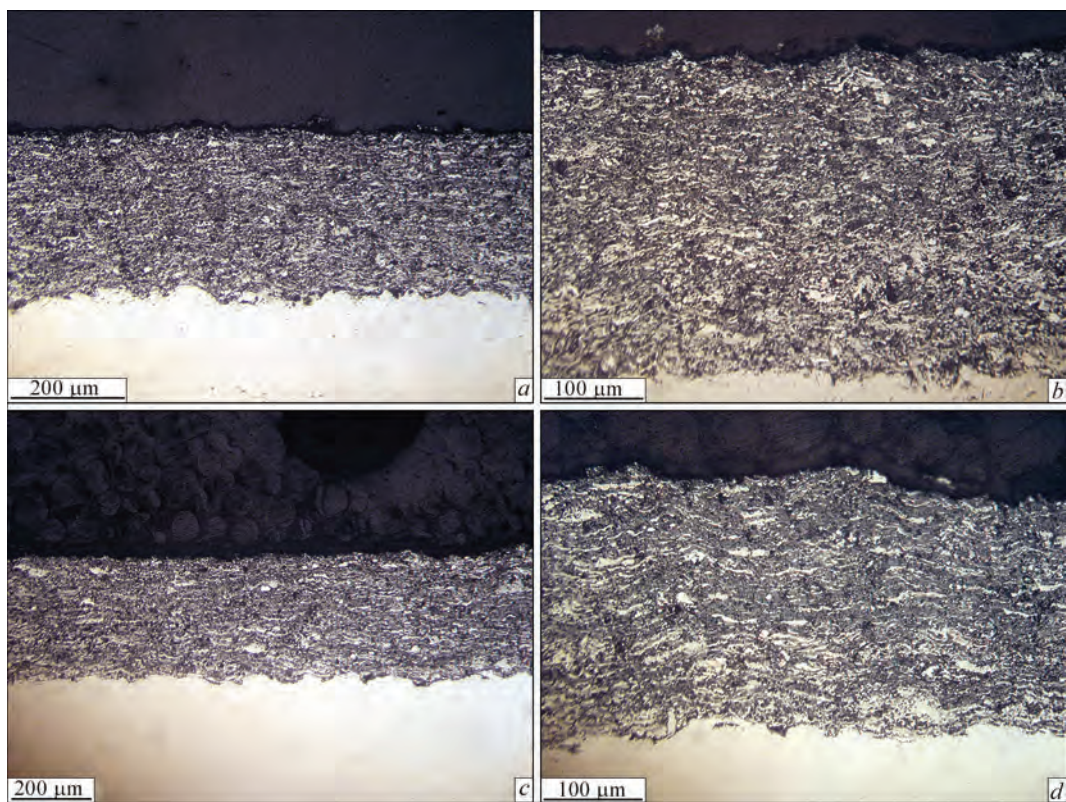


Figure 3. Microstructure of detonation spray coatings produced from MChS powders: *a, b* — Cr–Al–C; *c, d* — Cr₃C₂–Al

ing components Cr₃C₂ and Al, as well as Cr₇C₃ and Cr₂₃C₆ carbides are present in the powders.

Since the phase composition of the produced MChS powders does not differ significantly during processing for 1.5 and 5 h, further MChS powders of Cr–Al–C and Cr₃C₂–Al systems produced within 1.5 h of processing were used to study the formation of coatings under detonation spraying conditions.

As a result of the detonation spraying of the produced MChS powders, dense coatings with a thin-lamellar structure are formed consisting of alternating light and dark grey oxide lamellae (Figure 3). The amount of the oxide component in Cr–Al–C coating is ~35 %, the porosity is ~7 %; in Cr₃C₂–Al coating — ~30 % and 4 %, respectively. The microhardness of Cr–Al–C and Cr₃C₂–Al coatings is 4910±1150 and 5030±1015 MPa, respectively. The presence of a large discrepancy of microhardness values in the range of 3000–10000 MPa is

associated with the presence of heterogeneous phases in the coating.

The main phases in the sprayed coatings of Cr–Al–C and Cr₃C₂–Al systems are chromium carbide phases in the quantitative ratio according to the intensity of the peaks: Cr₇C₃ > Cr₃C₂ > Cr₂₃C₆ (Figure 4). In the case of spraying a coating of Cr–Al–C system, the appearance of chromium carbides is predetermined by the interaction of the starting components of chromium powder and graphite during the spraying process. In the case of spraying Cr₃C₂–Al coating, the appearance of a significant amount of Cr₇C₃ carbide is predetermined by the partial transformation of Cr₃C₂ carbide during the spraying process under the influence of temperature and the interaction of powder particles with ambient oxygen. The coatings contain a significant amount of chromium oxide Cr₂O₃ and a small amount of aluminium oxide Al₂O₃ of the co-

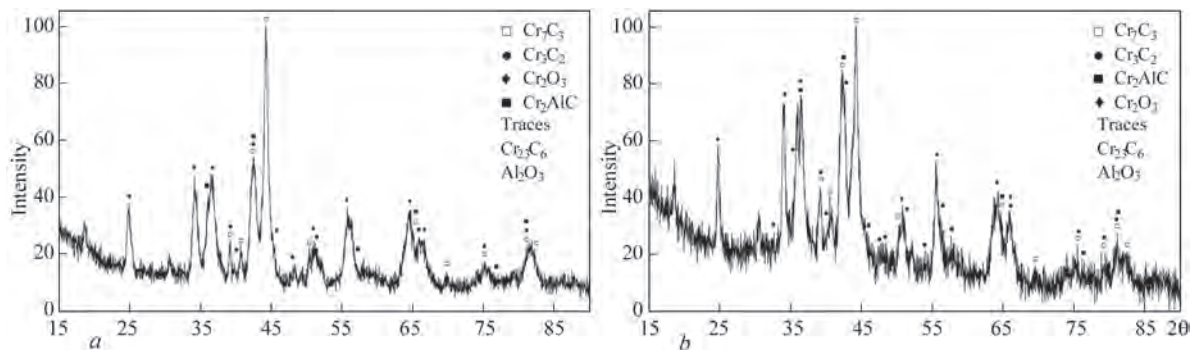
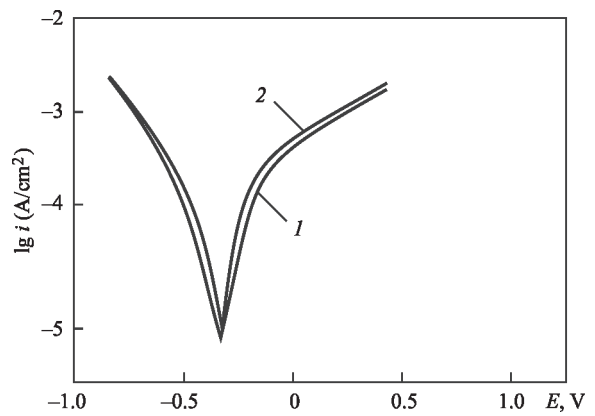
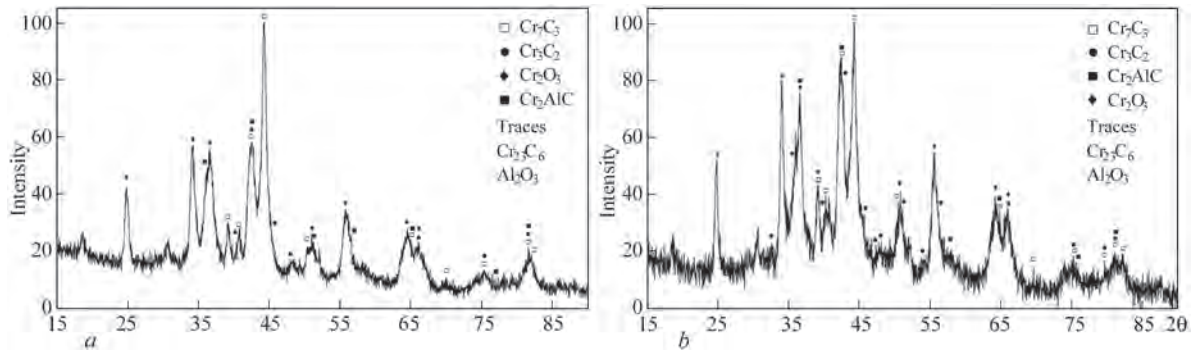


Figure 4. X-ray diffraction patterns of detonation spray coatings of Cr–Al–C (*a*) and Cr₃C₂–Al (*b*) systems

Table 3. Electrochemical characteristics of Cr–Al–C and Cr_3C_2 –Al detonation spray coatings in a 3 % NaCl solution

Material	E_{st} , V	E_c , V	i_c , A/cm ²
Cr–Al–C DS coating	–0.40	–0.36	$2.0 \cdot 10^{-6}$
Cr_3C_2 –Al DS coating	–0.44	–0.38	$1.6 \cdot 10^{-6}$
Steel 3	–0.54	–0.52	$2.4 \cdot 10^{-5}$
40Kh13	–0.28	–0.26	$2.0 \cdot 10^{-6}$
12Kh18M10T	–0.16	–0.18	$1.6 \cdot 10^{-6}$


Figure 5. Polarization curves of detonation coatings in a 3 % NaCl solution: 1 — Cr–Al–C; 2 — Cr_3C_2 –Al

Figure 6. X-ray diffraction patterns of detonation spray coatings of Cr–Al–C (a) and Cr_3C_2 –Al (b) systems after electrochemical studies in a 3 % NaCl solution

rundum modification. In contrast to MChS powders, the coatings do not contain a pure aluminium phase, which indicates its complete interaction during the spraying process with the components of Cr, C, Cr_3C_2 powders and ambient oxygen. Both types of coatings contain Cr_2AlC MAX phase, and the intensity of MAX phase peaks in Cr_3C_2 –Al coating is significantly higher, which may indicate a greater amount of MAX phase in it. Also, an increase in the intensity of peaks corresponding to MAX phase on the XRD pattern of Cr_3C_2 –Al coating relative to the peaks on the XRD pattern of the MChS powder is noted, which indicates the interaction of powder components during the process of detonation spraying and the formation of a coating layer with the formation of MAX phase.

The studies of the kinetics of the electrode potentials of detonation coatings of Cr–Al–C and Cr_3C_2 –Al systems have made it possible to find that the value of the electrode potential of the specimens stabilizes after 25–30 min. The stationary potentials E_{st} are –0.4 and –0.44 V, respectively. The characteristic polarization curves of the coatings are shown in Figure 5; the electrochemical characteristics of the coatings are given in Table 3. For comparison, Table 3 also shows the characteristics of St3 and stainless steels 40Kh13 and 12Kh18N10T.

The analysis of the polarization curves showed that the course of cathodic and anodic polarization

curves for detonation coatings of both compositions is almost the same. The corrosion current for Cr_3C_2 –Al system coating is 1.25 times lower than that of Cr–Al–C system coating, which indicates its higher corrosion resistance. This is obviously predetermined by the higher content of MAX phase in Cr_3C_2 –Al coating and the slightly lower porosity of this coating. After electrochemical studies, the phase composition of the sputtered coatings does not change significantly (Figure 6), i.e., no corrosion processes occur on the surface of the coated specimens. The developed coatings of both compositions are not inferior to stainless steels in terms of their corrosion resistance and are by an order of magnitude higher than carbon steel.

CONCLUSIONS

The carried out studies of the products of mechanochemical synthesis of powder mixtures of Cr–Al–C and Cr_3C_2 –Al compositions showed the formation of conglomerate-type particles with a size in the range of $d_{10} = 8\text{--}10$, $d_{50} = 16\text{--}21$, $d_{90} = 40\text{--}45$ μm after 1.5–5 h of processing. In Cr_3C_2 –Al system, the formation of Cr_2AlC MAX phase was recorded after 1.5 h of processing; in the case of Cr–Al–C system, no interaction of components with the formation of new phases occurs during the MChS process.

As a result of detonation spraying of the produced MChS powders, dense coatings with a thin-lamellar

structure are formed. The presence of Cr_2AlC MAX phase, as well as chromium carbides and oxide phases Cr_2O_3 and Al_2O_3 is recorded in the coatings. The content of MAX phase in the coatings relative to the MChS powder is higher in the coatings formed from the powders of Cr_3C_2 –Al system; an increase in the content of MAX phase in the coating relative to the MChS powder was found due to the interaction reactions between the starting components during the spraying process.

Based on the results of potentiostatic studies in a 3 % NaCl solution, it was found that coatings based on Cr_3C_2 –Al system are characterized by a lower corrosion current ($1.6 \cdot 10^{-6}$ A/cm²) compared to Cr–Al–C ($2.0 \cdot 10^{-6}$ A/cm²), which confirms their higher corrosion resistance due to the higher content of MAX phase and denser structure. The developed coatings of both compositions are not inferior to stainless steels in terms of their indices of corrosion resistance and can be recommended for operation in this aggressive environment.

REFERENCES

- Gonzalez-Julian, J. (2020) Processing of MAX phases: From synthesis to applications. *J. of the American Ceramic Society*, 104(2), 659–690. DOI: <https://doi.org/10.1111/jace.17544>
- Sun, Z.M. (2011) Progress in research and development on MAX phases: A family of layered ternary compounds. *Inter. Materials Reviews*, 56(3), 143–166. DOI: <https://doi.org/10.1179/1743280410y.0000000001>
- Tian, W., Wang, P., Zhang, G. et al. (2007) Mechanical properties of Cr_2AlC ceramics. *J. of the American Ceramic Society*, 90(5), 1663–1666. DOI: <https://doi.org/10.1111/j.1551-2916.2007.01634.x>
- Tian, W., Wang, P., Zhang, G. et al. (2006) Synthesis and thermal and electrical properties of bulk Cr_2AlC . *Scripta Materialia*, 54(5), 841–846. DOI: <https://doi.org/10.1016/j.scriptamat.2005.11.009>
- Majed, R.A., Hasan, A.M., Faleh, R.F. (2015) Corrosion behavior of V_2AlC and Cr_2AlC materials in acidic media. *Engineering and Technology J.*, 33(4), 845–854. DOI: <https://doi.org/10.30684/etj.33.4A.8>
- Azina, C., Badie, S., Litnovsky, A. et al. (2023) Optical properties and corrosion resistance of Ti_2AlC , Ti_3AlC_2 , and Cr_2AlC as candidates for concentrated solar power receivers. *Solar Energy Materials and Solar Cells*, 259, 112433. DOI: <https://doi.org/10.1016/j.solmat.2023.112433>
- Desai, V., Shrivastava, A., Zala, A.B. et al. (2024) Manufacturing of high purity Cr_2AlC MAX phase material and its characterization. *J. of Mater. Eng. and Performance.*, 33, 9841–9849. DOI: <https://doi.org/10.1007/s11665-024-09513-4>
- Shamsipoor, A., Farvizi, M., Razavi, M., Keyvani, A. (2019) Influence of processing parameters on the microstructure and wear performance of Cr_2AlC MAX phase prepared by spark plasma sintering method. *J. of Alloys and Compounds*, 815, 152345. DOI: <https://doi.org/10.1016/j.jallcom.2019.152345>
- Xiao, L.-O., Li, S.-B., Song, G., Sloof, W.G. (2011) Synthesis and thermal stability of Cr_2AlC . *J. of the European Ceramic Society*, 31(8), 1497–1502. DOI: <https://doi.org/10.1016/j.jeurceramsoc.2011.01.009>
- Gonzalez-Julian, J., Llorente, J., Bram, M. et al. (2017) Novel Cr_2AlC MAX-phase/SiC fiber composites: Synthesis, processing and tribological response. *J. of the European Ceramic Society*, 37(2), 467–475. DOI: <https://doi.org/10.1016/j.jeurceramsoc.2016.09.029>
- Yeh, C.L., Kuo, C.W. (2011) Effects of Al and Al_4C_3 contents on combustion synthesis of Cr_2AlC from Cr_2O_3 –Al– Al_4C_3 powder compacts. *J. of Alloys and Compounds*, 509 (3), 651–655. DOI: <https://doi.org/10.1016/j.jallcom.2010.09.169>
- Field, M.R., Carlsson, P., Eklund, P. et al. (2014) A combinatorial comparison of DC and high power impulse magnetron sputtered Cr_2AlC . *Surf. and Coat. Technol.*, 259, 746–750. DOI: <https://doi.org/10.1016/j.surfcoat.2014.09.052>
- Su, R., Zhang, H., Meng, X. et al. (2017) Synthesis of Cr_2AlC thin films by reactive magnetron sputtering. *Fusion Engineering and Design*, 125, 562–566. DOI: <https://doi.org/10.1016/j.fusengdes.2017.04.129>
- Vihilianska, N.V., Filonenko, D.V., Yushchenko, A.O. et al. (2024) Thermal spraying of coatings, containing Cr_2AlC MAX-phase (Review). *The Paton Welding J.*, 3, 24–32. DOI: <https://doi.org/10.37434/tpwj2024.03.04>
- Go, T., Sohn, Y.J., Mauer, G. et al. (2019) Cold spray deposition of Cr_2AlC MAX phase for coatings and bond-coat layers. *J. of the European Ceramic Society*, 39(4), 860–867. DOI: <https://doi.org/10.1016/j.jeurceramsoc.2018.11.035>
- Zhang, F., Yan, S., Li, C. et al. (2019) Synthesis and characterization of MAX phase Cr_2AlC based composite coatings by plasma spraying and post annealing. *J. of the European Ceramic Society*, 39(16), 5132–5139. DOI: <https://doi.org/10.1016/j.jeurceramsoc.2019.08.039>
- Zhang, F., Yu, G., Yan, S. et al. (2023) Characterization and reaction mechanism of in-situ micro-laminated Cr_2AlC coatings by plasma spraying $\text{Cr}_3\text{C}_2/\text{Al}/\text{Cr}$ powder mixtures. *Surf. and Coat. Technol.*, 456, 129271. DOI: <https://doi.org/10.1016/j.surfcoat.2023.129271>
- Vigilianska, N., Iantsevitch, C., Tsymbalista, T. et al. (2024) Formation of coatings containing Cr_2AlC MAX phase during plasma spraying of mixture of Cr_3C_2 +Al powders. *Coatings*, 14(12), 1584. DOI: <https://doi.org/10.3390/coatings14121584>

ORCID

N.V. Vigilianska: 0000-0001-8576-2095,
C. Senderowski: 0000-0002-0331-3702,
T.V. Tsymbalista: 0000-0001-9569-7776,
K.V. Iantsevitch: 0000-0002-3975-7727,
A.I. Kildiy: 0000-0001-8133-8705,
O.Yo. Gudymenko: 0000-0002-5866-8084

CONFLICT OF INTEREST

The Authors declare no conflict of interest

CORRESPONDING AUTHOR

N.V. Vigilianska

E.O. Paton Electric Welding Institute of the NASU
11 Kazymyr Malevych Str., 03150, Kyiv, Ukraine.
E-mail: pewinataliya@gmail.com

SUGGESTED CITATION

N.V. Vigilianska, C. Senderowski,
T.V. Tsymbalista, K.V. Iantsevitch, A.I. Kildiy,
O.Yo. Gudymenko (2025) Detonation sputtering
of coatings containing Cr_2AlC MAX phase.
The Paton Welding J., 6, 25–30.
DOI: <https://doi.org/10.37434/tpwj2025.06.04>

JOURNAL HOME PAGE

<https://patonpublishinghouse.com/eng/journals/tpwj>

Received: 02.05.2025

Received in revised form: 19.05.2025

Accepted: 27.06.2025

FEATURES OF SMELTING OF HEAT-RESISTANT TITANIUM ALLOY OF THE Ti–Nb–Al–Mo–Zr ALLOYING SYSTEM BY ELECTRON BEAM MELTING WITH A COLD HEARTH

S.V. Akhonin¹, V.O. Berezos¹, A.Yu. Severyn¹, O.H. Yerokhin¹, V.V. Pashynskiy²

¹E.O. Paton Electric Welding Institute of the NASU
11 Kazymyr Malevych Str., 03150, Kyiv, Ukraine

²Technical University “Metinvest Polytechnic” LLC
80 Pivdenne Highway, 69008, Zaporizhzhia, Ukraine

ABSTRACT

In order to develop the technique and technology of smelting ingots of heat-resistant alloys based on titanium with the content of the Ti_2AlNb ortho-phase, experimental works were carried out to produce the experimental Ti–39Nb–16Al–2.6Mo–1.4Zr alloy. The results of studies of the ingot produced by double electron beam remelting are presented. The developed technology and experimental melting of the 110 mm diameter Ti–39Nb–16Al–2.6Mo–1.4Zr ingot by the electron beam melting method with a cold hearth showed the prospects of using the EBM method for producing ingots of heat-resistant alloys based on titanium with the content of the Ti_2AlNb ortho-phase.

KEYWORDS: electron beam melting, cold hearth, ingot, refractory elements, chemical composition, titanium aluminide, ortho-phase

INTRODUCTION

Creation of intermetallic alloys of the Ti–Al–Nb system and technologies for their production are a perspective direction, which is being developed in the world in the field of new metal materials with a high level of heat resistance, high-temperature strength and thermal stability [1–3]. Ortho-alloys may well replace heat-resistant steels and nickel alloys used in the rotor and stator of a high-pressure compressor, but despite the advantages of these alloys, none of ortho-alloys are still used abroad. Obviously, this is associated with the fact that such alloys have proved to be quite difficult in metallurgical production. The need in using more expensive and refractory elements (niobium, molybdenum, etc.) for alloying, providing high homogeneity of ingot composition, the use of equipment with a protective atmosphere, strict testing of macro- and microstructure in semi-finished products are the main reasons for slowing down the industrial implementation of this grade of alloys. Nevertheless, there are real prerequisites and technical capabilities to overcome many of these difficulties.

The most interesting are ortho-alloys within the Ti–(22–25)Al–(25–30)Nb alloying range (at.%), which contain precipitations of the Ti_2AlNb ortho-phase. It should be noted that although an increase in the aluminium content above 25 at.% improves the heat resistance of the material, it leads to a drop in toughness [4, 5]. In addition to aluminium and niobium, ortho-alloys may

contain additional alloying elements. Thus, macroalloying with an element such as Mo leads to an expansion of the β -phase existence area, which acts as a plastic matrix and layering of diffusion processes in the volume and at the interfacial boundaries of the material, increasing its melting point and facilitating softening at operating temperatures. Zirconium, acting as a neutral hardener in relation to titanium and intermetallic titanium alloys, provides solid-solution hardening of the main phases and increases creep resistance.

One of the methods of producing intermetallic ingots is smelting technology based on independent heating sources. It should be considered that heat-resistant titanium-based alloys contain such alloying elements as Nb, Zr, Mo, which, like titanium, have high chemical activity towards gases at elevated temperatures, which necessitates melting of these materials in a protective atmosphere or under vacuum [6]. Among the modern methods of special electrometallurgy, electron beam melting is the most efficient method of vacuum metallurgy [7, 8].

As shown in [6], when smelting ortho-alloys with a high content of refractory alloying elements (niobium, molybdenum, tungsten) by electron beam melting, it is significantly more difficult to ensure a uniform chemical composition in the ingot volume. It is especially difficult to provide a uniform content of elements with high vapour elasticity, such as aluminium and chromium. Therefore, in [9], a mathematical model of the processes of evaporation of alloying



Figure 1. Laboratory electron beam UE-208M installation

elements from titanium alloys during electron beam melting with a cold hearth was developed and, using the example of the process of producing the titanium aluminide Ti–29Al–12Nb–3Cr–3Zr alloy ingot, the dependencies of the concentration of alloying elements in the ingot on the technological parameters of melting and the content of alloying elements in the initial charge were established.

Earlier studies have shown that the specified chemical composition of titanium intermetallic alloys can be achieved only by performing at least a double electron beam remelting. In addition, to facilitate adding of alloying elements into the alloy composition, various master alloys were used, which are quite scarce and expensive. Therefore, it is of particular interest to develop a technology that allows using pure components to produce materials of this grade.

RESEARCH PROCEDURE

In order to practice the technique and technology of smelting ingots of titanium-based high-temperature alloys containing the Ti_2AlNb ortho-phase, experimental works were carried out to produce an experimental Ti–39Nb–16Al–2.6Mo–1.4Zr alloy (wt.%).

For experimental studies, a multipurpose laboratory electron beam UE-208M installation [10] was used (Figure 1).

The technological sequence of ingot smelting consisted of the following stages: calculation of the quantity of components of the initial charge, taking into account evaporation losses; preparation of equipment and technological fixture for melting; formation of consumable billets; melting process; sampling for chemical and gas analysis of a smelted ingot.

Before conducting the experimental ingot melts, the equipment was prepared by cleaning the melting chamber, the electron beam gun plate, the cold hearth and the mold, and the bottom-plate from condensation, dust and metal residues from previous melts.



Figure 2. Charge billet for the production of ortho-titanium aluminide Ti–39Nb–16Al–2.6Mo–1.4Zr alloy

Experimental melts were carried out in a 110 mm diameter mold. The works on producing a heat-resistant titanium Ti–39Nb–16Al–2.6Mo–1.4Zr alloy ingot were carried out in two stages. When smelting titanium-based alloys by electron beam melting, the main problem of alloying elements distribution arises namely with elements that have high vapour elasticity [11, 12]. Therefore, in order to ensure a more uniform distribution of aluminium in the final ingot, at the first stage, an intermediate billet of a commercial titanium aluminide was smelted without adding refractory alloying elements. The charge billet was prepared, which included briquettes of TG-120 titanium sponge and a commercially pure aluminium (Figure 2).

At the second stage, alloying elements in the form of electrolytic niobium, commercially pure molybdenum and refined zirconium iodide were added to the produced ingot of a commercial titanium aluminide.

After loading the charge, the installation was vacuumed to the level of a residual pressure in the melting chamber of 10^{-2} Pa. Then the billet was melted into a cold hearth until it was filled and the liquid metal was periodically poured into a copper water-cooled mold.



Figure 3. Melting process of an ingot with a diameter of 110 mm made of ortho-titanium aluminide Ti–39Nb–16Al–2.6Mo–1.4Zr alloy



Figure 4. Ingot with a diameter of 110 mm made of ortho-titanium aluminide Ti-39Nb-16Al-2.6Mo-1.4Zr alloy

The first pouring portions were used to form a seed for the future ingot. Then, the achieved technological mode was used to smelt the ingot of the required height (Figure 3).

During the experimental melts, the following technological parameters were monitored: melting rate, electron beam current and accelerating voltage. The numerical values of the accelerating voltage and beam current were measured and adjusted using the devices intended for this purpose. The melting rate was controlled by the rate of feeding the consumable billet into the melting zone.

**Technological parameters of melting an ingot
with a diameter of 110 mm made
of ortho-titanium aluminide
Ti-39Nb-16Al-2.6Mo-1.4Zr alloy**

Total EB heating power, kW	130
Power in the mold, kW	30
Melting rate, kg/h	30

After melting, the ingot was kept in a vacuum chamber until it cooled completely. An ingot with a

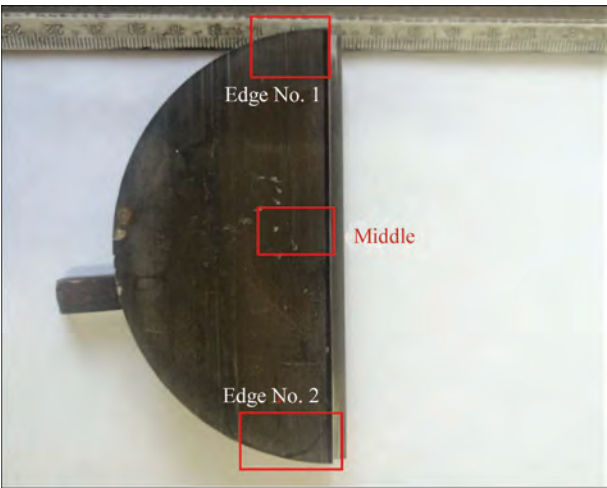


Figure 5. Scheme of sampling for microstructure examination diameter of 110 mm and a weight of approximately 40 kg was produced (Figure 4).

The head part with the shrinkage shell was cut off from the ingot and samples were taken for chemical analysis. The samples were taken at three points in the form of chips by drilling. In this case, at first, the upper layer of the ingot was removed to a depth of at least 5 mm, and then chips were sampled for analysis to a depth of 10 mm from the surface of the ingot.

To accurately analyse the content of alloying elements in the produced ingot, inductively coupled plasma/optical emission spectrometry (ICP-OES) was used in the ICAP 6500 DUO ICP-spectrometer. The studies showed that after a double electron beam remelting, the distribution of alloying elements was satisfactory and did not exceed the technical specifications (Table 1). The oxygen content was 0.04 wt.%, which corresponded to the data of the certificate of oxygen content in the TG-120 titanium sponge.

To study the microstructure of the material in the cast state by the method of optical metallography, samples were taken from the produced ingot according to the scheme shown in Figure 5.

The general appearance of the microstructure at magnifications $\times 50$, 500 and 1000 is shown in Figure 6. The analysis of the images (Figure 6, *a-c*, $\times 50$) shows that the structure is formed by equilibrium grains of the β -phase body-centered cubic lattice with dispersed precipitations in the grain body. Comparison of Figure 6, *b* with Figure 6, *a, c* shows that the grain size in the middle zone is coarser than in the peripheral zones of the ingot. This is explained by the

Table 1. Chemical composition of an ingot with a diameter of 110 mm made of ortho-titanium aluminide Ti-39Nb-16Al-2.6Mo-1.4Zr alloy produced by EBM, wt.%

Ingot part	Nb	Al	Mo	Zr	Ti	O
Top	39.2	16.4	2.62	1.37	Base	0.04
Middle	39.2	15.3	2.76	1.36		
Bottom	39.7	14.9	2.63	1.35		

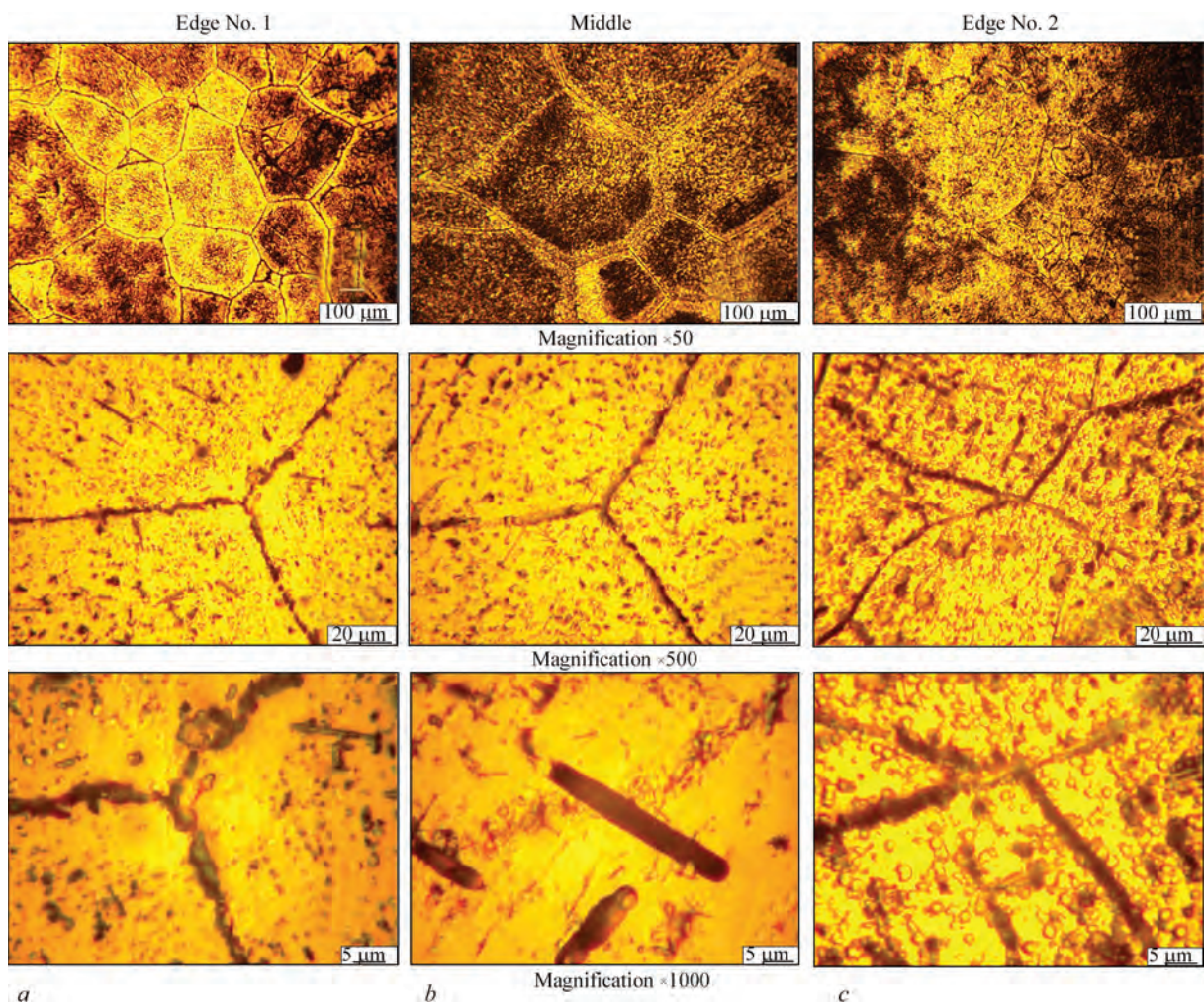


Figure 6. General appearance of the cast metal microstructure: *a* — sampling place corresponds to the edge 1 zone; *b* — middle; *c* — edge 2

difference in the cooling rate of the periphery and centre of the ingot.

In order to study the morphology of the phases precipitated in the grain body, the microstructure of the material was examined at magnifications of $\times 500$ and $\times 1000$ (Figure 6). The analysis of the microstructures shows that the bulk of the precipitations are dispersed particles of approximately equilibrium shape, which are localised in the grain body. The grain boundaries are free of precipitations (Figure 6, *a–c*, $\times 500$). At the same time, in the middle zone, separate lamellar precipitations of 20–30 μm length are observed (Figure 6, *b*, $\times 1000$). Based on the particles morphology, it can be assumed that dispersed particles are α_2 -phase (Ti_3Al), and lamellar ones are θ -phase crystals (orthogonal Ti_2AlNb phase).

Thus, the developed technology and experimental melts of the Ti–39Nb–16Al–2.6Mo–1.4Zr ingot with a diameter of 110 mm by the electron beam melting method with a cold hearth showed the prospects of using the EBM method to produce ingots of heat-resistant alloys based on titanium with the content of the Ti_2AlNb ortho-phase.

CONCLUSIONS

1. The Ti–39Nb–16Al–2.6Mo–1.4Zr alloying system containing intermetallic Ti_2Al and Ti_2AlNb phases was selected for experimental melts.
2. A new method of adding alloying elements into the alloy was developed and an experimental melting of a 110 mm diameter ingot was carried out.
3. It was shown that electron beam melting allows producing ingots of titanium-based alloys with a high content of aluminium and niobium and a sufficiently uniform distribution of alloying elements.
4. An examination of the microstructure of the cast metal showed that the structure is formed by equilibrium β -phase grains with dispersed inclusions in the grain body. Based on the particles morphology, it can be assumed that dispersed precipitations are α_2 -phase, and lamellar precipitations are θ -phase crystals (orthogonal Ti_2AlNb phase).

REFERENCES

1. Kumpfert, J. (2001) Intermetallic alloys based on orthorhombic titanium aluminide. *Adv. Eng. Mater.*, **3**, 851–864. DOI: [https://doi.org/10.1002/1527-2648\(200111\)3:113.0.CO;2-G](https://doi.org/10.1002/1527-2648(200111)3:113.0.CO;2-G)

2. Partridge, A., Shelton, E.F.J. (2001) Processing and mechanical property studies of orthorhombic titanium-aluminide-based alloys. *Air Space Eur.*, **3**, 170–173. DOI: [https://doi.org/10.1016/S1290-0958\(01\)90085-1](https://doi.org/10.1016/S1290-0958(01)90085-1)
3. Gogia, A.K. (2005) High-temperature titanium alloys. *Defence Sci. J.*, **55**, 49–173. DOI: <https://doi.org/10.14429/dsj.55.1979>
4. Chen, Y., Niu, H., Kong, F., Xiao, S. (2011) Microstructure and fracture toughness of a β phase containing TiAl alloy. *Intermetallics*, **19**, 1405–1410. DOI: <https://doi.org/10.1016/j.intermet.2011.05.006>
5. Emura, S., Araoka, A., Hagiwara, M. (2003) B2 grain size refinement and its effect on room temperature tensile properties of a Ti–22Al–27Nb orthorhombic intermetallic alloy. *Scripta Mater.*, **48**, 629–634. DOI: [https://doi.org/10.1016/s1359-6462\(02\)00462-1](https://doi.org/10.1016/s1359-6462(02)00462-1)
6. Akhonin, S.V., Severin, A.Yu., Berezos, V.A. (2015) Development of technology of adding the refractory alloying elements into alloys on the base of Ti_2AlNb intermetallic in electron beam melting. *Sovremennaya Elektrometallurgiya*, **3**, 12–15 [in Russian].
7. Vutova, K., Vassileva, V., Stefanova, V. et al. (2019) Effect of electron beam method on processing of titanium technogenic material. *Metals*, **9**(6), 683. DOI: <https://doi.org/10.3390/met9060683>
8. Liu, Q.L., Li, X.M., Jiang, Y.H. (2016) Research progress of electron beam cold hearth melting for titanium and titanium alloys. *Hot Work. Technol.*, **45**, 9–14.
9. Akhonin, S.V., Severin, A.Yu., Berezos, V.A., Erokhin A.G. (2013) Mathematical modelling of evaporation processes in melting of ingots of multicomponent titanium alloys in electron beam equipment with a cold hearth. *Advances in Electrometallurgy*, **4**, 288–295.
10. Akhonin, S.V., Pikulin, A.N., Berezos, V.A. et al. (2019) Laboratory electron beam unit UE-208M. *Suchasna Elektrometalurhiya*, **3**, 15–22. DOI: <https://doi.org/10.15407/sem2019.03.03>
11. Wang, Y., Gao, L., Xin, Y. et al. (2024) Numerical modeling of electron beam cold hearth melting for the cold hearth. *Minerals*, **14**(6), 601. DOI: <https://doi.org/10.3390/min14060601>
12. Bellot, J.-P., Hess, E., Hitzer, D. (2000) Aluminum volatilization and inclusion removal in the electron beam melting and refining of titanium alloys. *Metallurgical, Materials Transact.*, **31B**(8), 845–859.

ORCID

S.V. Akhonin: 0000-0002-7746-2946,
V.O. Berezos: 0000-0002-5026-7366,
A.Yu. Severyn: 0000-0003-4768-2363,
O.H. Yerokhin: 0000-0003-2105-5783,
V.V. Pashynskiy: 0000-0003-0118-4748

CONFLICT OF INTEREST

The Authors declare no conflict of interest

CORRESPONDING AUTHOR

V.O. Berezos

E.O. Paton Electric Welding Institute of the NASU
11 Kazymyr Malevych Str., 03150, Kyiv, Ukraine.
E-mail: titan.paton@gmail.com

SUGGESTED CITATION

S.V. Akhonin, V.O. Berezos, A.Yu. Severyn,
O.H. Yerokhin, V.V. Pashynskiy (2025)
Features of smelting of heat-resistant titanium alloy
of the Ti–Nb–Al–Mo–Zr alloying system by
electron beam melting with a cold hearth. *The Paton
Welding J.*, **6**, 31–35.
DOI: <https://doi.org/10.37434/tpwj2025.06.05>

JOURNAL HOME PAGE

<https://patonpublishinghouse.com/eng/journals/tpwj>

Received: 07.04.2025

Received in revised form: 13.05.2025

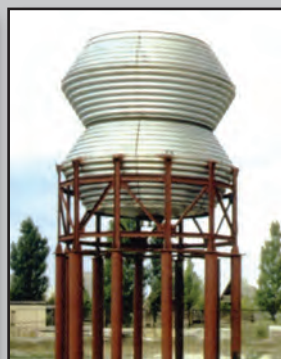
Accepted: 25.06.2025



Developed at PWI

METAL TRANSFORMABLE-VOLUME STRUCTURES

Shell structures of a transformable volume with transformation coefficient of 5–50 have been designed and manufactured, which have smaller dimensions during transportation, and are transformed into tanks of a specified volume at application of small inner pressure. On the Earth such



structures are used under extreme conditions of delivery and mounting. In Space they can have the functions of tunnels — passages between the individual space modules, additional laboratory premises, waste containers, etc.

DOI: <https://doi.org/10.37434/tpwj2025.06.06>

THE EFFECT OF ANNEALING ON THE STRUCTURE
AND PROPERTIES OF WELDED JOINTS
OF HEAT-RESISTANT PSEUDO- α -TITANIUM ALLOY
Ti–Al–Zr–Sn–Mo–Nb–Si ALLOYING SYSTEM

S.V. Akhonin¹, V.Yu. Bilous¹, V.V. Pashynskyi², R.V. Selin¹, A.Iu. Severin¹, E.L. Vrzhyzhevskiy¹

¹E.O. Paton Electric Welding Institute of the NASU
11 Kazymyr Malevych Str., 03150, Kyiv, Ukraine

²Technical University “Metinvest Polytechnic” LLC
80 Pivdenne Highway, 69008, Zaporizhzhia, Ukraine

ABSTRACT

The effect of furnace annealing after electron beam welding (EBW) and gas tungsten arc welding (GTAW) on the properties of welded joints of a pseudo- α -titanium alloy of the Ti–Al–Zr–Sn–Mo–Nb–Si system was investigated. To compare the properties of welded joints in the as-welded state and after additional heat treatment, a quality criterion was introduced. It was established that annealing promotes the formation of a finer microstructure in the welded joints of the heat-resistant pseudo- α -titanium alloy of Ti–Al–Zr–Sn–Mo–Nb–Si alloying system produced by EBW, resulting in a tensile strength of 980 MPa, which is 95 % of the base metal strength; the impact toughness of the annealed welded joints remained high at 17.9 J/cm². Annealing after GTAW also leads to microstructural refinement of the welded joints. A comparative analysis of the quality coefficients of EB and GTA welded joints demonstrated the superior combination of mechanical properties in EB joints, both in the as-welded state and after annealing. Annealing application enabled an improvement in the mechanical properties of EB joints to levels comparable to those achieved with additional local heat treatment (LHT).

KEYWORDS: heat-resistant titanium alloy, microstructure, mechanical properties, electron beam welding, gas tungsten arc welding

INTRODUCTION

In the last decades a significant increase in the scope of research is observed, the objective of which is producing titanium alloys with a new set of properties [1–3]. Heat-resistant titanium alloys with intermetallic strengthening are considered promising materials for aviation, space and automotive technology. The highest heat resistance is demonstrated by doped alloys of Ti–Si–X system, owing to formation of a framework of strengthening phases in the cast state, arising at eutectic crystallization in Ti–Al–Si system, α -Ti, Ti₃Al and TiAl acting as the matrix, and Ti₅Si₃ silicide being the strengthening phase [4–7]. One of such promising alloys is the experimental multicomponent pseudo- α -alloy of Ti–Al–Zr–Sn–Mo–Nb–Si alloying system, the average chemical composition of which is given in Table 1 [8, 9]. Investigations of the properties of welded joints of alloys containing a large number of alloying elements, revealed their significant disadvantages: high proneness to alloying element liquation, strong dependence of aging duration on the content of alloying elements and impurities, as

well as low thermal stability, which are due to precipitation of intermetallics in the structure of these alloys, for instance Ti₅Si₃ [10].

The most wide-spread method of fabrication of structures from titanium alloys is gas tungsten arc welding (GTAW). For heat-resistant titanium alloys, however, it is the most rational to apply electron beam welding (EBW). Possibility of performing local preheating and further local heat treatment (LHT) in the vacuum chamber is an essential advantage of EBW technology, used to prevent cold cracking in the welded joints [11, 12]. In case of making welded joints of promising heat-resistant titanium alloy of Ti–Al–Zr–Sn–Mo–Nb–Si alloying system, EBW is complicated, in connection with a high content of silicon in the weld metal and the HAZ metal. As a result of the influence of the welding thermal cycle, structural changes take place in the weld metal and the HAZ of this alloy, resulting in formation of a stressed state and cold cracking at low ductility of silicon-alloyed metal.

In work [13], EBW influence on the structure of weld metal and the HAZ and the mechanical prop-

Table 1. Average chemical composition of the experimental heat-resistant alloy, wt. %

Al	Zr	Si	Mo	Nb	Sn	Ti
6.2–6.9	5.0–5.5	0.50–0.85	0.5–0.8	0.5–0.8	1.5–2.5	Base

Table 2. Mechanical properties of wrought alloy of Ti–Al–Zr–Sn–Mo–Nb–Si alloying system at temperatures of 20 and 600 °C

Sample	20 °C			600 °C		
	σ_t	σ_{02}	δ_s , %	σ_t	σ_{02}	δ_s , %
	MPa			MPa		
Base metal	1101–1169	1052–1107	7.7–10.4	744–765	552–575	11.5–14.6

erties of welded joints on the heat-resistant titanium alloy of Ti–Al–Zr–Sn–Mo–Nb–Si alloying system was studied, and it was shown that EBW application in combination with LHT to make welded joints of heat-resistant pseudo- α -titanium alloy of Ti–Al–Zr–Sn–Mo–Nb–Si alloying system allows producing welded joints of equal strength to the base metal, but application of additional furnace annealing is required to ensure a homogeneous structure in all the zones of the welded joint, including the HAZ.

Titanium alloy welded joints can be produced by different methods, with different values of energy input and cooling rates of the metal of the weld and HAZ. On the whole, for titanium alloys increasing some mechanical properties, for instance, strength causes the respective lowering of the ductility and impact toughness values, but this occurs disproportionately. Therefore, it is rational to determine the influence of furnace heat treatment on the properties of EB welded joints of heat-resistant pseudo- α -titanium alloy of Ti–Al–Zr–Sn–Mo–Nb–Si alloying system and to compare the properties of welded joints, produced by the most common method, namely GTAW.

Thus, it is necessary to study the influence of postweld heat treatment, namely annealing, on the structure and properties of welded joints of heat-resistant titanium alloy of Ti–Al–Zr–Sn–Mo–Nb–Si alloying system to achieve a homogeneous structure and a complex of high mechanical properties of the welded joints, as well as to compare the mechanical properties of welded joints of the heat-resistant alloy, produced by two kinds of welding: EBW and GTAW.

The objective of the work is to determine the influence of heat treatment-annealing on the structure and properties of the base metal and welded joints of the heat-resistant titanium alloy of Ti–Al–Zr–Sn–Mo–Nb–Si alloying system, produced by two kinds of welding: EBW and GTAW.

The heat-resistant titanium alloy of Ti–Al–Zr–Sn–Mo–Nb–Si alloying system differs by a high sensitivity to the thermal welding cycle. GTAW and EBW are characterized by different values of welding energy input and cooling rates of the metal of the weld and HAZ. Therefore, at the first stage of the research we will assess the annealing influence on the structure of GTA and EB welded joints. At the second stage we will compare the mechanical property values of EB and GTA welded joints and their change after annealing.

Research was performed using plates made from an ingot of heat-resistant titanium alloy of Ti–Al–Zr–Sn–Mo–Nb–Si alloying system produced by the method of electron beam melting [12]. Hot-rolled plates 10 mm thick from the mentioned alloy were made in a reversible double-roll rolling mill 500/350 of Skoda Company [13]. Rolling began at the temperature of 1050 °C, the rolling end temperature was not lower than 800 °C. After rolling, the metal was annealed at 900 °C for 1 h. After deformation treatment the alloy had high strength values ($\sigma_t = 1135$ MPa) at room temperature (Table 2); at working temperature of 600 °C — $\sigma_t = 755$ MPa, the values of material room temperature ductility being equal to 9.0 % [9].

Electron beam welding was performed in UL-144 machine, fitted with ELA 60/60 power unit [11]. Argon-arc welding was carried out by the method, most widely used for titanium alloys — gas tungsten argon-arc welding (GTAW). GTAW was conducted at straight polarity direct current, using VDU 511 power source. Properties of EB welded joints 10 mm thick and GTA joints 6 mm thick were studied.

In order to assess the effectiveness of the selected mode of welding and postweld heat treatment of the welded joints on high-strength titanium alloys, a criterion of welding mode quality in conditional units was proposed [14], which consists of the contribution of the modes of welding and heat treatment into a comprehensive increase of the total indices of strength, ductility and impact toughness of titanium alloy welded joints relative to the base metal of the respective alloy. On the whole, for titanium alloys, increase in some mechanical properties, for instance, strength causes the respective lowering of the ductility and impact toughness values. In some cases, however, this occurs disproportionately. Analysis of the obtained results of testing the mechanical characteristics of the welded joints allowed us to conclude that titanium alloy welded joints have high ductility

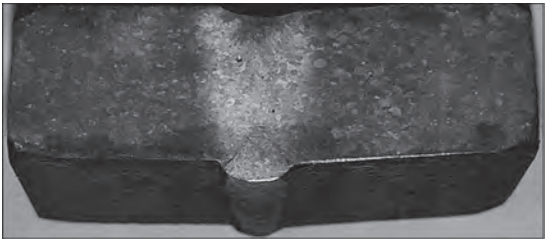


Figure 1. Macrosection of EB welded joint of the heat-resistant titanium alloy of Ti–Al–Zr–Sn–Mo–Nb–Si alloying system in the state after annealing at 850 °C

values, and the impact toughness values are also at a high level. In case we consider only the strength and impact toughness values and accept their significance as equal, the following coefficient of welding mode quality was proposed:

$$K_{wm} = 0.5(\sigma_w/\sigma_{BM}) + 0,5 (KCV_w/KCV_{BM}),$$

where K_{wm} is the quality coefficient.

The strength coefficient was also calculated [14]:

$$K_s = \sigma_w/\sigma_{BM}.$$

**INFLUENCE OF ANNEALING
ON THE MICROSTRUCTURE OF EB
WELDED JOINTS OF HEAT-RESISTANT
TITANIUM ALLOY OF Ti–Al–Zr–Sn–Mo–Nb–Si
ALLOYING SYSTEM**

Welded joints of the heat-resistant titanium alloy of Ti–Al–Zr–Sn–Mo–Nb–Si alloying system made by EBW even with application of local heat treatment have a heterogeneous nonuniform structure. To ensure formation of a homogeneous uniform structure in all the welded joint zones, including the HAZ, which eliminates the presence of metastable phases, as well as to relieve the welding stresses, welded joints of the heat-resistant titanium alloy of Ti–Al–Zr–Sn–Mo–Nb–Si alloying system made by EBW and GTAW were subjected to furnace treatment — furnace annealing.

Annealing temperature was selected proceeding from the temperature of polymorphous transformation of the heat-resistant titanium alloy of Ti–Al–Zr–Sn–Mo–Nb–Si alloying system. The temperature of polymorphous transformation of the heat-resistant titanium alloy of Ti–Al–Zr–Sn–Mo–Nb–Si alloying system was established by the methods of mathematical modeling and was confirmed experimentally [15]. During cooling the temperature range of $\beta \rightarrow (\alpha + \beta)$ transformation is in the range of 995–1025 °C, and the $(\alpha + \beta) \rightarrow \alpha$ — transformation range is within 800–825 °C. Proceeding from that, the annealing temperature of 850 °C was selected.

Annealing of the heat-resistant titanium alloy of Ti–Al–Zr–Sn–Mo–Nb–Si alloying system envisages heating up to the temperature of 850 °C, holding for 1 h, and further cooling in the furnace. Figure 1 gives an example of the transverse macrosection of the welded joint after annealing.

Figure 2 shows the structure of base metal in the central zone of a sheet after annealing at 850 °C. After the performed annealing, a clearer delineation of α -phase plates (Figure 2, *a*) and formation of intermetallic particles (Figure 2, *b*) are observed in the structure. In the base metal, not only clusters of dispersed particles in the form of chains are recorded after annealing, but also possibly monolithic silicide interlayers between plates of up to 7 μm length (Figure 2, *c*, *d*). In order to check this assumption, however, it is necessary to study the changes in the alloy phase

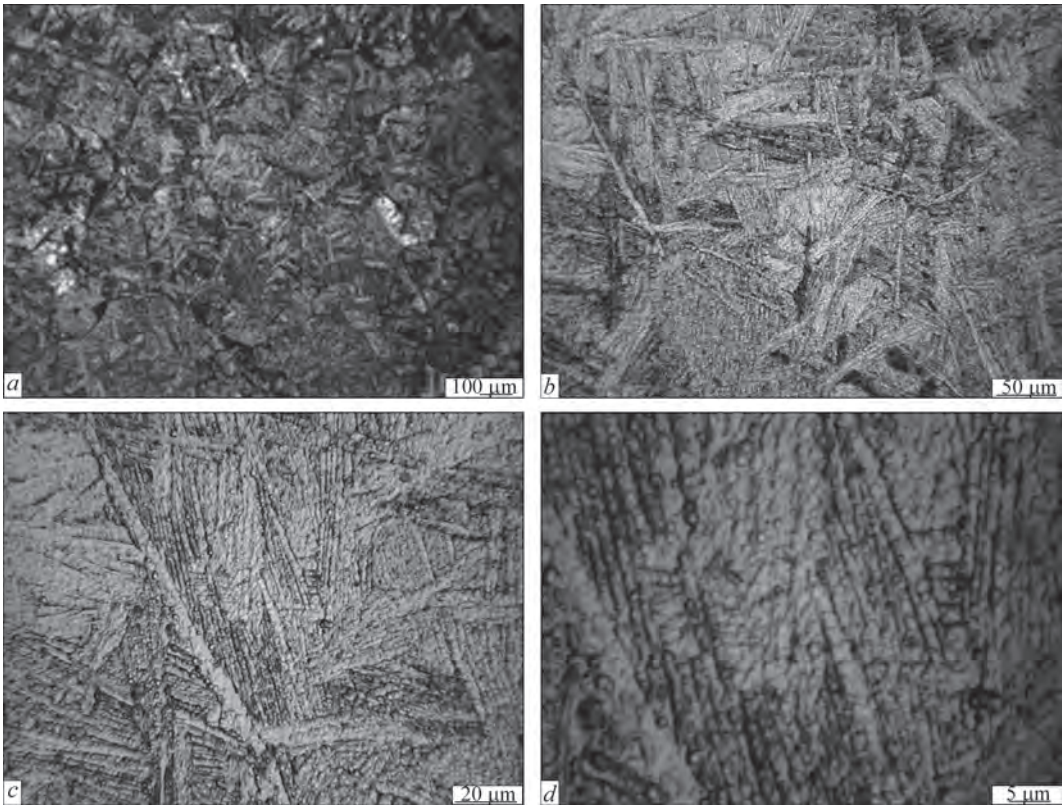


Figure 2. Microstructure of base metal of EB welded joint of the heat-resistant alloy of Ti–Al–Zr–Sn–Mo–Nb–Si alloying system in the state after annealing at 850 °C

composition by the methods of X-ray diffraction analysis and scanning electron microscopy. In work [8] it was shown that fine silicides within α -plates form during the eutectoid transformation and further lowering of silicon solubility in the titanium α -matrix. Work [8] presents the distribution of the main alloying elements in the cast metal of the alloy of Ti–Al–Zr–Sn–Mo–Nb–Si alloying system, from which we can see that alongside titanium, zirconium is also present in the silicides and their interlayers on the grain boundaries, i.e. complex silicides of $(\text{Zr}, \text{Ti})_5\text{Si}_3$ and $(\text{Zr}, \text{Ti})_3\text{Si}$ type form in the alloy. Zirconium and silicon are present both in the solid solution, and in the strengthening silicide phase, which is distributed along the boundaries of former β -grains. In work [9] a conclusion was made that the silicides form not only within the α -plates, but dispersed silicides are also distributed between the α -plates in the form of individual precipitates along the boundaries and inside the α -phase grains. There are quite a lot of silicides in the structure, but they are dispersed, and are distributed between the α -plates and in the form of individual precipitates along the boundaries and inside the α -phase grains [8].

The structure of the metal of the weld middle zone in welded joints of the heat-resistant alloy of Ti–Al–Zr–Sn–Mo–Nb–Si alloying system, produced by electron beam welding, after additional vacuum annealing at 850 °C, is shown in Figure 3.

A typical dendritic structure of the cast metal is formed in the weld zone (Figure 3, *a*). It is dense, and no defects of the type of porosity, cracks or nonmetallic inclusions were found in it. The size of dendrite branches in the cross-sectional section can be tentatively assessed by the difference in etchability of individual regions. It is equal to 100–500 μm . The boundaries of the dendritic regions have no excess phase precipitates and are not the weak points of the material. It is important that rapid cooling of the molten weld metal results in formation of quite dispersed packs of Widmanstätten morphology in the dendritic regions with the pack size (by the size of the largest plates) in the range of 20–50 μm (Figure 3, *b*), that is close to the characteristics of dispersity of the base metal structure. At the same time, comparing the structures of the upper and middle zone of the weld, we can conclude that a more dispersed structure forms in the weld middle, compared to its upper part. The difference, however, is not great, and it can be associated with different temperature-time conditions of weld metal crystallization.

Vacuum annealing at the temperature of 850 °C for 1 h intensified the diffusion processes, which resulted in a certain redistribution of alloying elements in the welded joint structure. Compared to the structure of the welded joint in the state after LHT [13], after vacuum annealing clusters of dispersed particles in the form of chains, as well as monolithic silicide interlay-

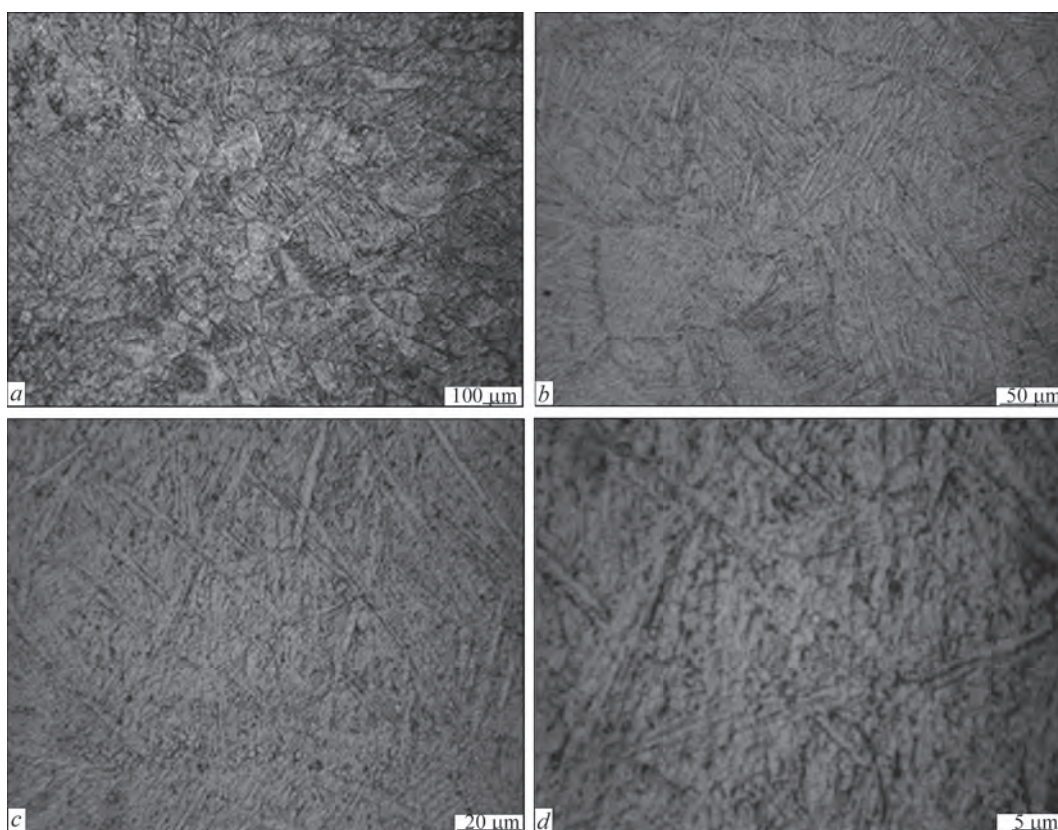


Figure 3. Microstructure of the weld metal of EB welded joint of the heat-resistant alloy of Ti–Al–Zr–Sn–Mo–Nb–Si alloying system after annealing at 850 °C

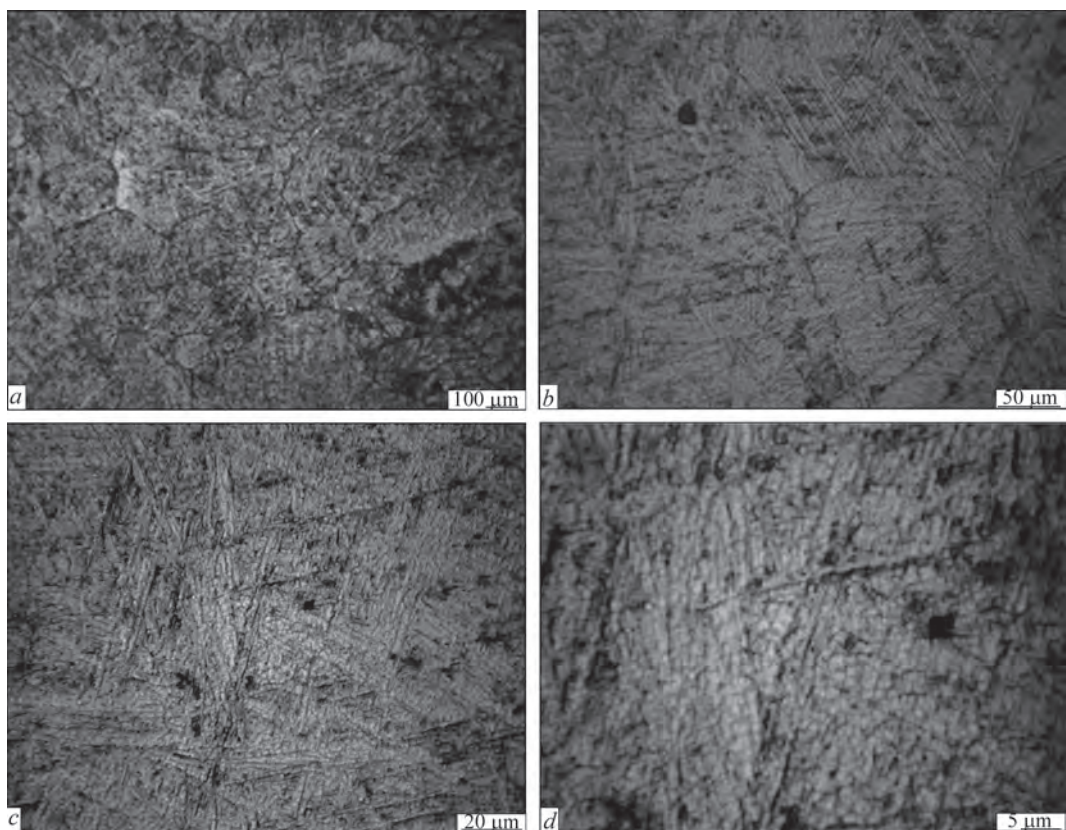


Figure 4. Microstructure of the metal in the fusion zone of EB welded joint of the heat-resistant alloy of Ti–Al–Zr–Sn–Mo–Nb–Si alloying system after annealing at 850 °C

ers up to 7 μm long are recorded on the boundaries of the platelike α -phase (Figure 3, *c, d*).

Microstructure of the fusion zone in the EB welded joint of the heat-resistant alloy of Ti–Al–Zr–Sn–Mo–Nb–Si alloying system, in the state after annealing at 850 °C, is shown in Figure 4.

No significant difference in the morphology or dimensional characteristics of the structural components was found between the samples after LHT [13], and samples annealed in the vacuum at 850 °C. This can be associated with the fact that the temperature of both the treatments did not exceed that of the phase transformation point for this alloy, so that the repeated crystallization processes did not develop, while the processes of recrystallization in the heat-resistant alloy proceed slowly at these temperatures.

The HAZ metal structure in samples of the EB welded joint of the heat-resistant alloy of Ti–Al–Zr–Sn–Mo–Nb–Si alloying system after annealing at 850 °C is shown in Figure 5. Analysis of the microstructure reveals that the HAZ preserves the main morphological and dimensional characteristics of the base metal. No difference in the structure was observed after different heat treatment modes, namely annealing and LHT [13]. During annealing at 850 °C a clearer delineation of the α -phase plates is observed in the structure, due to precipitation of the β -phase along the plate boundaries and there is a possibility of formation of intermetallic particles. In the fusion zone metal not only clusters of dis-

persed particles in the form of chains, but also monolithic silicide interlayers between the plates are recorded on the boundaries of the platelike α -phase as a result of the influence of annealing at 850 °C (Figure 5, *c, d*). Etching of the sections of the welded joint of the alloy of Ti–Al–Zr–Sn–Mo–Nb–Si alloying system was improved, compared to etching of the sections of the welded joint after LHT, as a result of decorating of the plate boundaries by the dispersed particles. The effectiveness of vacuum annealing can be fully evaluated when establishing the mechanical characteristics of the welded joints.

Although application of different modes of heat treatment did not lead to any essential changes in the welded joint microstructure, the difference in the intensity of structure etching and in the quantity of the β -phase on the boundaries of α -phase plates allows us to assume that the mechanical properties of the joints could change under the annealing influence, as a result of relaxation of the mechanical stresses and due to excess phase formation. More over, vacuum annealing at the temperature of 850 °C intensified the running of the diffusion processes, which resulted in a certain redistribution of the alloying elements in the structure of the welded joints proper. Silicon has diffused to a large extent to the boundaries of the platelike α -phase, forming there not only clusters of dispersed particles in the form of chains, but also monolithic silicide interlayers between the plates.

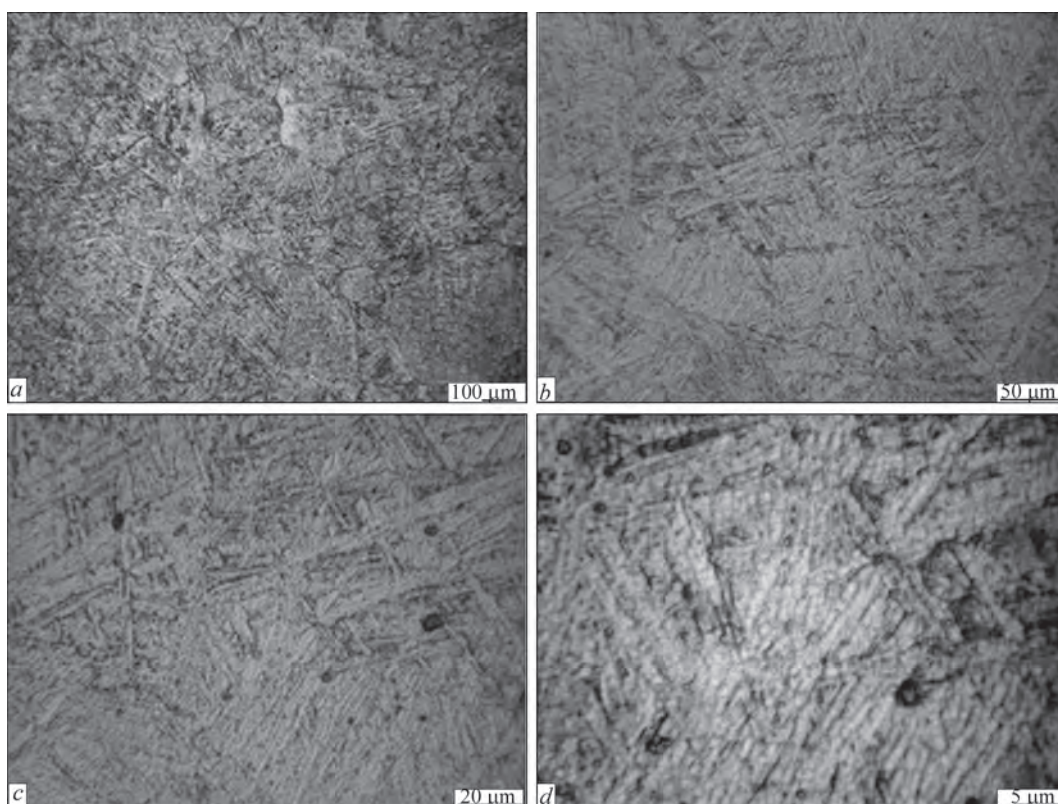


Figure 5. Microstructure of the HAZ metal of the weld in EB welded joint of the heat-resistant alloy of Ti–Al–Zr–Sn–Mo–Nb–Si alloying system after annealing at 850 °C

ANNEALING INFLUENCE ON THE MICROSTRUCTURE OF GTA WELDED JOINTS OF THE HEAT-RESISTANT TITANIUM ALLOY OF Ti–Al–Zr–Sn–Mo–Nb–Si ALLOYING SYSTEM

Weld metal microstructure in the GTA welded joint in the state after annealing at 850 °C for 1 h is shown in Figure 6. Microstructural analysis reveals that the typical dendritic structure of the cast metal formed during welding is preserved in the weld metal after annealing (Figure 6, *a, b*). It is dense and no defects of the type of porosity, cracks or nonmetallic inclusions were found in it. The size of the dendrite branches in the cross-section of the microsection, which can be tentatively assessed by precipitation of α -phase interlayers on the boundaries of the dendritic regions, is equal to 200–300 μm .

As a result of molten metal cooling during welding rather dispersed packs of Widmanstatten morphology are formed in the dendritic regions. In case of application of GTAW with through penetration coarsened packs of the dimensions in the range of 10–30 μm (by the size of the largest plates) form in the weld metal. With lowering of the specific power during welding in the case of GTAW over a layer of flux a reduction in the pack dimensions and increase in the microstructural homogeneity are observed, which should have a positive impact on the welded joint mechanical properties. Subsequent annealing at 850 °C (Figure 6, *c, d*) leads to an even greater refinement of the weld metal

structure due to formation of dispersed precipitates of the β -phase inside the primary packs of α -phase crystals. These precipitates, however, decorate the boundaries of the primary dendrite branches, leading to their more contrast delineation at small magnifications (Figure 6, *b*). The influence of additional precipitation of β -phase crystals on the mechanical properties requires further study. Precipitates of dispersed crystals should have a positive effect on the strength properties, but their precipitation exactly along the dendrite boundaries can facilitate crack propagation. It follows from the analysis that preheating to 400 °C has virtually no effect on the morphology and dimensional parameters of the microstructure (although there is a slight tendency to coarsening), but the structure of the samples, produced using GTAW with a lower specific power with preheating to 400 °C, is characterized by a more complete precipitation of the β -phase during weld metal crystallization.

Metal structure in the fusion zone of samples produced by GTAW over a layer of flux with lower energy input values in the state after annealing at 850 °C for 1 h, is shown in Figure 7. Dependence of the fusion zone microstructure on GTAW technological scheme is similar to the one observed during analysis of the weld structure. The fusion zone metal is dense and no defects of the type of porosity, cracks or nonmetallic inclusions were found in it. Quite dispersed packs of ($\alpha+\beta$)-Widmanstatten morphology are formed in the weld metal in the dendritic regions (Figure 7, *a*). The dimensions of

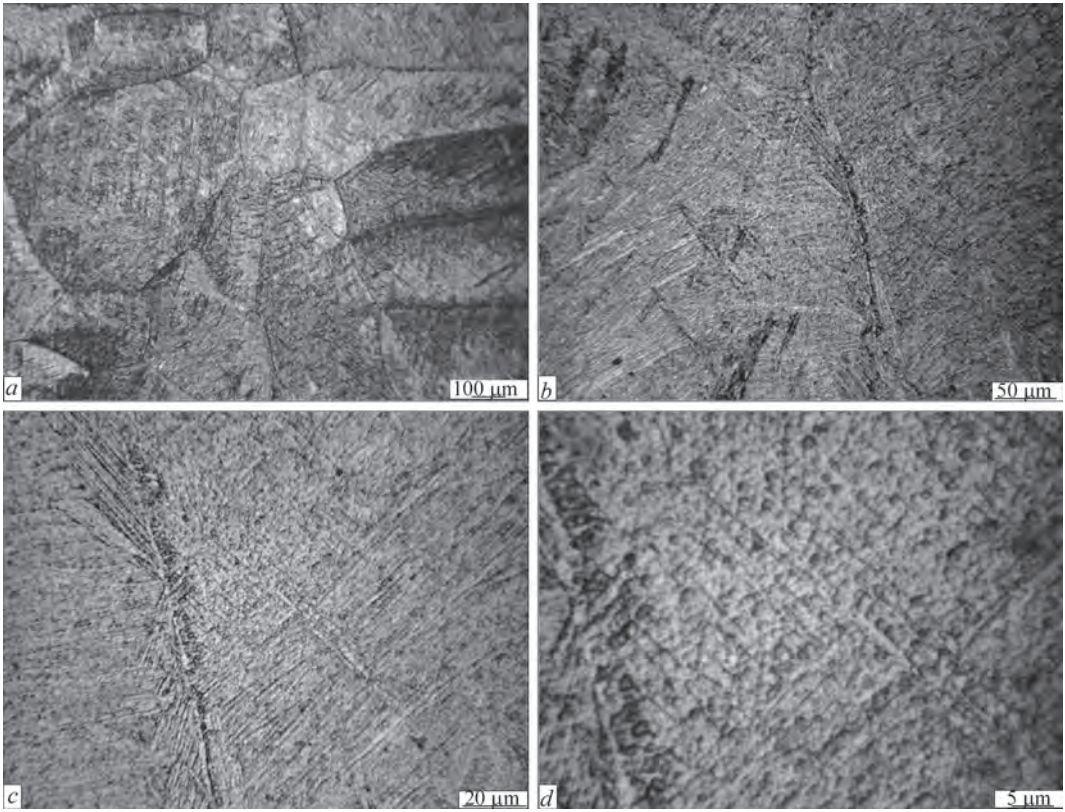


Figure 6. Microstructure of the weld metal of GTA welded joint of the heat-resistant titanium alloy of Ti–Al–Zr–Sn–Mo–Nb–Si alloying system after annealing at 850 °C

the dispersed ($\alpha+\beta$)-Widmanstatten packs by the largest plate size are equal to 10–30 μm . At lowering of the specific power in welding a reduction in the pack

dimensions and an increase in the homogeneity of the microstructure are observed, that should have a positive effect on the welded joint mechanical properties.

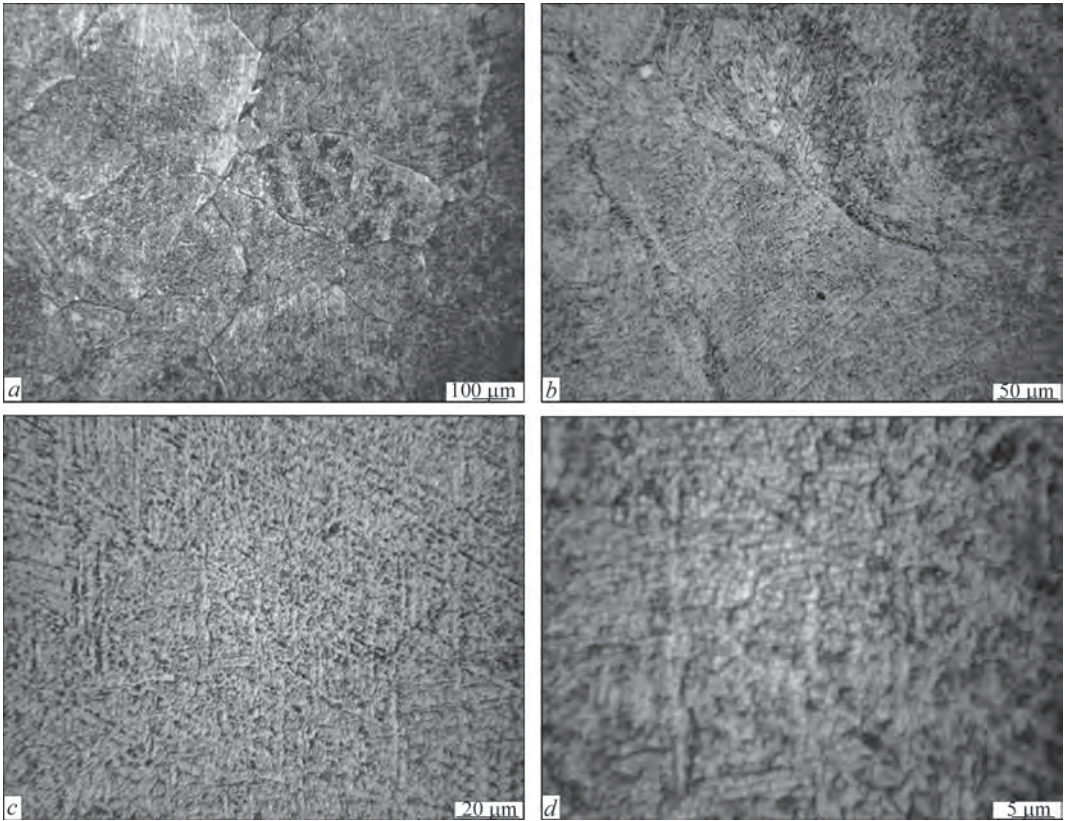


Figure 7. Microstructure of the fusion zone metal in GTA welded joint of the heat-resistant titanium alloy of Ti–Al–Zr–Sn–Mo–Nb–Si alloying system after annealing at 850 °C

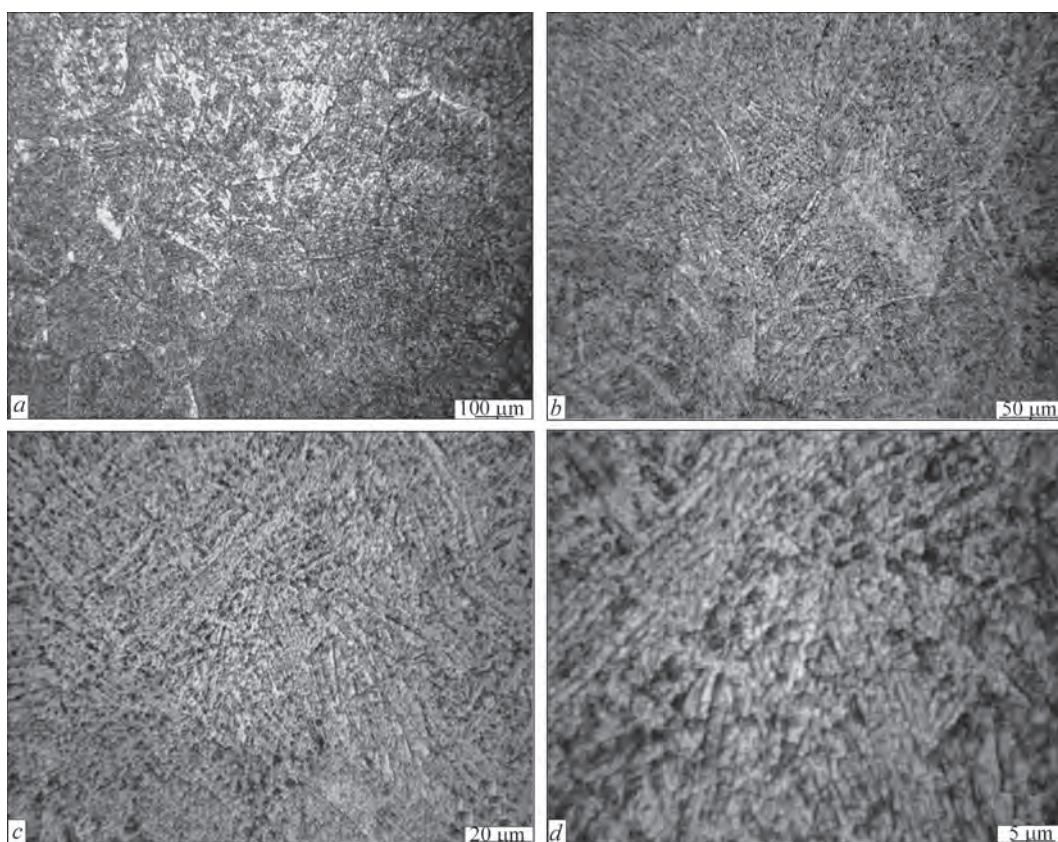


Figure 8. Microstructure of the HAZ metal in GTA welded joint of the heat-resistant titanium alloy of Ti–Al–Zr–Sn–Mo–Nb–Si alloying system after annealing at 850 °C

Welding with a lower level of specific power and subsequent annealing at 850 °C (Figure 7, *a–c*) leads to an even greater refinement of the weld metal structure due to formation of dispersed β -phase precipitates inside the primary packs of α -phase crystals (Figure 7, *d*). These precipitates also decorate the boundaries of the primary dendrite branches, leading to their more contrast delineation at small magnifications (Figure 7, *c*). Additional precipitation of β -phase crystals can influence the mechanical properties.

Dependence of the HAZ microstructure on GTAW technological scheme practically coincides with the regularities revealed during analysis of the structure of the fusion zone metal. At lowering of the specific power in welding due to application of GTAW over a layer of flux (Figure 8, *a, b*) the HAZ metal preserves the finely dispersed structure of basket weave type, which should have a positive effect on the welded joint mechanical properties.

Welding with a lower level of specific power and subsequent annealing at 850 °C (Figure 8, *a, b, d*) leads to an even greater refinement of the weld metal structure, due to formation of dispersed precipitates of β -phase inside the primary packs of α -phase crystals. As no liquid phase formed in the HAZ, the effect of decorating the boundaries of primary dendrite branches is absent, so that the influence of additional precipitation of β -phase crystals on the mechanical

properties in this case, should be favourable for the alloy mechanical properties.

Comparing the welded joint regions, namely base metal, weld metal, fusion zone metal and HAZ metal, we should note the similarity of metal microstructure in different welded joint zones after the influence of furnace annealing.

MECHANICAL PROPERTIES OF WELDED JOINTS OF HEAT-RESISTANT PSEUDO- α -TITANIUM ALLOY OF Ti–Al–Zr–Sn–Mo–Nb–Si ALLOYING SYSTEM AFTER ANNEALING

Determination of the mechanical properties of EB welded joints of heat-resistant pseudo- α -titanium alloy of Ti–Al–Zr–Sn–Mo–Nb–Si alloying system in as-annealed state led to the conclusion that after the influence of annealing the strength values of the welded joints somewhat decreased and are at the level of 980 MPa (Table 3). It should be noted that the impact toughness values of the welded joints are also at a high level of 17.9 J/cm². The values of impact toughness (*KCV*) after annealing increased for all the welded joints.

Comparison of the quality coefficients for the EB welded joints lead to the conclusion that LHT application allows obtaining a higher set of mechanical characteristics ($K_{wm} = 1.126$), compared to EBW without the LHT, while annealing application allowed increasing the values of mechanical characteristics of

Table 3. Mechanical properties of EB and GTA welded joints of the heat-resistant titanium pseudo- α -alloy of Ti–Al–Zr–Sn–Mo–Nb–Si alloying system

Sample	σ_t	σ_{02}	δ_s , %	KCV , J/cm ²	K_{wm}	K_s
	MPa					
Base metal after annealing	1028	996	2.7	14	–	–
EB welded joint	996	901	–	12.3	0.919	0.96
EB welded joint with LHT at 750 °C	1041	1012	–	17.4	1.126	1.01
EB welded joint, mode 2 after annealing	980	899	–	17.9	1.1157	0.953
GTA welded joint	969	890	11.2	8.9	0.787	0.94
GTA welded joint after annealing	995	908	–	9.7	0.829	0.967

an EB joint without LHT application to the level of those of EB joints with LHT.

Comparison of the quality coefficients for GTA welded joints leads to the conclusion that annealing application allowed obtaining the strength values of GTA joints at the level of those of EB welded joints.

Comparison of the quality coefficients for the welded joints produced by EBW and GTAW leads to the conclusion about a higher complex of mechanical characteristics of EB joints, both after welding and after annealing.

DISCUSSION OF THE RESULTS

Pseudo- α -alloys, to which the experimental heat-resistant titanium alloy also belongs, have a number of important advantages compared to the heat-resistant titanium alloys of other classes, which are particularly important for the welded joints. The quantity of the β -phase in the experimental alloy is such ($K_\beta < 0.2$) that it should have all the main properties and advantages of single-phase α -alloys, and also have positive properties, which distinguish the alloys of this class from α -alloys. The martensite α' -phase, forming at cooling from the temperatures above the critical one, is close to the α -phase by its physical and mechanical properties. The quantity of the β -phase in the experimental alloy is so small that its eutectoid decomposition, even if it takes place, cannot lead to any noticeable deterioration of the physical-mechanical properties. Due to that the structural pseudo- α -alloys feature good weldability and high thermal stability, inherent to α -alloys. Addition of small amounts of β -stabilizing elements above their solubility in α -titanium, in connection with heteronization of the structure, results in a significant increase of the strength and heat-resistance at moderate temperatures, without any noticeable lowering of their ductility, or even in an increase in their technological ductility. Pseudo- α -alloys practically do not lend themselves to strengthening heat treatment which is highly important for the welded joints, as in the HAZ, which is adjacent to the weld, unfavourable combinations of temperatures and cooling rates almost always arise, which may lead to brittleness, for instance two-phase titanium. Studies of the heat-resistant pseudo- α -titanium alloy showed that the microstructure in different regions of the welded joints is identical, and it is similar for differ-

ent methods and modes of welding and heat treatment. It can be assumed that the metal phase composition in different regions of the welded joints will not have any marked differences. The change in the welding heat input makes a greater contribution to the joint structure. So, at application of GTAW with through penetration coarsened packs are formed with the dimensions (by the largest plate size) in the range of 10–30 μm . At lowering of the specific power a reduction in the pack dimensions and an increase in the microstructure homogeneity are observed, which should have a positive effect on the welded joint mechanical properties.

Thus, in GTAW with a lower linear power a fine highly homogeneous structure is formed, which potentially can have higher mechanical characteristics. Application of vacuum annealing to the welded joints of the heat-resistant pseudo- α -titanium alloy of Ti–Al–Zr–Sn–Mo–Nb–Si alloying system, produced by the technology of GTAW with a lower linear power, allows additional refinement of the structure, having a positive effect on the mechanical characteristics. However, the tendency to β -phase precipitation on the dendrite boundaries in the weld metal zone can potentially facilitate crack propagation. At EBW annealing also leads to structure refinement and silicon redistribution with formation of monolithic silicide interlayers between the plates.

After the annealing influence, the strength values of EB welded joints somewhat decreased, and impact toughness (KCV) values increased after annealing for all the welded joints. Note that the strength values of all the welded joints are higher than 0.95 of base metal strength.

CONCLUSIONS

1. It is shown that annealing results in the formation of a finer structure in the metal of EB welded joints of the heat-resistant pseudo- α -titanium alloy of Ti–Al–Zr–Sn–Mo–Nb–Si alloying system with precipitates of dispersed silicide particles in the form of chains and monolithic silicide interlayers up to 7 μm long between the plates. Such a structure ensures the strength values of the welded joints at the level of 980 MPa, which is equal to 95 % of base metal strength, and the impact toughness values of the welded joints in as-annealed state are at a high level of 17.9 J/cm².

2. It is established that application of annealing after GTA welding of the heat-resistant pseudo- α -titanium alloy of Ti–Al–Zr–Sn–Mo–Nb–Si alloying system leads to refinement of the welded joint microstructure, reduction of the dimensions of dispersed (α + β)-Widmanstätten packs to 10–30 μm , and to an increase in the impact toughness (*KCV*) values.

3. Comparison of the quality coefficients for EB and GTA welded joints leads to the conclusion about a higher complex of mechanical characteristics of the EB joints, both after welding and after annealing. Annealing application allowed raising the values of mechanical characteristics for EB joints without LHT application to the level of characteristics of EB joints with LHT.

REFERENCES

- (2003) *Titanium and titanium alloys. Fundamentals and applications*. Ed. by Leyens, M. Peters. Weinheim, WILEY-VCH Verlag GmbH & Co, KGaA.
- Ertuan Zhao, Shichen Sun, Yu Zhang (2021) Recent advances in silicon containing high temperature titanium alloys. *J. of Materials Research and Technology*, **14**, 3029–3042. DOI: <https://doi.org/10.1016/j.jmrt.2021.08.11>
- Firstov, S.O., Kulak, L.D., Kuzmenko, M.M., Shevchenko, O.M. (2018) The Ti–Al–Zr–Si alloys for the exploitation at high temperatures. *Materials Sci.*, **54**(6), 30–35. DOI: <http://jnas.nbuv.gov.ua/article/UJRN-0000958917>
- Shichen Sun, Hongze Fang, Yili Li et al. (2023) Formation mechanism and effect on the mechanical properties of TiSi phase for Ti–5Al–5Mo–5Cr–3Nb–2Zr alloyed by silicon. *J. Alloys and Compd.*, **938**(25), 168510. DOI: <https://doi.org/10.1016/j.jallcom.2022.168510>
- Hong Feng, Shuzhi Zhang, Fan Peng et al. (2023) Enhanced mechanical properties of a near- α titanium alloy by tailoring the silicide precipitation behavior through severe plastic deformation. *Materials Sci. and Eng.*, **880**(26), 145356. DOI: <https://doi.org/10.1016/j.msea.2023.145356>
- Wu, T., Beaven, P., Wagner, R. (1990) The Ti_3 (Al, Si) + Ti_2 (Si, Al)₃ eutectic reaction in the Ti–Al–Si system. *Scripta Metallurgica*, **24**, 207–212. DOI: [https://doi.org/10.1016/0956-716X\(90\)90593-6](https://doi.org/10.1016/0956-716X(90)90593-6)
- Hayat, M.D., Singh, H., He, Z., Cao, P. (2019) Titanium metal matrix composites: An overview. *Composites, Pt A*, **121**418–121438, DOI: <https://doi.org/10.1016/j.compositesa.2019.04.005>
- Akhonin, S.V., Berezos, V.O., Pikulin, O.M. et al. (2022) Producing high-temperature titanium alloys of Ti–Al–Zr–Si–Mo–Nb–Sn system by electron beam melting. *Suchasna Elektrometalurgiya*, **2**, 3–9. DOI: <http://doi.org/10.37434/sem2022.02.01>
- Akhonin, S.V., Severin, A.Yu., Pikulin, O.M. et al. (2022) Structure and mechanical properties of high-temperature titanium alloy of Ti–Al–Zr–Si–Mo–Nb–Sn system after deformation treatment. *Suchasna Elektrometalurgiya*, **4**, 43–48. DOI: <http://doi.org/10.37434/sem2022.04.07>
- Longchao Zhuo, Kaile Ji, Jinwen Lu et al. (2023) Microstructure characterization and tensile performance of a high-strength titanium alloy with in-situ precipitates of Ti_5Si_3 . *J. Alloys and Compd.*, **968**(15), 171867. DOI: <https://doi.org/10.1016/j.jallcom.2023.171867>
- Akhonin, S.V., Vrzhyzhevsky, E.L., Belous, V.Yu., Petrichenko, I.K. (2017) Influence of preheating parameters and local heat treatment on structure and properties of dispersion-strengthened joints of silicon-containing titanium alloys made by electron beam welding. *The Paton Welding J.*, **7**, 43–47. DOI: <https://doi.org/10.15407/tpwj2017.07.09>
- Li, Y., Wang, H., Han, K. et al. (2017) Microstructure of Ti–45Al–8.5Nb–0.2W–0.03Y electron beam welding joints. *J. of Materials Proc. Technology*, **250**, 401–409. DOI: <https://doi.org/10.1016/j.jmatprotec.2017.07.004>
- Akhonin, S.V., Bilous, V.Yu., Vrzhyzhevskiy, E.L. et al. (2024) Structure and properties of welded joints of heat-resistant titanium alloy of the system Ti–Al–Zr–Sn–Mo–Nb–Si produced by EBW. *Suchasna Elektrometalurgiya*, **4**, 29–40. DOI: <https://doi.org/10.37434/sem2024.04.05>
- Akhonin, S.V., Bilous, V.Yu., Selin, R.V. et al. (2023) Mechanical characteristics of welded joints of high-strength titanium alloys produced by various welding methods. *Suchasna Elektrometalurgiya*, **4**, 44–53. DOI: <https://doi.org/10.37434/sem2023.04.06>
- Severyn, A.Yu., Bilous, V.Yu., Radchenko, L.M. et al. (2025) Study of the temperatures of phase transformation of heat-resistant titanium alloy of Ti–Al–Zr–Si–Mo–Nb–Sn alloying system. *Suchasna Elektrometalurgiya*, **1**, 40–44. DOI: <https://doi.org/10.37434/sem2025.01.07>

ORCID

S.V. Akhonin: 0000-0002-7746-2946,
V.Yu. Bilous: 0000-0002-0082-8030,
V.V. Pashynskiy: 0000-0003-0118-4748,
R.V. Selin: 0000-0002-2990-1131,
A.Iu. Severin: 0000-0003-4768-2363,
E.L. Vrzhyzhevskiy: 0000-0001-8651-8510

CONFLICT OF INTEREST

The Authors declare no conflict of interest

CORRESPONDING AUTHOR

V.Yu. Bilous

E.O. Paton Electric Welding Institute of the NASU
11 Kazymyr Malevych Str., 03150, Kyiv, Ukraine.

E-mail: belousvy@gmail.com

SUGGESTED CITATION

S.V. Akhonin, V.Yu. Bilous, V.V. Pashynskiy, R.V. Selin, A.Iu. Severin, E.L. Vrzhyzhevskiy (2025) The effect of annealing on the structure and properties of welded joints of heat-resistant pseudo- α -titanium alloy Ti–Al–Zr–Sn–Mo–Nb–Si alloying system. *The Paton Welding J.*, **6**, 36–45. DOI: <https://doi.org/10.37434/tpwj2025.06.06>

JOURNAL HOME PAGE

<https://patonpublishinghouse.com/eng/journals/tpwj>

Received: 27.03.2025

Received in revised form: 07.05.2025

Accepted: 27.06.2025

INFLUENCE OF WELDING THERMAL CYCLES ON THE STRUCTURE AND HARDNESS OF THE METAL IN THE HAZ OVERHEATING AREA IN WELDED JOINTS OF MEDIUM-CARBON ALLOY STEELS OF HIGH HARDNESS

V.D. Poznyakov, O.V. Korieniev

E.O. Paton Electric Welding Institute of the NASU
11 Kazymyr Malevych Str., 03150, Kyiv, Ukraine

ABSTRACT

During welding, two characteristic areas are formed in the heat-affected zone of welded joints of medium-carbon alloy steels with hardened (high-temperature area) and tempered (low-temperature area) metal. Since the metal of the high-temperature area of the HAZ is heated above the temperature A_{c1} (approximately 730 °C), the initial structure in it is transformed into austenite, which upon cooling decomposes with the formation of other structures, from ferritic to martensitic. Accordingly, the mechanical properties of the metal also change. The formation of a particular structure in the cooled metal depends on the chemical composition of the material and the degree of its supercooling. This paper presents data on the influence of welding thermal cycles on the structure and mechanical properties of the metal in the HAZ overheating area in welded joints of medium-carbon alloy steels of different chemical composition.

KEYWORDS: medium-carbon alloy steels, high hardness, welding thermal cycle, metal structure, mechanical properties, welded joints

INTRODUCTION

Throughout the world, heat-strengthened medium-carbon alloy steels of high hardness (HV — over 5000 MPa) and strength (σ_t — more than 1400 MPa) are widely used in the manufacture of metal structures for special machines and individual, particularly loaded assemblies of mining and processing equipment. Such steels acquire high hardness and strength, combined with the necessary toughness properties by alloying with manganese, silicon, chromium, molybdenum, nickel, microalloying with boron, titanium, aluminium, vanadium, etc., as well as by heat treatment, which involves quenching of steel and then low-temperature tempering [1–8].

Most products that use high-hardness steels are welded. Individual parts and assemblies in such products are joined together using arc welding processes. This process involves heating of a rolled steel to temperatures exceeding A_{c1} temperature (approximately 730 °C) in some HAZ areas and reach 1300 °C in the area in direct contact with the weld (high-temperature areas of the HAZ in welded joints).

It should be noted that a high-temperature HAZ area includes areas of overheating (temperature ranges from 1100–1500 °C), normalization (temperature ranges from 930–1100 °C) and partial recrystallization (temperature ranges from 720–930 °C). When these areas are heated in the metal, the primary structure transforms into austenite. During cooling, austenite

decomposes forming other structural components. The type of a formed structure depends on the chemical composition of steels and the degree of supercooling. Accordingly, mechanical properties (hardness, strength, ductility, and impact toughness) of the metal with the newly formed structures change [9–11]. Taking this fact into account, the aim of this paper is to present the results of laboratory studies on the influence of welding thermal cycles on the structure and mechanical properties of the metal in the HAZ overheating area in welded joints of different chemical composition of medium-carbon alloy steels.

RESEARCH METHODS

The studies were carried out on medium-carbon alloy steels, the maximum requirements for the concentration of alloying elements and chemical composition of which are given in Table 1.

The influence of welding thermal cycles on the structural transformations of the metal in the HAZ overheating area was studied using model specimens that were heated and cooled through the thermal cycles typical of arc welding processes.

The welding thermal cycle was recorded using a chromel-alumel thermocouple with a diameter of 0.5 mm.

To simulate the welding thermal cycles, the research complex Gleeble 3800 equipped with a high-speed dilatometer was used, which allowed detecting the temperature interval, in which structural and phase transformations in the metal start and end.

Table 1. Requirements for the chemical composition of the studied steels and mass fraction of alloying elements in them, wt.%

Steel grade		C	Si	Mn	Cr	Ni
1	Requirements	0.29–0.36	1.2–1.5	0.60–1.00	1.50–2.00	2.00–2.40
	Actual	0.32	1.2	0.70	1.80	2.20
2	Requirements	≤0.32	≤0.4	≤1.20	≤1.00	≤1.80
	Actual	0.23	0.25	0.84	0.50	0.97

Table 1 (Cont.)

Steel grade		Mo	B	V	Ti	S	P
1	Requirements	0.45–0.55	–	0.18–0.25	0.005–0.025	≤0.003	≤0.012
	Actual	0.50	–	0.20	0.024	0.008	0.011
2	Requirements	≤0.70	≤0.005	–	–	≤0.010	≤0.015
	Actual	0.33	0.002	–	–	0.004	0.013

Rigidly fixed specimens were studied, that were continuously heated and cooled in a manner similar to the thermal cycles typical of arc welding processes. The specimens were heated by a current passing through the specimen at a rate of 210 °C/s (heating time 6 s) to a temperature of 1250 °C. The cooling intensity of the specimens was adjusted so that in the temperature range of 600–500 °C, the cooling rate ($W_{6/5}$) varied from 2.5 to 30.0 °C/s. More details of this procedure and the requirements for model specimens are described in [12]. The final identification of the final structure formed as a result of the thermal cycle effect on the metal was revealed on the basis of metallographic examinations. The ratio of the phases formed as a result of transformations was determined by the segment method.

Metallographic examinations were performed using the Neophot-32 microscope; the microhardness of individual structural components and the integrated hardness of the metal were measured in the LECO M-400 hardness tester at loads of 100 g ($HV_{0.1}$) and 10 kg (HV_{10}), respectively. The specimens were prepared for studies according to the standard method using diamond pastes of different dispersion, and the microstructure was revealed by chemical etching in a 4 % alcohol solution of nitric acid.

The microhardness (HV), strength ($\sigma_{0.2}$ and σ_l), ductility (δ_5) and impact toughness (KCU_{20}) of the HAZ metal were evaluated by the results of testing standard specimens made from model specimens heated by the current passing through the specimen. The specimens were continuously heated and cooled through the thermal cycles of arc welding processes. The model specimens of 12×12×120 mm, from which standard specimens for tensile and impact toughness tests were made, were heated using the MRS-75 equipment. The cooling rate of the specimens was regulated by blowing them with air at different intensities.

RESEARCH RESULTS AND DISCUSSION

Metallographic examinations have established that the structure of the base metal of steel 1 was identified as martensite, which has a microhardness $HV_{0.1} = 4680–5020$ MPa (Figure 1, *a*).

The transformation of supercooled austenite in the metal in the HAZ overheating area of steel grade 1, regardless of its cooling rate, occurs exclusively in the martensitic area. The cooling rate of the metal affects the structure parameters. As the cooling rate grows, the structure becomes finer. This is evidenced by the fact that the size of martensite packets in the metal in the HAZ overheating area decreases from approximately 40 μm at $W_{6/5} = 2.5$ °C/s to 12 μm at $W_{6/5} = 30$ °C/s. The cooling rate of the metal in the HAZ overheating area also affects its microhardness (Table 2). Thus, at $W_{6/5} = 2.5$ °C/s, it is in the range of 4510–4600 MPa, and at $W_{6/5} = 30$ °C/s it is approximately 5510 MPa.

The structure of the base metal of steel 2 represents a mixture of bainite and martensite with a pronounced rolled texture (Figure 2, *a*). The hardness of the base metal is $HV_{0.1} = 4770$ MPa.

Examinations of the metal structure of steel 2 specimens, which were continuously heated and cooled through the welding thermal cycles, revealed the following. At a cooling rate of $W_{6/5} = 1$ °C/s, the structure of the simulated HAZ metal is bainitic-martensitic (B–M) with a microhardness $HV_{0.1} = 3210–3860$ MPa (bainitic component) and $HV_{0.1}$ approximately ≈ 4730 MPa (martensitic component) (Figure 2, *b*). The size of martensite packets (D_p) is in the range of 120–240 μm.

At higher cooling rates ($W_{6/5} > 3$ °C/s), an exclusively martensitic structure is formed in the metal in the HAZ overheating area of steel 2 (Figure 2, *c*, *d*). Its microhardness increases from 5090 to 5490 MPa as the metal cooling intensity grows. At the same time,

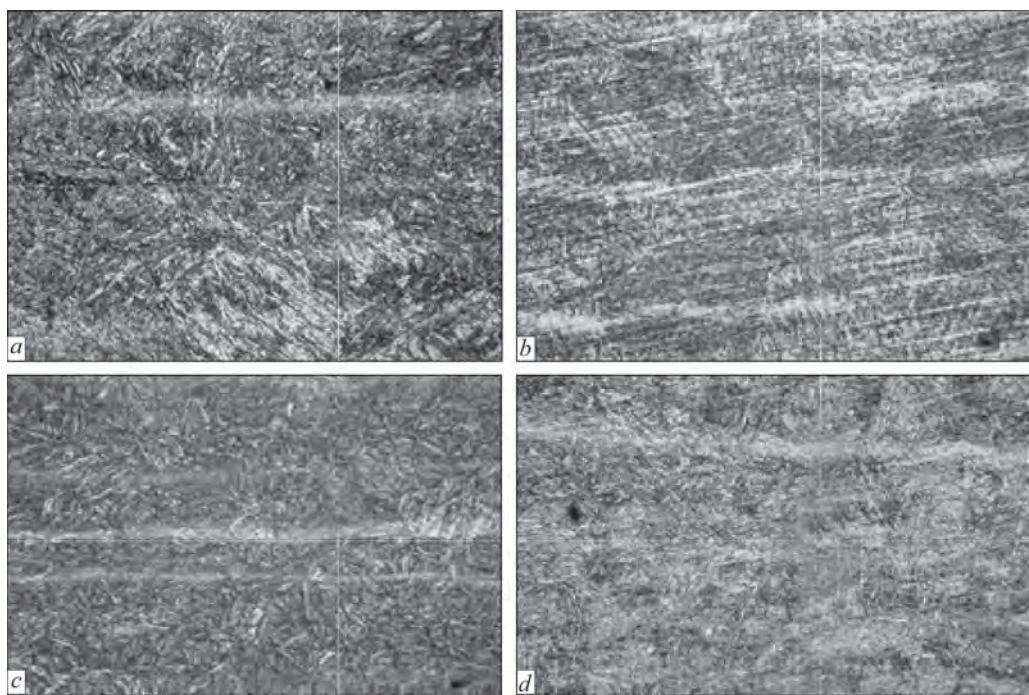


Figure 1. Structure of the base metal (*a*) and metal in the HAZ overheating area (*b–d*) of steel 1: *b* — 2.5; *c* — 10.0; *d* — 30 °C/s

Table 2. Microhardness of the base metal and metal in the HAZ overheating area of steel 1

$W_{6/5}$ °C/s	Base metal	2.5	5.0	10.0	15.0	30.0
Structure	M	M	M	M	M	M
$HV_{0.1}$, MPa	4680–5020	4200–4950	5100–5150	5050–5350	5150–5350	5150–5350

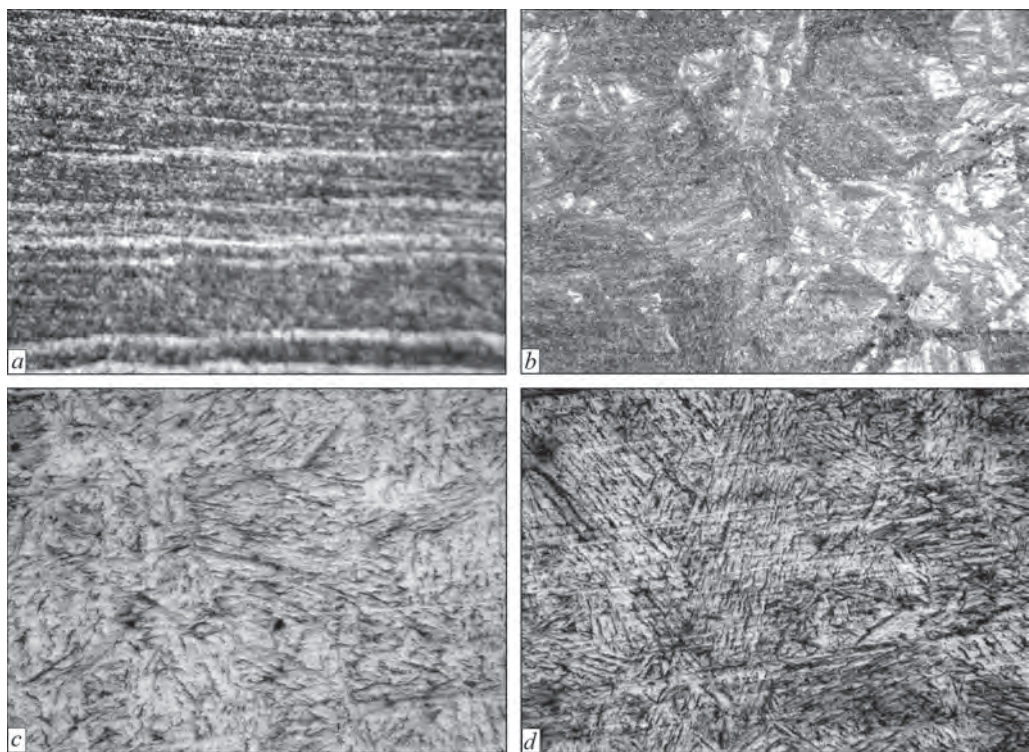


Figure 2. Structure of the base metal (*a*) and metal in the HAZ overheating area of steel 1 cooled at the following rates: *b* — 1.0; *c* — 10.0; *d* — 30 °C/s

Table 3. Microhardness of the base metal and metal in the HAZ overheating area of steel 2

$W_{6/5}, ^\circ\text{C/s}$	Base metal	1	3	5	10	20
Structure	M	B+M	M	M	M	M
$HV_{0.1}, \text{MPa}$	4700–4900	2950–3850 (B) 4150–4550 (M)	4200–4950	5100–5150	5150–5350	5150–5350

Table 4. Mechanical properties of the metal in the HAZ overheating area of the studied medium-carbon alloy steels

Steel grade	$W_{6/5}, ^\circ\text{C/s}$	HV	$\sigma_{0.2}$	σ_t	δ_5	φ	$KCU, \text{J/cm}^2$
		MPa			%		
1	0	5400	1460	1780	11.1	58.6	80.0
	5	4370	1262	1490	12.7	55.0	62.1
	10	4920	1395	1615	12.1	53.6	58.0
	15	5200	1445	1705	11.2	48.3	54.6
	20	5500	1502	1805	10.6	47.3	48.7
	30	5710	1607	1896	10.4	46.8	44.3
2	0	5100	1432	1670	7.6	55.0	127.0
	5	4200	1158	1327	8.5	45.0	72.0
	10	4930	1409	1637	7.2	28.8	56.0
	20	5150	1435	1692	7.0	25.9	52.0

martensite packets are also refined. As the cooling rate grows, their sizes decrease from $D_p = 100\text{--}150 \mu\text{m}$ at $W_{6/5} = 3 ^\circ\text{C/s}$ to $D_p = 50\text{--}70 \mu\text{m}$ at $W_{6/5} = 20 ^\circ\text{C/s}$. The microhardness values characteristic of the metal of the studied steels and the cooling conditions of the specimens are given in Table 3.

The results of studies on the influence of the cooling rate of the HAZ overheating area on the mechanical properties of the metal are given in Table 4. They show that, despite the fact that the studied steels contain different amounts of alloying elements, their concentration in steel 1 is higher, and due to heat treatment, they acquire almost the same hardness, approximately $HV 4850\text{--}4860 \text{ MPa}$. Nevertheless, the strength and ductility of these steels is somewhat different. Steel 1 has the highest values. As for the impact toughness of steels, it can be noted that steel 2 will have a better ability to resist dynamic loads.

As noted above, structural changes occurring in the metal under the influence of welding thermal cycles also cause certain changes in the mechanical properties of the overheated HAZ metal in welded joints of the studied steels.

As for the metal strength indices, despite the differences in the absolute values of $\sigma_{0.2}$ and σ_t , which are higher in steel 1, the same tendency is observed for both steels in terms of the influence of metal cooling conditions on these indices. At a cooling rate $W_{6/5} < 5.0 ^\circ\text{C/s}$, the strength of the HAZ metal in relation to the base metal decreases by 15–20 %. In the range of cooling rates $10.0 \leq W_{6/5} \leq 15.0 ^\circ\text{C/s}$, this dif-

ference becomes much smaller and at $W_{6/5} \geq 20.0 ^\circ\text{C/s}$ reaches the strength of the base metal.

Despite the fact that the HAZ metal strength of the studied steels is lower in steel 2, its ductile properties (δ_5), regardless of the metal cooling rate, are worse than in steel 1. This is probably predetermined by different conditions of heat treatment of steels. Taking into account that the concentration of alloying elements in steel 2 is lower than in steel 1, it is obvious, that to ensure high hardness of this steel, its heat treatment conditions were more rigid.

As for the impact toughness of steel, in the initial state it is significantly, almost 1.5 times higher than that of less alloyed steel 2. However, as a result of high-temperature heating during the welding thermal cycle, the KCU values of the metal in the HAZ overheating area almost level and tend to decrease monotonically as the metal cooling intensity grows.

CONCLUSIONS

The results of studies on the influence of welding thermal cycles on the mechanical properties of the metal in the HAZ overheating area in welded joints of different chemical composition of medium-carbon alloy high hardness steels ($HB 500$) showed the following.

1. As a result of heat treatment of medium-carbon alloy steels of high hardness ($HB 500$) according to conditions typical of arc welding process, a martensitic structure is formed in the metal in the HAZ overheating area, the dispersion of which grows with an increase in the metal cooling rate.

2. The high hardness of the metal, which is acquired due to heat treatment of steel during rolled production, can be reduced as a result of its heating through the thermal cycles typical of arc welding. It has the most significant manifestation in the metal cooled at $W_{6/5} \leq 5.0$ °C/s. The lower the concentration of alloying and microalloying elements in steel, the lower the metal hardness.

3. At a cooling rate $W_{6/5} \leq 5.0$ °C/s, the strength of the HAZ metal in relation to the base metal decreases by 15–20 %. In the range of cooling rates $10.0 \leq W_{6/5} \leq 15.0$ °C/s, this difference becomes much smaller and at $W_{6/5} \geq 20.0$ °C/s reaches the strength of the base metal.

4. The impact toughness of less alloyed steel is almost 1.5 times higher than that of steel containing a higher concentration of alloying and microalloying elements. However, as a result of high-temperature heating during the welding thermal cycle, the *KCU* values of the metal in the HAZ overheating area almost level and tend to decrease monotonically as the metal cooling rate grows.

REFERENCES

1. Tekin, Ö. (2020) Mechanical & microstructural analysis of armor steel welded joints. *Inter. J. of Engineering Research and Development UMAGD*, 12(1), 166–175.
2. Łukasz Konat ID, Beata Białobrzaska, Bialek P. (2017) *Effect of welding process on microstructural and mechanical characteristics of Hardox 600 steel*. DOI: <http://dx.doi.org/10.3390/met7090349>
3. Gaivoronskyi, O.A., Poznyakov, V.D., Zavdoveyev, A.V. et al. (2023) Prevention of cold cracking in armour steel welding. *The Paton Welding J.*, 5, 3–10. DOI: <https://doi.org/10.37434/tpwj2023.05.01>
4. Oskwarek, M. (2006) Structural features and susceptibility to cracking of welded joints of Hardox 400 and Hardox 500 steels. In: *Proc. of the IV Students' Sci. Conf. on Human-Civilisation-Future*, Wroclaw, Poland, 22–24 May 2006, Vol. 2, 115–120.
5. Cabrilo, A., Geric, K. (2016) Weldability of high hardness armor steel. *Advanced Materials Research*, 1138, 79–84.
6. Kuzmnikova, L. (2013) An investigation of the weldability of high hardness armor steel. *Wollongong Australia*, 17–234.
7. Shchudro, A., Laukhin, D., Pozniakov, V. (2020) Analysis of the effects of welding conditions on the formation of the structure of welded joints of low-carbon low-alloy steels. *Key Eng. Materials. Switzerland*, 844, 146–154. DOI: <https://doi.org/10.4028/www.scientific.net/KEM.844.146>
8. Maksimov, S.Yu., Prilipko, O.O., Berdnikova, O.M. et al. (2021) Controlling the parameters of the metal crystal lattice of the welded joints made underwater. *Metallofiz. Noveishie Tekhnol.*, 43(5), 713–723 [in Ukrainian]. DOI: <https://doi.org/10.15407/mfint.43.05.0713>
9. Pozniakov, V.D., Gaivoronskyi, A.A., Kostin, V.A. (2017) Features of austenite transformation and mechanical properties of the metal in the zone of thermal influence of 71 grade steel joints during arc welding. *Mehanika ta Mashynobuduvannya*, 1, 254–260.
10. Zavdoveev, A., Poznyakov, V., Baudin, T. et al. (2021) Effect of nutritional values on the processing properties and microstructure of HSLA rod processed by different technologies. *Materials Today Communications*, 28, 102598.
11. Özdemir, T. (2020) Mechanical & Microstructural analysis of armor steel welded joints. *Inter. J. of Eng. Research and Development*, 12(1), 166–175.
12. Grigorenko, G.M., Kostin, V.A. Orlovsky, V.Yu. (2008) Current capabilities of simulation of austenite transformation in low-alloyed steel welds. *The Paton Welding J.*, 3, 31–34.

ORCID

V.D. Poznyakov: 0000-0001-8581-3526,

O.V. Korieniev: 0009-0007-3533-1247

CONFLICT OF INTEREST

The Authors declare no conflict of interest

CORRESPONDING AUTHOR

V.D. Poznyakov

E.O. Paton Electric Welding Institute of the NASU
11 Kazymyr Malevych Str., 03150, Kyiv, Ukraine.

E-mail: pozniakovvd@ukr.net

SUGGESTED CITATION

V.D. Poznyakov, O.V. Korieniev (2025) Influence of welding thermal cycles on the structure and hardness of the metal in the HAZ overheating area in welded joints of medium-carbon alloy steels of high hardness. *The Paton Welding J.*, 6, 46–50. DOI: <https://doi.org/10.37434/tpwj2025.06.07>

JOURNAL HOME PAGE

<https://patonpublishinghouse.com/eng/journals/tpwj>

Received: 05.05.2025

Received in revised form: 05.06.2025

Accepted: 27.06.2025

The Paton Welding Journal



SUBSCRIBE TODAY

Available in print (348 Euro) and digital (288 Euro) formats
patonpublishinghouse@gmail.com; journal@paton.kiev.ua
<https://patonpublishinghouse.com>